

(12) LEVEL III

AD-E300 800

DNA 4216T-3

ADA 085760

DICE THROW UHF/SHF TRANSMISSION EXPERIMENT

Volume III — Final Data Reduction and Interpretation

Alan A. Burns

Patricia L. Crawley

SRI International

333 Ravenswood Avenue

Menlo Park, California 94025

1 August 1979

Topical Report for Period 16 November 1976—19 March 1979

CONTRACT No. DNA 001-75-C-0206

APPROVED FOR PUBLIC RELEASE;
DISTRIBUTION UNLIMITED.

THIS WORK SPONSORED BY THE DEFENSE NUCLEAR AGENCY
UNDER RDT&E RMSS CODES B322075462 L25AAXHX63310,
B322075462 K43AAXHX68501 AND B322076462 L35AAXHX68501
H2590D.

Prepared for

Director

DEFENSE NUCLEAR AGENCY

Washington, D. C. 20305

DTIC
ELECTE
JUN 23 1980
S D
B

80 5 19 214

Destroy this report when it is no longer needed. Do not return to sender.

PLEASE NOTIFY THE DEFENSE NUCLEAR AGENCY,
ATTN: STTI, WASHINGTON, D.C. 20305, IF
YOUR ADDRESS IS INCORRECT, IF YOU WISH TO
BE DELETED FROM THE DISTRIBUTION LIST, OR
IF THE ADDRESSEE IS NO LONGER EMPLOYED BY
YOUR ORGANIZATION.



UNCLASSIFIED

SECURITY CLASSIFICATION OF THIS PAGE (When Data Entered)

REPORT DOCUMENTATION PAGE		READ INSTRUCTIONS BEFORE COMPLETING FORM
1. REPORT NUMBER DNA 4216T-3	2. GOVT ACCESSION NO. AD-A085760	3. RECIPIENT'S CATALOG NUMBER 760
4. TITLE (and Subtitle) DICE THROW UHF/SHF TRANSMISSION EXPERIMENT Volume III—Final Data Reduction and Interpretation C013969		5. TYPE OF REPORT & PERIOD COVERED Topical Report for Period 16 Nov 76—19 Mar 79
7. AUTHOR(s) Alan A. Burns Patricia L. Crawley		6. PERFORMING ORG. REPORT NUMBER SRI Project 3972
9. PERFORMING ORGANIZATION NAME AND ADDRESS SRI International 333 Ravenswood Avenue Menlo Park, California 94025		8. CONTRACT OR GRANT NUMBER(s) DNA 001-75-C-0206 ✓
11. CONTROLLING OFFICE NAME AND ADDRESS Director Defense Nuclear Agency Washington, D.C. 20305		10. PROGRAM ELEMENT, PROJECT, TASK AREA & WORK UNIT NUMBERS Subtasks L25AAXHX633-10, K43AAXHX685-01, and L35AAXHX685-01
14. MONITORING AGENCY NAME & ADDRESS (if different from Controlling Office)		12. REPORT DATE 1 August 1979
		13. NUMBER OF PAGES 142
		15. SECURITY CLASS (of this report) UNCLASSIFIED
		15a. DECLASSIFICATION/DOWNGRADING SCHEDULE
16. DISTRIBUTION STATEMENT (of this Report) Approved for public release; distribution unlimited.		
17. DISTRIBUTION STATEMENT (of the abstract entered in Block 20, if different from Report)		
18. SUPPLEMENTARY NOTES This work sponsored by the Defense Nuclear Agency under RDT&E RMSS Codes B322075462 L25AAXHX63310, B322075462 K43AAXHX68501 and B322076462 L35AAXHX68501 H2590D.		
19. KEY WORDS (Continue on reverse side if necessary and identify by block number) DICE THROW Dust Clouds RF Effects UHF/SHF Propagation High-Explosives Tests Dust and Debris Nuclear Weapons Effects		
20. ABSTRACT (Continue on reverse side if necessary and identify by block number) This report presents the final results from an rf propagation experiment fielded during the DICE THROW HE test held at the White Sands Missile Range on 6 October 1976. That experiment was designed to measure the effects of high-density, explosively produced dust clouds on a series of coherent signals ranging in frequency from 400 MHz to 10 GHz. Both amplitude and phase data were obtained. This report contains: (1) A description of the experiment.		

DD FORM 1 JAN 73 1473

EDITION OF 1 NOV 65 IS OBSOLETE

UNCLASSIFIED

SECURITY CLASSIFICATION OF THIS PAGE (When Data Entered)

UNCLASSIFIED

SECURITY CLASSIFICATION OF THIS PAGE(When Data Entered)

20. ABSTRACT (Continued)

- (2) The reduced rf data.
- (3) An interpretation of the results.
- (4) A discussion of theoretical effects of dust and crater debris on rf signal propagation.
- (5) Results from photographic coverage of the event, including comparisons with hydrodynamic-code flow-field predictions and with nuclear and other non-nuclear tests.

The observed rf results were found to be consistent with the behavior expected from theoretical considerations and dust densities obtained from a simple model based on material missing from the water and measured cloud volume. Because of the relatively small volume of space affected, rf effects were generally mild, unless a threshold combination of the dust density and the particle size distribution parameter were exceeded. Once the threshold was crossed, extinction coefficients rose to as much as several tens of decibels per kilometer. This was accompanied by the complete loss of a coherent signal component, strong fading, and the apparent onset of multiple scattering.

UNCLASSIFIED

SECURITY CLASSIFICATION OF THIS PAGE(When Data Entered)

CONTENTS

LIST OF ILLUSTRATIONS	2
LIST OF TABLES	6
I INTRODUCTION	7
II EXPERIMENTAL LAYOUT AND EQUIPMENT	11
III MEASURED RF EFFECTS	20
A. General	20
B. Time Histories of RF Effects	27
C. Spectral Analyses	42
IV INTERPRETATION	50
V CONCLUSION	56
APPENDICES	
A EFFECTS OF DUST CLOUDS ON ELECTROMAGNETIC PROPAGATION	59
B DICE THROW CLOUD DEVELOPMENT	79
REFERENCES	132

ACCESSION for		
NTIS	White Section	<input checked="" type="checkbox"/>
DDC	Buff Section	<input type="checkbox"/>
UNANNOUNCED		<input type="checkbox"/>
JUSTIFICATION _____		
BY _____		
DISTRIBUTION/AVAILABILITY CODES		
Dist.	AVAIL. and/or	SPECIAL
A		

ILLUSTRATIONS

1	DICE THROW Site Location	8
2	Experimental Layout of DICE THROW Transmission Experiment	12
3	DICE THROW Site Layout with Microwave Transmission Experiment Site Locations	14
4	Line-of-Sight Penetration Points in Vertical Plane Through Ground Zero and Perpendicular to Paths 1 and 4 . . .	15
5	Evolutional Growth of DICE THROW Cloud from R-1 Site at T + 0.1, 4, 10, and 20 s with Propagation Path Inter- section Points	21
6	Evolutional Growth of DICE THROW Cloud from R-1 Site at T + 20, 30, 60, and 90 s with Propagation Path Inter- section Points	22
7	Evolutional Growth of DICE THROW Cloud from PR Site at T + 0.2, 4, 10, and 20 s with Propagation Pathways	23
8	Evolutional Growth of DICE THROW Cloud from PR Site at T + 20, 30, and 60 s with Propagation Pathways	24
9	Evolutional Growth of DICE THROW Cloud from NOP Site at T + 0.4, 10, 20, and 30 s with Propagation Path Inter- section Points	25
10	Evolutional Growth of DICE THROW Cloud from NOP Site at T + 30, 60, and 90 s and at T + 2 and 3 min with Propagation Path Intersection Points	26
11	Path 1 UHF Signal Fluctuations	28
12	UHF Signal Fluctuations for Paths 1, 2, and 3	29
13	Polar Plots of Path 1 and Path 3 413-MHz Quadrature Signal Components from T_0 to T + 5 s (these data have been decimated)	32
14	L-, S-, and X-Band Amplitudes and Phases from T - 1 s to T + 14 s	34
15	Polar Plots of Path 1 S- and X-Band Quadrature Signal Components from T_0 to T + 5 s (these data have been decimated)	36
16	Path 2 and 3 X-Band Signal Fluctuations	38
17	Path 1 S-Band Amplitude and Phase from T + 3 s to T + 30 s	40

18	Path 4 X-Band Signal Fluctuations	41
19	Path 4 UHF Signal Fluctuations	43
20	UHF Signal Fluctuations for Paths 4, 5, and 6	44
21	Power Spectrum of the UHF Path 1 Complex Signal Fluctuations	46
22	Power Spectrum of the Path 1 X-Band Complex Signal Fluctuations	47
23	Power Spectrum of the Path 3 X-Band Complex Signal Fluctuations	48
24	Power Spectrum of the Path 4 X-Band Complex Signal Fluctuations	49
25	Comparisons Between Computed Absorption and Phase Shift and Measured Amplitude and Phase Changes	51
26	Average Dust Density in DICE THROW Cloud Inferred from Volume Measurements	52
27	Calculated Absorption Compared to Measured Amplitude Fluctuations at L-, S-, and X-Bands	53
A-1	RF Propagation and Dust Clouds	59
A-2	Attenuation per Radian (α/ϕ) Excess Phase Shift vs Frequency	65
A-3	Excess Phase Retardation and Absorption per Kilometer	67
A-4	Intersections of Optical and Rayleigh Absorption and Scattering Asymptotes	69
A-5	Critical Radii vs Frequency	72
A-6	Attenuation Due to Extinction Caused by Large Scatterers	74
A-7	Ratio of Scattering Losses vs Frequency	76
A-8	Volume Scattering Coefficient vs Radar Frequency for Various Dust Particle Size Distributions--Incoherent and Semicoherent Scattering	77
A-9	Ratio of Coherent to Incoherent Scattering vs Radar Frequency for Various Models of Dust Particle Size Distribution	78
B-1	DICE THROW Capped Cylinder Charge of ANFO--Pre-Zero View from Phase Repeater Site	82
B-2	DICE THROW Early Times $T + 0.1$ s to $T + 0.5$ s, from Four Camera Sites	83
B-3	DICE THROW Wilson Cloud at $T + 1$ s, Viewed From Phase Repeater	84
B-4	DICE THROW at 2 s	85

B-5	DICE THROW at 4 s	86
B-6	DICE THROW at 6 s	87
B-7	Early-Time Photos from Two Other ANFO Events	89
B-8	Overhead View of DICE THROW Cloud at T + 0.8 s	90
B-9	120-T ANFO, Pre-DICE THROW II-2	91
B-10	DICE THROW Cloud Compared to Hull Velocity Field Calculation at 5 s	93
B-11	Cumulative Crater Volume vs Distance Away From Crater Center	94
B-12	DICE THROW at 8 s	95
B-13	DICE THROW at 10 s	96
B-14	Overhead Views of DICE THROW Cloud	97
B-15	DICE THROW Cloud Compared to HULL Velocity Field Calculation at 10 s	98
B-16	DICE THROW at 15 s	99
B-17	Nuclear Detonations at T + 20 s	101
B-18	100-T TNT, Pre-DICE THROW II-1	102
B-19	500-T TNT (Tangent Sphere), Mixed Company III	103
B-20	DICE THROW Cloud Compared to HULL Velocity Field Calcu- lations at 20 s	104
B-21	DICE THROW at 20 s	105
B-22	DICE THROW at 30 s	106
B-23	DICE THROW at 45 s	107
B-24	DICE THROW Cloud Compared to HULL Velocity Field Calculations.	108
B-25	120-T ANFO, Pre-DICE THROW II-2	109
B-26	1.2-kt Nuclear at -17 ft, Buster Jangle: Uncle 1951, T + 20 s	110
B-27	DICE THROW at T + 1 min	112
B-28	DICE THROW Cloud Compared to HULL Velocity Field Calcu- lation at T + 1 min	113
B-29	DICE THROW at T + 2 min	114
B-30	DICE THROW at T + 4 min	115
B-31	Measured Cloud Height, Width, and Stem Width vs Time from Receiver 1 Camera Site	117
B-32	Measured Cloud Height, Width, and Stem Width vs Time from Phase-Repeater Camera Site	118

B-33	Measured Cloud Height, Width, and Stem Width vs Time from North Oscuro Peak Camera Site	119
B-34	DICE THROW Cloud Height and Width Averaged from R-1, PR, and NOP Camera Sites	121
B-35	Measured PDT II-2 Cloud Height and Width vs Time	122
B-36	DICE THROW Cloud Edge Displacement from GZ (R-1 Site)	123
B-37	Measured DICE THROW Cloud Volume vs Time	124
B-38	Average Dust Density in the DICE THROW Cloud Inferred from Volume Measurements	125
B-39	Mass of Dust Aloft vs Time for DICE THROW and Hard Rock Particle Size Distributions	126
B-40	ANFO Dust Cloud Case by Particle Size Distribution Power (γ) vs Time for DICE THROW and Hard Rock Particle Size Distributions	127
B-41	Yield-Scaled Photographs of PDT II-2 Showing Anticipated Intersection of Propagation Paths with DICE THROW Phenomena. Dimensions and time scaled as $\sqrt[3]{5}$. (Photos courtesy of A. D. Thornbrough, Sandia Labs).	128
B-42	Photographs of DICE THROW Showing Actual Intersection of Propagation Paths	129

TABLES

1	Measurement Frequencies	13
2	WSMR Coordinates of DICE THROW Microwave Transmission Experiment Site Locations	16
3	Antenna Parameters	17
4	Shock-Wave Arrival Times at Various Locations Based on Measured Free-Field Blast Data	30
5	Path 1 Quadrature Signal Component Statistics in Units of Digitizer Output Counts	37
6	Ratios of Signal Power Variance (σ_p) Mean Signal Power (\bar{P}) in the T_0 -to-2.7-s Time Interval	37
A-1	Summary of Dielectric Property Measurements	63
A-2	Inferred Average Dielectric Constant, Molecular Loss Tangent, and Conductivity for Solid Particles	63
A-3	Excess Phase Retardation and Absorption versus Frequency at 10^{-3} g/cm ³ Dust Cloud Density	66
B-1	Automax 35-mm Framing Camera Parameters	80

I INTRODUCTION

Under the sponsorship of the Defense Nuclear Agency (Contract DNA001-75-C-0206, SRI International successfully fielded a UHF/SHF coherent transmission experiment. This experiment was designed to measure the effects of dust and debris on signals passing through the cloud lofted by the DICE THROW high-explosive test. The test, which was a 628-ton ANFO (ammonium nitrate plus fuel oil) detonation, took place at 0800 MDT on 6 October 1976 at the Giant Patriot site in the northern part of the White Sands Missile Range (WSMR) (Figure 1). Because the explosion lofted between 4 and 10 kt of (desert) soil, it simulated in at least one way a much larger nuclear detonation than its 500-ton TNT equivalent. A rather complete description of that test and the various experimental programs (including this one) associated with it appears in the Proceedings of the DICE THROW Symposium.^{1*}

The UHF/SHF transmission experiment consisted basically of making measurements of amplitude and phase fluctuations on 12 different CW signals between 379 MHz and 10.2 GHz. Those signals were transmitted along six paths penetrating the space above and in the vicinity of ground zero where the dust cloud was expected. Preliminary results of the experiment and a report on investigations of soil properties appear in topical reports 1 and 2 under this contract.^{2,3} An earlier report⁴ covered the experimental design phase.

The primary reason for fielding this experiment and making these measurements was simply that until then, no one had made any rf transmission measurements through high-density dust and debris clouds lofted by large explosions. There is legitimate concern that various kinds of communication and sensor systems might be affected adversely by large-scale dust clouds produced by surface, or near-surface nuclear detonations.

*References are listed at the end of the report.

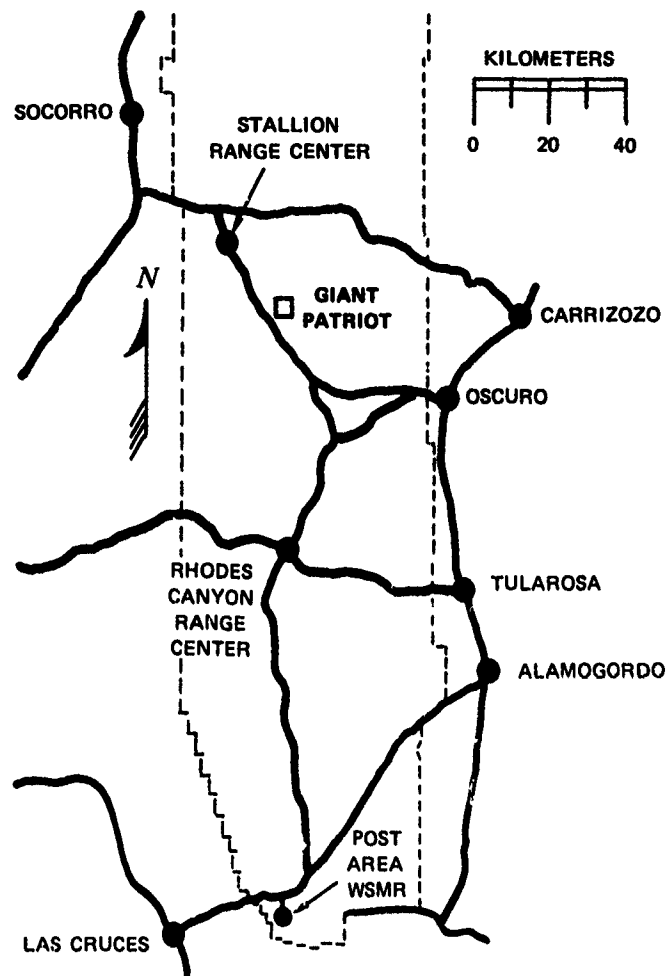


FIGURE 1 DICE THROW SITE LOCATION

Our goal was to make accurate measurements of both amplitude and phase perturbations over a range of wavelengths that are commonly used by communications and sensing systems. Although many of the frequencies used were in or near bands used by military systems, there was no attempt to simulate in any way the operation of any actual system. These measurements were strictly of basic rf effects on simple, CW, signals. Nuclear dust cloud rf effects can in principle be estimated, using these basic measurements.

Of course, the magnitudes, durations, and extents of the rf effects measured during DICE THROW were much smaller than are likely to be encountered in a nuclear environment. Although the DICE THROW main event

was much more effective at raising dust than the "megaton of dust per megaton of yield" rule would predict, it is still quite small, and the flow-field velocities for the DICE THROW charge configuration and composition are very small as well. According to calculations, the capped cylinder ANFO configuration produces flow fields having significantly lower velocities than even those occurring after tangent-sphere TNT detonations. In addition, the areal extent of the dust cloud was only on the order of a few hundred meters during the early phases. After a nuclear detonation, a much larger area and volume are affected, and the larger velocities during the rising fireball phase would tend to support more and larger particles for much greater lengths of time. Extrapolation to the nuclear environment, while not part of the work reported here, is an important and in many ways a difficult, uncertain step that needs to be taken. These data provide one of the bases for such extrapolation.

The first subject in this report is a description of the experiment and its layout. The next two sections are devoted respectively to presenting and to interpreting the measured effects, which can be divided into two categories. The first category, which lasted for several seconds following the detonation, was characterized by intense fading, including the complete loss of a coherent signal on many of the frequencies. Scattering from large particles seems to have been very important then. The second category was characterized by gentle effects, because of fallout of the larger particles. The duration of effects was limited by the rapid drift of the dust cloud away from the signal paths due to higher-than-expected winds at test time.

There are two appendices. The first (Appendix A) is a brief review of the theoretical effects of dust clouds on electromagnetic propagation in the UHF/SHF range. Results of laboratory measurements of the dielectric properties of soil samples gathered from the DICE THROW crater are summarized there as well. Our conclusion is that phase shifts and attenuation caused by absorption are probably the dominant effects except at early times before sufficient numbers of large particles have fallen out.

Scattering losses can become very large when very many large particles are in the dust cloud. These results are used in the interpretation of the experimental results.

Development of the dust cloud is considered in Appendix B. Photographic records, some of which were obtained from our own boresight cameras, are compared with other events and with Air Force Weapons Laboratory (AFWL) hydrodynamic (HULL) code calculations. Comparisons are also made with some previous HE test results, and with the appearance of several nuclear events. These comparisons illustrate the substantial dissimilarities between the clouds produced by different types of detonations.

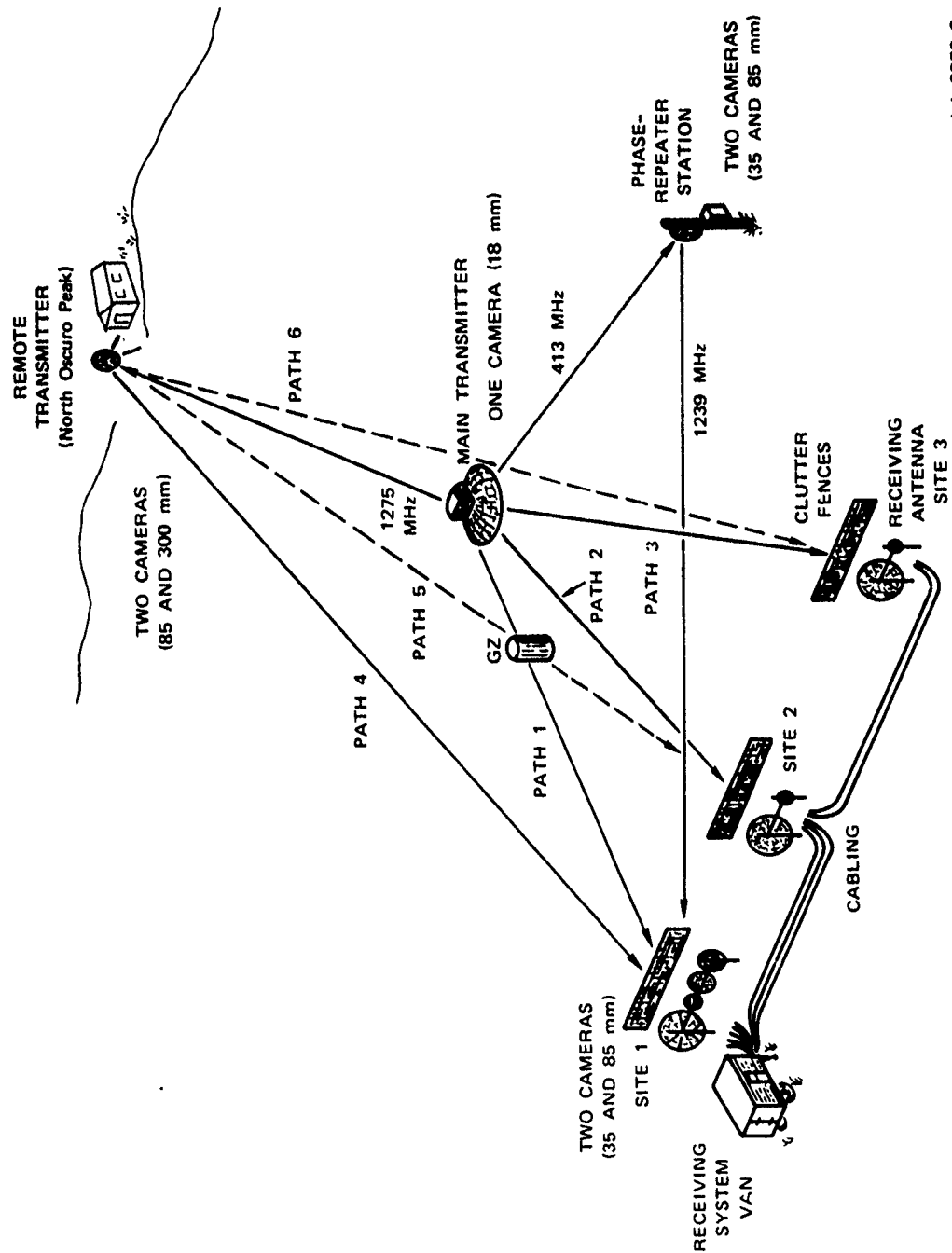
The measured DICE THROW crater volume was used to bound the uncertainty in the amount of lofted dust and debris. A simple model for the average dust density that is based on the measured dust cloud volume and on estimates of the mass of lofted soil is developed from the photographs. These photographic records are very important to the interpretation of the results of the experiment.

II EXPERIMENTAL LAYOUT AND EQUIPMENT

Figure 2 is a schematic of the experimental layout. Signals were transmitted from two locations and were received at three sites, providing six measurement paths (labeled Paths 1 through 6). In addition, the 413-MHz signal from the main transmitter was received at the "phase-repeater station," multiplied to 1239 MHz, then retransmitted to the receiving system. This arrangement served to transfer a phase reference signal from the main transmitter to the receiving system along a path unaffected--or only briefly affected--by the explosion. Finally, a 1274-MHz signal from the main transmitter was received at North Oscuro Peak to phase-lock the remote transmitter. The transmitter power levels ranged between 10 and 100 mW.

Table 1 lists the exact frequencies of the signals transmitted along the six measurement paths. Initially, no measurements were planned for Paths 5 and 6. It was possible, however, to receive the 424-MHz signal from the remote transmitter at any of the receiving antenna sites. Therefore, because it appeared that a net gain of data could easily be obtained, we decided to make a simple modification to switch sequentially, or commutate, the 424-MHz receiver channel between the three antenna sites. A 2-s period was chosen, with the 424-MHz UHF signal of Path 4 received for 1 s and the 424-MHz UHF signals of Paths 5 and 6 received for 0.5 s each. Although Path 6 passed quite far from ground zero, it was believed that there was a reasonable chance that the cloud might drift into that path later.

Two major considerations primarily dictated the physical locations of the various components of the experiment. First, based on the expected size of the dust cloud, a 20-m Fresnel zone radius at 413 MHz was desirable. Second, Path 4 was required to pass about 200 m directly over ground zero. Secondary considerations included: (1) access and practicality, (2) keeping the signals clear of obstacles and equipment, and



LA-3972-3

FIGURE 2 EXPERIMENTAL LAYOUT OF DICE THROW TRANSMISSION EXPERIMENT

Table 1

MEASUREMENT FREQUENCIES

Path	Frequency (MHz)
1	378.608, 413.028, 447.447 1273.503 2891.196 10188.024
2	413.028 10188.024
3	413.028 10188.024
4	424.501 8914.521
5	424.501
6	424.501

(3) separating Paths 2 and 3, respectively, by one (40 m) and three (120 m) UHF Fresnel zone diameters from ground zero (GZ) in order to probe the dust cloud laterally along independent lines of sight at UHF. Figures 3 and 4, respectively, present the plan and elevation (in the plane of ground zero) views of the resulting layout. The WSMR coordinates of the various sites are listed in Table 2. (So that it would be more accessible, the phase repeater station was not located at the surveyed point, and because its new position was not resurveyed, only its approximate location in WSMR coordinates is listed.) For reference, the WSMR coordinates of ground zero, in meters, were E135,027, N198,205, and H1442 (see Figure 3).

The beamwidths of the antennas were chosen so that the entire expected extent of the early dust cloud would fall well within the beams.

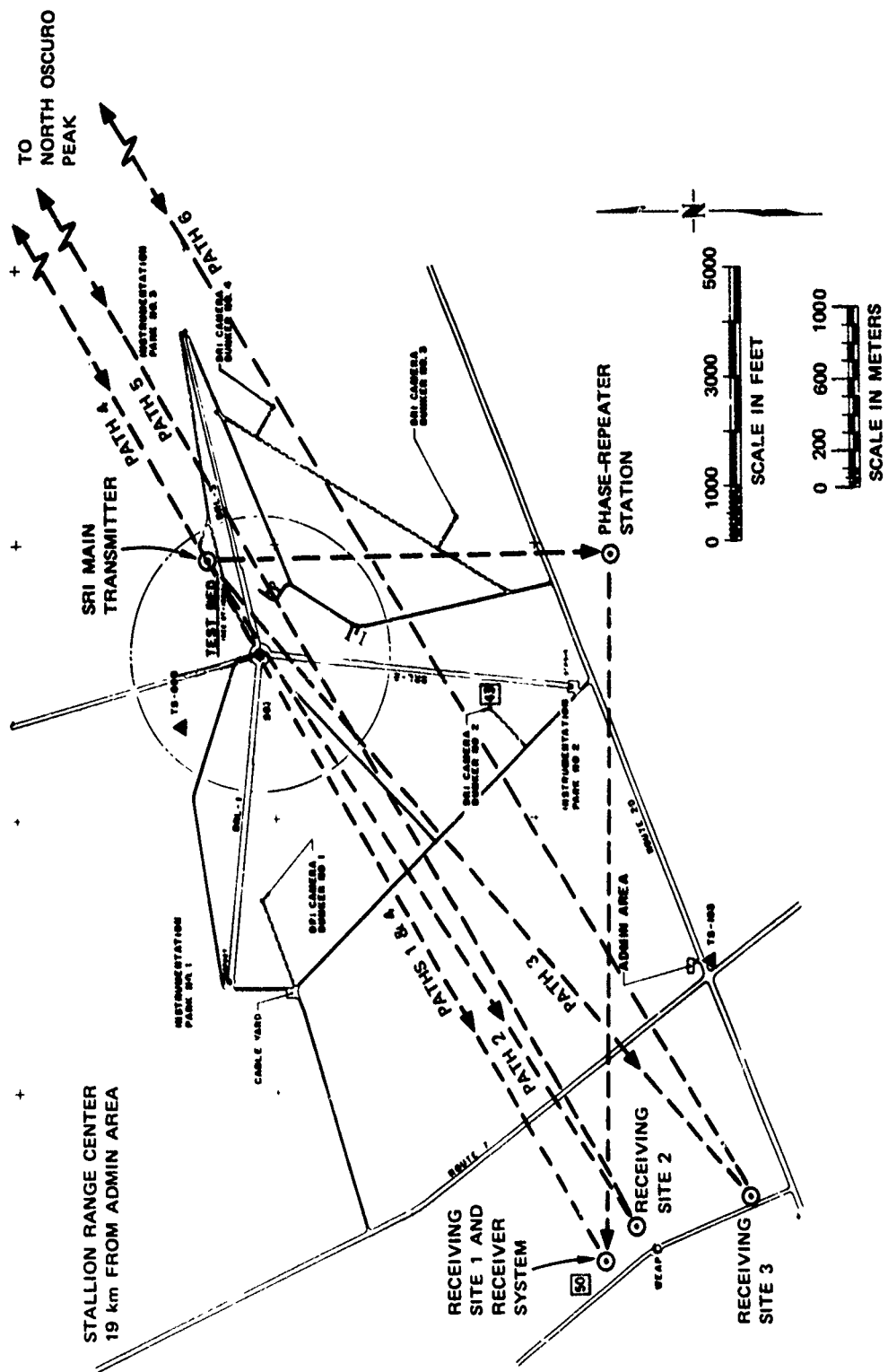
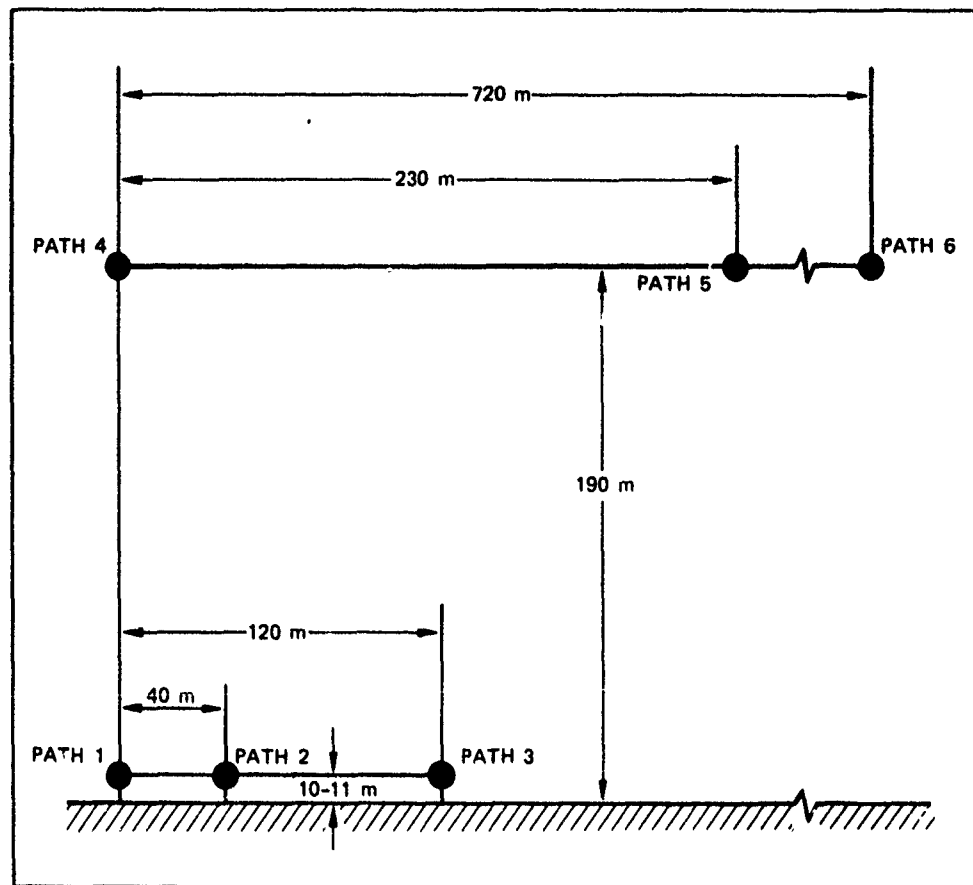


FIGURE 3 DICE THROW SITE LAYOUT WITH MICROWAVE TRANSMISSION EXPERIMENT SITE LOCATIONS



LA-3972-6

FIGURE 4 LINE-OF-SIGHT PENETRATION POINTS IN VERTICAL PLANE THROUGH GROUND ZERO AND PERPENDICULAR TO PATHS 1 AND 4

This choice tended to eliminate any antenna beam-limiting effects on the measurements. However, the antenna beams had to be as narrow as practical in order to reduce the possibility of troublesome reflections from nearby objects. Except for UHF, where impractically large antennas would have had to be used, the antenna parameters as listed in Table 3 fulfilled these experimental requirements. An extensive program of antenna measurements was undertaken before the experiment was fielded.

Because the main, multifrequency transmitter had to be placed quite close (630 m) to ground zero in order to reduce the UHF Fresnel zone, it was necessary to harden the antennas and to protect the electronics from

Table 2

WSMR COORDINATES OF DICE THROW MICROWAVE
TRANSMISSION EXPERIMENT SITE LOCATIONS

Site	WSMR Coordinates (m)		
	E	N	H
Main Transmitter	135,569	198,525	1450
Remote Transmitter (North Oscuro Peak)	148,810	206,340	2440
Phase Repeater	135,600	196,200	1440
Receiving Site 1 (Main)	131,614	196,191	1429
Receiving Site 2 (Outrigger 1)	131,843	195,995	1429
Receiving Site 3 (Outrigger 2)	131,972	195,319	1428

the shock wave. (The measured overpressure at 630 m was about 19 kPa.) Protection and immobilization of the antennas was accomplished by casting them into a concrete block and filling their apertures with foam. The UHF antenna, which had a wider beamwidth than the others, was skewed to the left in order to increase the signal strength at the phase repeater station (the others were aimed in azimuth at ground zero). An electronics shelter was partly buried in the rear of a 20-ft earthen mound constructed to support and elevate the antennas. No damage was sustained by either the antennas or the electronics during the event. The phase repeater station consisted of antennas, electronics, and cameras mounted on a 20-ft tower.

Several actions were taken to reduce the possibility, and the effects, of any multipath signals due to reflections from the ground surface or from equipment or structures. Circular polarization was used on all of the measurement paths because specular or quasi-specular reflection

Table 3

ANTENNA PARAMETERS

	Transmit or Receive	Band	Frequency (MHz)	Type *	Size (ft)	Polarization †	Nominal Gain (dB)	Beamwidth (deg)
Main Transmitter	T	UHF	379 to 447	XDC	--	RC	10	50
	T	L [‡]	1274	CH	--	RC	15	25
	T	L	1274	RH	--	VL	15	25
	T	S	2891	CH	--	RC	15	25
	T	X	10188	CH	--	RC	15	25
Receiver Site 1	R	UHF	379 to 447	PD	10	RC	20	15 to 18
	R	L [§]	1239	PD	6	VL	25	9
	R	L	1274	PD	6	RC	75	9
	R	S	2891	PD	3.4	RC	28**	7**
	R	X	8915/10188	PD	1	RC	26	8
Receiver Sites 2 and 3	R	UHF	413/424	PD	10	RC	19	16
	R	X	10188	PD	1	RC	26	8
Remote Transmitter (North Oscuro Peak)	T	UHF	424	PD	10	RC	20	16
	R	L	1274	PD	6	VL	25	9
	T	X	8915	PD	4	RC	38	2
Phase Repeater	R	UHF	413	QHA	--	RC	>10	50
	T	L	1239	PD	6	VL	25	9

Notes:

*XDC = crossed dipoles in cavity; CH = conical horn; RH = rectangular horn; PD = parabolic dish;
QHA = quad helix array.

†RC = right circular; VL = vertical linear.

‡The linearly polarized rectangular horn antenna was pointed at North Oscuro Peak.

§Receiving antenna for phase repeater transmissions.

**At 10,188 MHz.

from conductive surfaces reverses the sense of circular polarization. (Because the requirements were much less severe on the phase-reference paths, vertical linear polarization was used on them.) Both the transmitting and receiving antennas were tilted upward by one-half of their beamwidths to discriminate against ground-reflected signals. Clutter fences were placed in front of the receiving antennas to reduce ground reflections. These fences were 30 m wide and were placed at the geometrical points of reflection (50 m in front of the receiving antennas) for surface-reflected signals from the North Oscuro transmitter. Although such fences are quite effective against surface-reflected signals from high-elevation sources, they are not very effective in suppressing those associated with very-low-elevation-angle paths like Paths 1 to 3 because the diffraction angles are very small. The best one could do would be to place the top of the fence so that both the direct and surface-reflected signals would be in the shadow zone; such an arrangement attenuates any reflected signals more than it does the direct one. For DICE THROW the edges of the geometric shadows of the tops of the 2.3-m-high (7.5 ft) fences illuminated by the main transmitter passed through the centers of all of the receiving antennas behind the fences. All of the receiving antennas were aimed at the appropriate transmitters. The direct signals from the upper paths (4 through 6) were virtually unaffected by the clutter fences.

The receiver was designed to be linear over at least a 60-dB dynamic range, and the signal levels were adjusted to be about 10 dB below saturation to account for any enhancements due to diffraction or focusing. Rather than detecting amplitude and phase, the quadrature signal components (which can be interpreted as the real and imaginary parts of the complex representation of the received signal or as a pair of zero-carrier-frequency IF signals) were developed at the receiver outputs. The amplitude and phase of each signal can be easily computed from each pair of quadrature components. In a sense, the nonlinear "detection" process occurs in the mathematical computation. Greater processing flexibility justifies the quadrature-component approach. The overall bandwidths of all the receiver channels were limited at each quadrature

component output by a four-pole, low-pass Butterworth filter with 150-Hz, 3-dB cutoff frequency. Each of the 13 receiver channels used provided a pair of quadrature component outputs. One of the 13 channels was used for the 1239-MHz phase-reference signal. One of the twelve recording channels used for measurement paths was commutated between the 424-MHz signals from Paths 4, 5, and 6 as described above. Quadrature component pairs were simultaneously digitized by a pair of 12-bit (± 2048 -point) analog-to-digital converters (one for each of the quadrature components). Thus, 26 channels of data were digitized. The digitization rate was 500 samples per second, and the commutation interval was 80 μ s. Then, under the control of an HP-2100 minicomputer, the data were written on magnetic tape. Two independent digital tape recorders were used. A backup analog recording system was also operated. That system multiplexed a 50-kHz IF signal from each of the 13 receiver channels with a 100-kHz pilot tone serving as a phase reference, and recorded each resulting composite signal on a single tape recorder track. Time signals were also recorded by both the primary and the backup recording systems.

III MEASURED RF EFFECTS

A. General

In this section we present the final results of the rf transmission experiment. The data, which were originally presented in Ref. 1, have been carefully calibrated and purged of all the artifacts that could be identified. A particularly great effort was expended toward the goal of obtaining continuous phase records--i.e., removing the discontinuities at $\pm 180^\circ$. While this was a simple process conceptually, in practice it was very difficult to devise an algorithm to make the decision of whether or not a phase transition across the $\pm 180^\circ$ boundary actually occurred when the signals were weak and fading.

The duration of rf effects was quite brief. On the lower paths (1, 2, and 3), there was a period of very strong effects lasting until about $T + 3$ to $T + 4$ s. By $T + 25$ s, all signal perturbations had ceased on those paths. Of the upper paths, only Path 4 passed through the dust cloud because of the adverse winds. (Although we did not expect an occultation on Path 6 due to its distance from GZ, we believed that there was a good chance of obtaining one on path 5.) Rf perturbations on Path 4 lasted until $T + 37$ s, when the dust cloud blew out of the line of sight.

For a quick comparative look at the evolutionary growth of the DICE THROW cloud as seen from the three major camera sites, R-1, PR, and NOP, Figures 5 through 10 have been prepared. Figure 5 displays the cloud outlines as recorded on film from the R-1 site at 0.1, 4, 10, and 20 s superimposed on a photograph taken at $T + 0.1$ s, which is lined up with its corresponding outline. In addition, the propagation path intersections are overlaid in their correct locations. Figure 6 similarly displays R-1 contours at 20, 30, 60, and 90 s over a photograph at 20 s.

Figures 7 and 8 show contours overlaid on the earliest photograph for each given time sequence as well as raypath configuration as seen

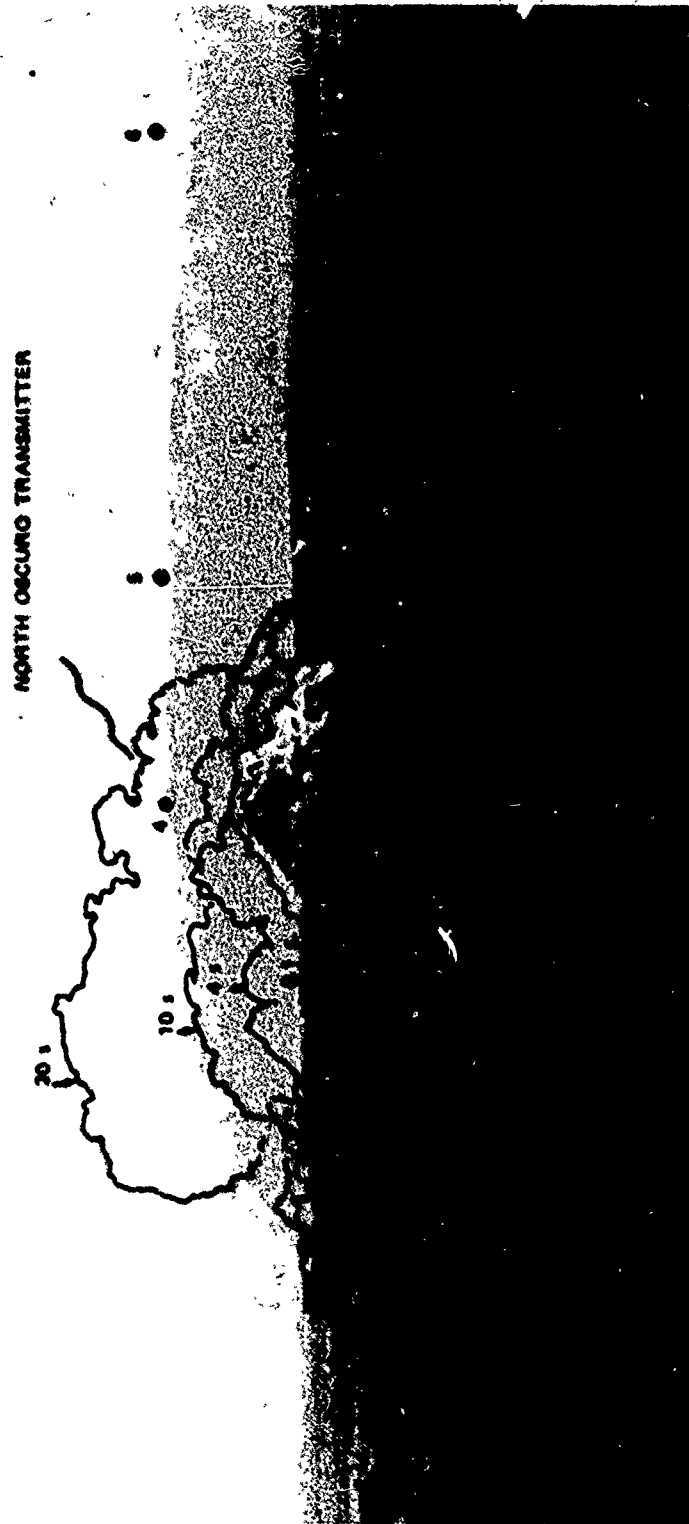


FIGURE 5 EVOLUTIONAL GROWTH OF DICE THROW CLOUD FROM R-1 SITE AT $T + 0.1, 4, 10,$ AND 20 s WITH PROPAGATION PATH INTERSECTION POINTS

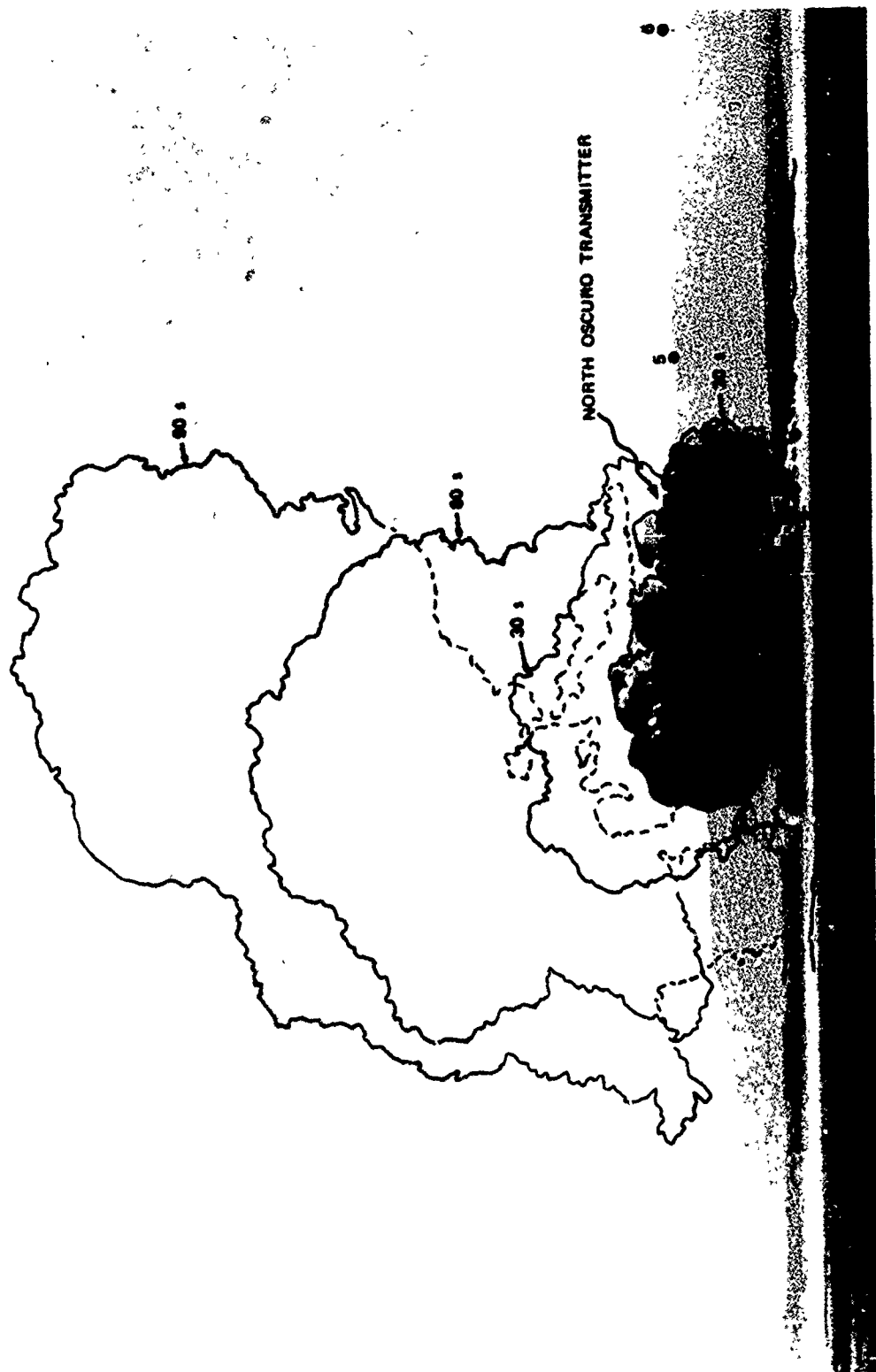


FIGURE 5 EVOLUTIONAL GROWTH OF DICE THROW CLOUD FROM R-1 SITE AT T + 20, 30, 60, AND 90 s WITH PROPAGATION PATH INTERSECTION POINTS



FIGURE 7 EVOLUTIONAL GROWTH OF DICE THROW CLOUD FROM PR SITE AT $T = 0.2, 4, 10,$ AND 20 s WITH PROPAGATION PATHWAYS

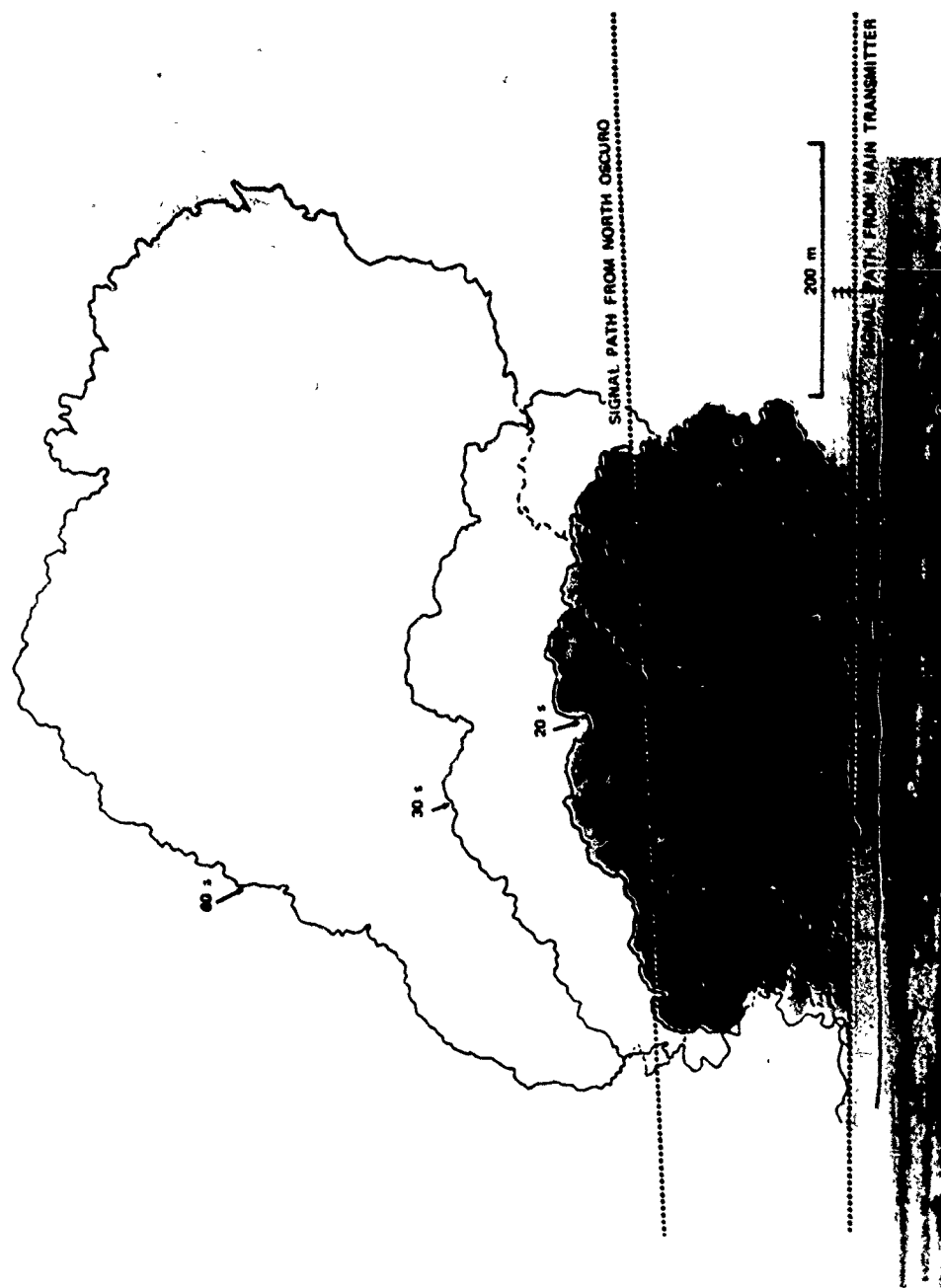


FIGURE 8 EVOLUTIONAL GROWTH OF DICE THROW CLOUD FROM PR SITE AT $T + 20$, 30, AND 60 s WITH PROPAGATION PATHWAYS



FIGURE 9 EVOLUTIONAL GROWTH OF DICE THROW CLOUD FROM NOP SITE AT $T + 0.4$, 10, 20, AND 30 s WITH PROPAGATION PATH INTERSECTION POINTS

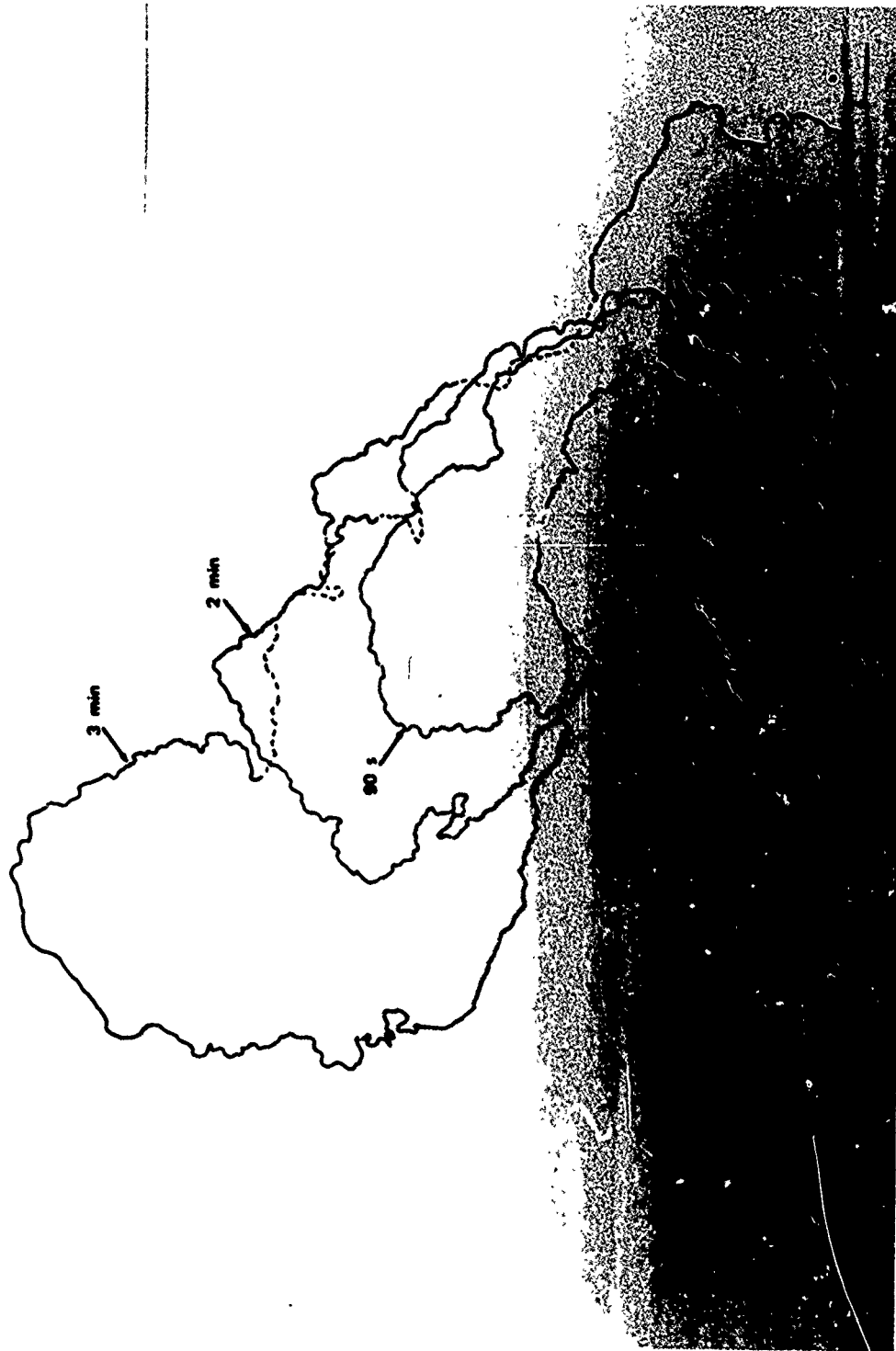


FIGURE 10 EVOLUTIONAL GROWTH OF DICE THROW CLOUD FROM NOP SITE AT $T + 30$, 60, AND 90 s AND AT $T + 2$ AND 3 min WITH PROPAGATION PATH INTERSECTION POINTS

from the PR site. Figures 9 and 10 present the view of the other side of the cloud seen from NOP. In the second figure for each site of the series, the early-time contour is the latest time contour outlined in the first figure.

B. Time Histories of RF Effects

Figures 11 and 12 show the amplitudes and phases for the lower path UHF signals from $T - 1$ to $T + 14$ s. The sign of the phase shift produced by the dust cloud for each of the signals depends on the manner in which the signal is translated in frequency by the receiver, and can be either positive or negative. For all of these UHF signals, the dust cloud would produce negative phase shifts. The Path 1 phase shifts of Figure 11 indicate that there was a relatively uniform fallout of most of the material in the cloud that ended at about $T + 5$ s. No particular change in the appearance of the cloud accompanied the end of the rapid fallout phase. It should be noted that a return to the baseline signal level could not be expected in general because of the blocking effect of the explosive stack.

It is possible that the passage of the shock wave at various places could perturb the signals in undesirable ways, such as introducing transient and permanent phase shifts with amplitude changes. Table 4 lists the shock-wave arrival times at several locations. These times were obtained from the average of the measured arrival times along the three instrumentation gauge lines laid out for the experiment.¹ The antenna oscillations at the main receiver site and the direct effects of the shock waves passing through the signal paths are the only ones that have been identified.

Because the rf effects of the dust cloud were very much the same on the Path-1 UHF signals, which were spaced 69 MHz apart (Figure 11), the coherent bandwidth at 400 MHz was substantially wider than 70 MHz. Since the coherent bandwidth is inversely related to the multipath time spread, this result is consistent with the small lateral extent of the dust cloud. Strong diffractive effects, however, were clearly present. Distortion of

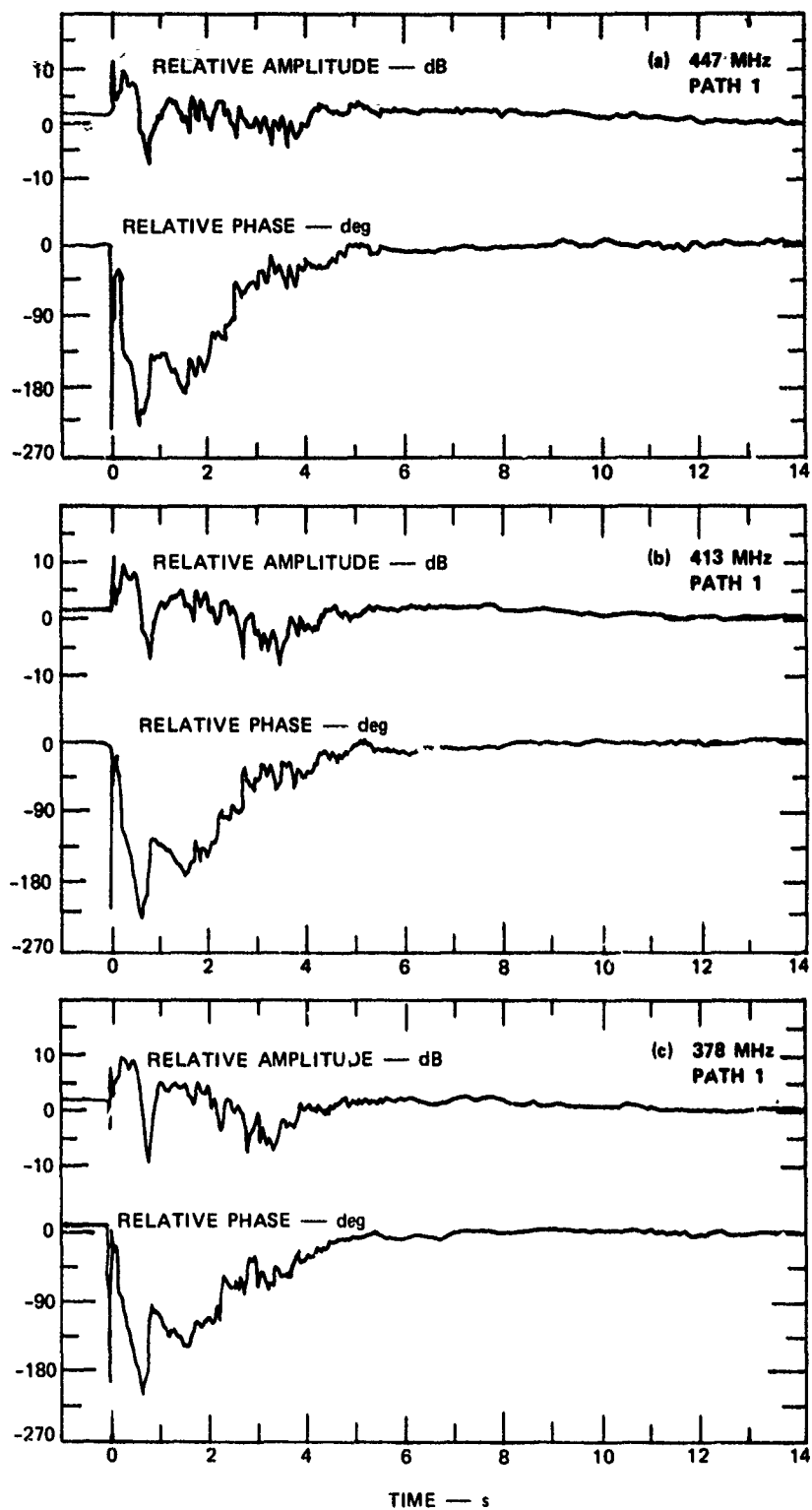


FIGURE 11 PATH 1 UHF SIGNAL FLUCTUATIONS

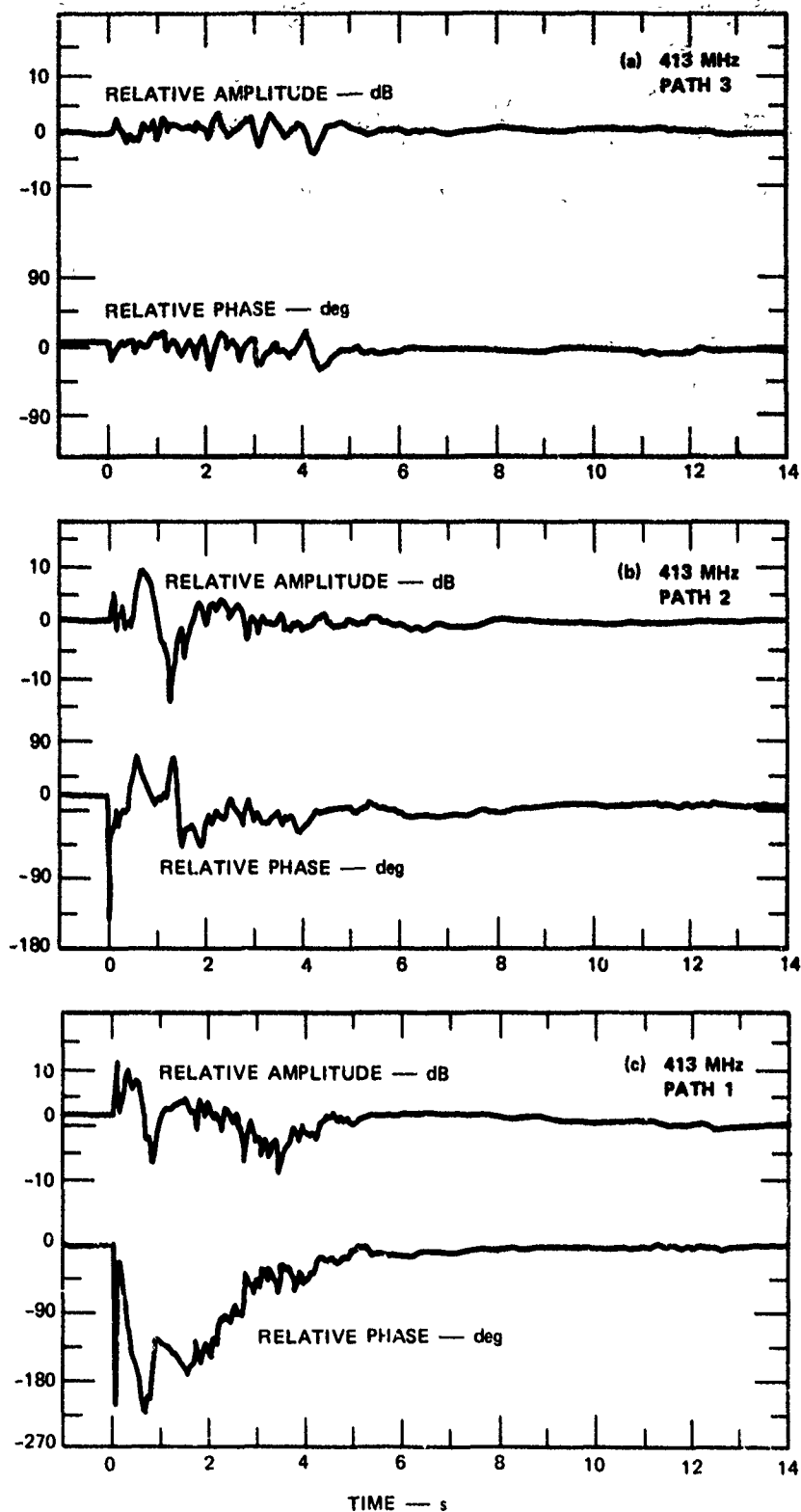


FIGURE 12 UHF SIGNAL FLUCTUATIONS FOR PATHS 1, 2, AND 3

Table 4

SHOCK-WAVE ARRIVAL TIMES AT VARIOUS LOCATIONS
BASED ON MEASURED FREE-FIELD BLAST DATA

Position	Range (m)	Arrival Time (s)
Main Transmitter (MT)	630	1.15
Phase Repeater (PR)	2400	5.8
Receiver (R-1)	3900	11.0*
Perpendicular to MT-PR path	535	0.9
Perpendicular to PR to R-1 path	2330	6.5

* Extrapolated.

the phase shifts due to diffraction was severe enough to preclude interpretation of phase shift in terms of integrated dust density until times later than $T + 1$ to $T + 1.5$ s.

This type of distortion is very evident in the results of Path 2 between T_0 and $T + 1.5$ s shown in the center panel of Figure 12. Part of the positive phase shift, which implies a loss of matter, in that time interval could have been caused by a decrease in atmospheric refractivity due to heating. As will be seen, this effect did occur along Path 4. If it were significant here, it would tend to reduce the effects of the dust. For instance, the HULL calculations predict temperatures above 600 K within a 150-m radius around ground zero near the surface during the first three seconds after detonation. Since the dominant term in the expression for atmospheric refractivity is inversely dependent on temperature, these temperatures would reduce the refractivity on the order of 100 N-units. At 400 MHz, the corresponding phase shift over a 300-m path is about 15° . Because this value is less than 10% of the measured phase shifts at early times on Path 1, temperature effects were probably not very important, although irregularities may have contributed to some of

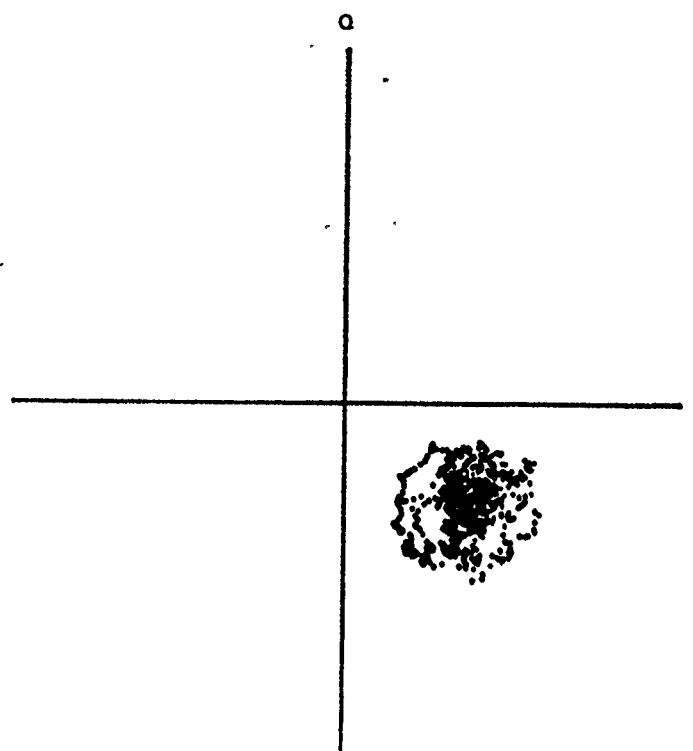
the fluctuations observed. The distortion due to the diffraction on Path 2 was so great that the net phase shifts were much larger in the positive direction than can be explained by heating.

The very strong similarities between the amplitude pattern for Path 2 from $T + 0.5$ s to $T + 1.5$ s and those for Path 1 from T_0 to $T + 1$ s lead to the conclusion that the Path 1 phase shifts were distorted in the same way as that for Path 2. This means that the undistorted Path 1 phase shifts were probably larger than those measured.

Another propagation effect is that a dust cloud tends to act as a converging lens. This is the reason for the early-time 10-dB signal enhancement on Paths 1 and 2. Note that, although the visible dust cloud practically instantaneously enveloped all of the lower paths, the focus for Path 2 was delayed about 0.5 s behind those for Path 1. Therefore the focus is apparently due to a dense bulk of crater ejecta within the visible cloud. Since the paths were spaced 40 m apart, the 0.5-s delay implies a horizontal velocity of about 80 m/s for the dense ejecta bulk. Although significant extinction would be expected from a very dense region, phase effects were dominant and the rf energy at 400 MHz was focused much more strongly than it was attenuated.

As would be expected, the onset of the strongest effects on Path 3 were delayed even more. The top panel of Figure 12 shows that the intensity of the fluctuations increased at $T + 2$ s and changed somewhat in character. However, for this path there was no general phase shift due to the integrated dust density. Rather, the signal appears to have exhibited Rician fading. Figure 13(a), which is a plot of the quadrature components of the 413-MHz Path-3 signal between T_0 and $T + 5$ s, supports this interpretation. The signal seems to be rather well characterized as being the sum of a steady, "coherent" component and a random, "scattered" component having no preferred phase; in contrast, the Path 1 signal, whose quadrature components from T_0 to $T + 5$ s are shown in Figure 13(b), had a coherent component that underwent a large phase change. This means that the part of the dust cloud penetrated by Path 3 was very inhomogeneous and did not have a very high average density. The 2-s delay and 120-m

(a) 413 MHz
PATH 3



(b) 413 MHz
PATH 1

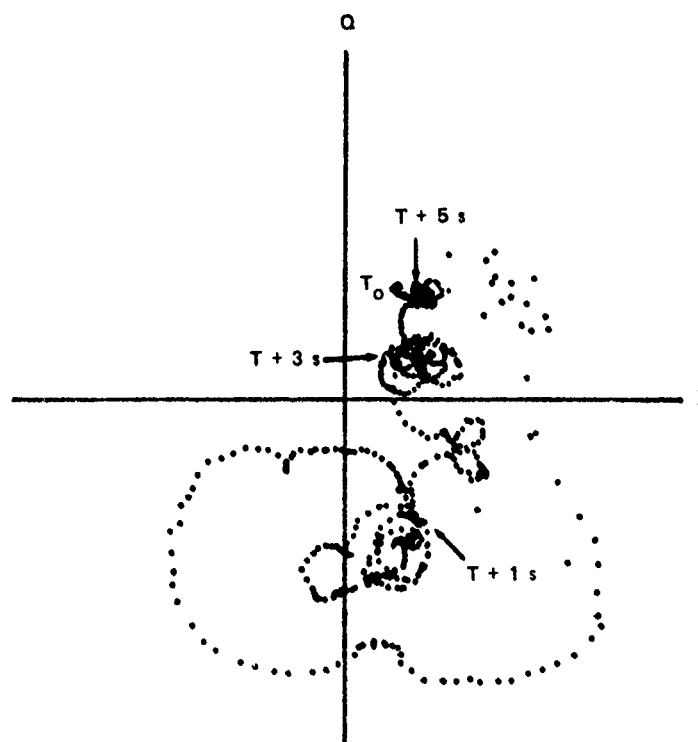


FIGURE 13 POLAR PLOTS OF PATH 1 AND PATH 3 413-MHz QUADRATURE SIGNAL COMPONENTS FROM T_0 TO $T + 5s$ (these data have been decimated)

offset of Path 3 from ground zero implies a 60-m/s ejecta velocity. This is slightly smaller than the 80-m/s horizontal velocity deduced from the Path 2 delay, but is consistent with a lower horizontal velocity for the higher-angle ejecta that would occult Path 3.

The higher-frequency (L-, S-, and X-band) Path 1 signals were different from the UHF signals during the early period in that all of them exhibited an effectively complete loss of a coherent signal component. Only a rapidly fading, scattered component of the transmitted signal was received for several seconds after detonation, during which time phase data were nearly meaningless. Figure 14 shows the L-, S-, and X-band amplitudes and phases from $T - 1$ to $T + 14$ s. Because these data have been smoothed using a 20-ms running average, the depth of the fades has been suppressed by about 3 to 5 dB--i.e., the fades were about 3 to 5 dB greater in the raw data. The loss-of-coherent-signal periods manifest themselves in Figure 14 in three ways: (1) a decrease in the average signal level, (2) rapid and deep fading, and (3) a tendency for the phase to wind up by many revolutions, followed by a recovery to a new baseline. There is no explanation for the tendency for the phase to wind up in the negative direction; it may be an artifact. A change in the baseline value was expected because of the disappearance of the charge, which was in the Path 1 line of sight.

Because dust cloud effects become stronger as the frequency increases, recovery of a sufficiently strong coherent component to make interpretation of phase shifts in terms of integrated dust density possibly takes longer at higher frequencies. The Path 1 L-band signal recovered at about $T + 2$ s, while the S- and X-band recoveries were delayed until $T + 2.5$ s and $T + 3$ s, respectively. After recovery, the phases relaxed to their new baseline values in a way consistent with the VHF results.

At about $T + 11$ s the shock wave arrived at the receiver and perturbed the system enough to knock the X-band local oscillator out of phase lock. The noise level was 10 to 13 dB below the signal level during the intense fading period T_0 to $T + 3$ s, which proves that although the coherent signal disappeared, there was some signal getting through. Note

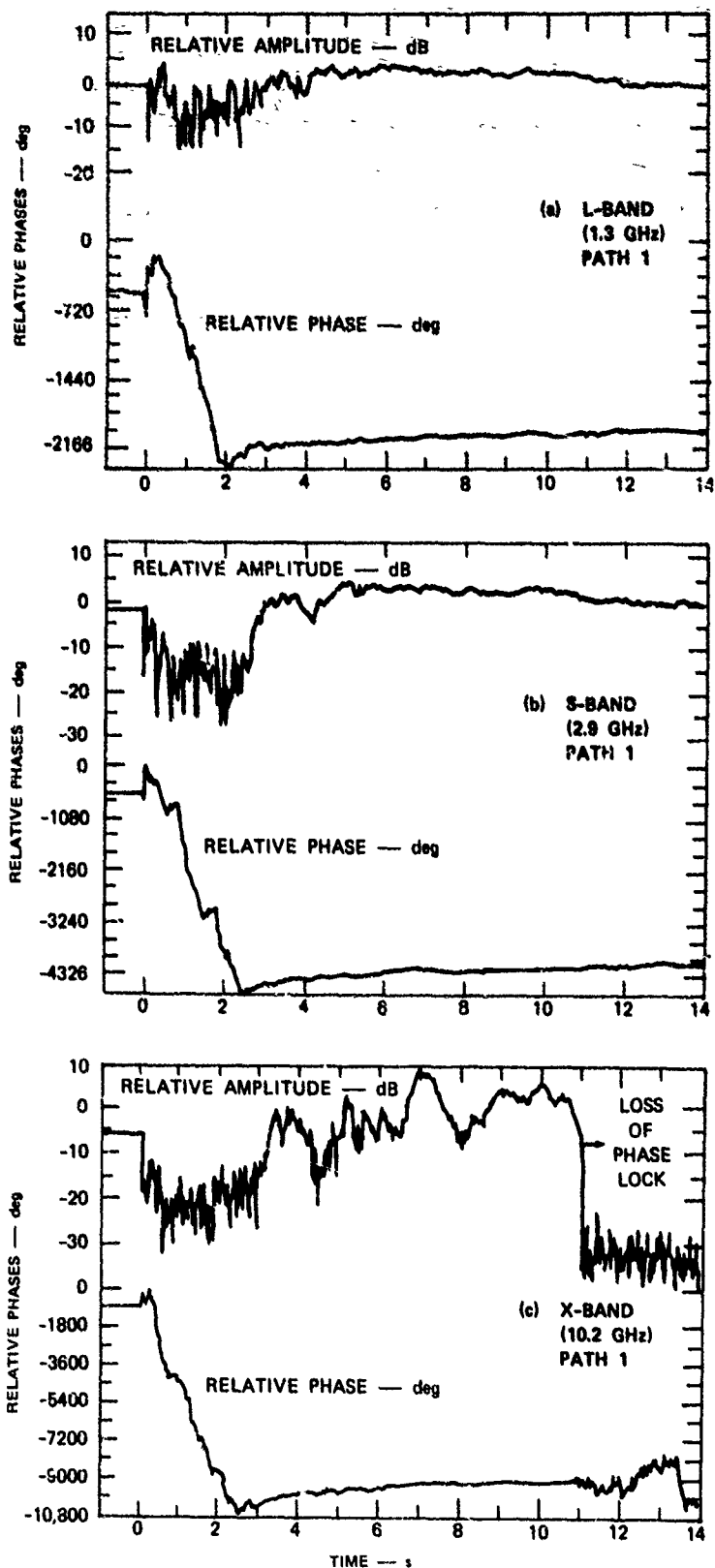
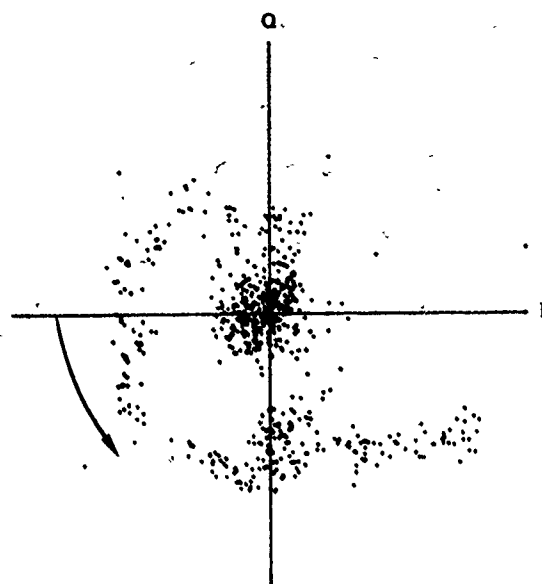


FIGURE 14 L-, S-, AND X-BAND AMPLITUDES AND PHASES FROM $T - 1$ s TO $T + 14$ s

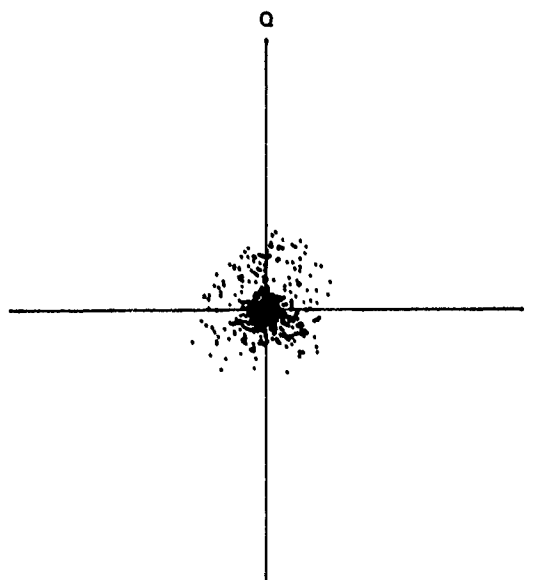
that there was no tendency for the phase to wind up in any particular direction when there was only noise present. The tendency for the phase to wind up in a preferred direction during the intense fading period was, therefore, probably a true dust-cloud effect rather than an instrumental artifact.

Figure 15 is a polar plot of the S- and X-band quadrature components from T_0 to $T + 5$ s. At S-band, before the recovery phase, which was characterized by a spiral trajectory, the signal appears to be distributed in a manner consistent with Rayleigh statistics. The L- and X-band signals behaved in similar ways except that the spiral recovery trajectory in the X-band case (Figure 15) cannot be distinguished because it performed several revolutions. Statistical computation also seem to support Rayleigh statistics at early times. Table 5 presents the results from computing various moments from the data in several time intervals. During the 0-to-2.7-s interval, the mean values were much smaller than the standard deviations, which, furthermore, were approximately equal to one another. Also, the correlation coefficient, r , between I and Q was very small. However, these results may be very misleading, for we know that the phase behaved in a very deterministic way during that interval. Table 6 lists the ratio of the variance of the L-, S-, and X-band signal power to its mean value for the 0-to-2.7-s interval. If the signals did follow Rayleigh statistics, this ratio would have been unity. Because the actual S- and X-band ratios were very different from that value, we must conclude that those signals were not fading in a Rayleigh fashion. In fact, they exhibited much greater variability than expected for the Rayleigh case, particularly at S-band.

The Path 2 and Path 3 X-band signals also experienced periods of intense fading, during which phase changes cannot be related directly to integrated dust density. Consistent with the progressive delay of the strongest effects with path offset from ground zero seen in the UHF data (Figure 12), the Path 2 and 3 X-band data are also progressively delayed (Figure 16). The strongest effects on Path 2 spanned the interval $T + 1.5$ to $T + 4.5$ s, and those on Path 3 occurred between $T + 4.5$ s and $T + 8$ s. This pattern implies that the intense fallout of larger



(a) S-BAND (2.9 GHz)



(b) X-BAND (10.2 GHz)

FIGURE 15 POLAR PLOTS OF PATH 1 S- AND X-BAND
QUADRATURE SIGNAL COMPONENTS FROM
 T_0 TO $T + 5$ s (these data have been decimated)

Table 5

PATH 1 QUADRATURE SIGNAL COMPONENT STATISTICS
IN UNITS OF DIGITIZER OUTPUT COUNTS

Band	Time Interval (s)	\bar{I}	\bar{Q}	σ_I	σ_Q	r
L	0-2.7	65	67	510	480	0.021
L	2.7-5.5	-150	-1100	490	310	-0.67
L	5-8	960	-980	310	320	0.85
S	0-2.7	-49	31	250	240	0.005
S	2.7-5.5	290	-490	980	680	0.066
S	5-8	880	920	700	760	-0.83
X	0-2.7	-5.4	-5.1	70	68	0.004
X	2.7-5.5	32	82	260	270	0.14
X	5-8	260	2.7	480	550	0.29

Table 6

RATIOS OF SIGNAL POWER VARIANCE (σ_P)
TO MEAN SIGNAL POWER (\bar{P})
IN THE T_0 -to-2.7-s TIME INTERVAL

Band	\bar{P}	σ_P	σ_P/\bar{P}
L	5.0×10^5	4.9×10^5	0.98
S	1.2×10^5	3.6×10^5	3.00
X	9.5×10^3	1.4×10^4	1.45

particles within the dust cloud struck the ground in roughly the form of a slowly expanding annulus about 80 to 95 m wide and moving outward from ground zero at about 27 m/s. The statistical nature of these signals during their respective intense fading periods paralleled that of the Path 1 signal, and leads to the same conclusion that although the fadings were similar in some ways to the Rayleigh case, they were much more

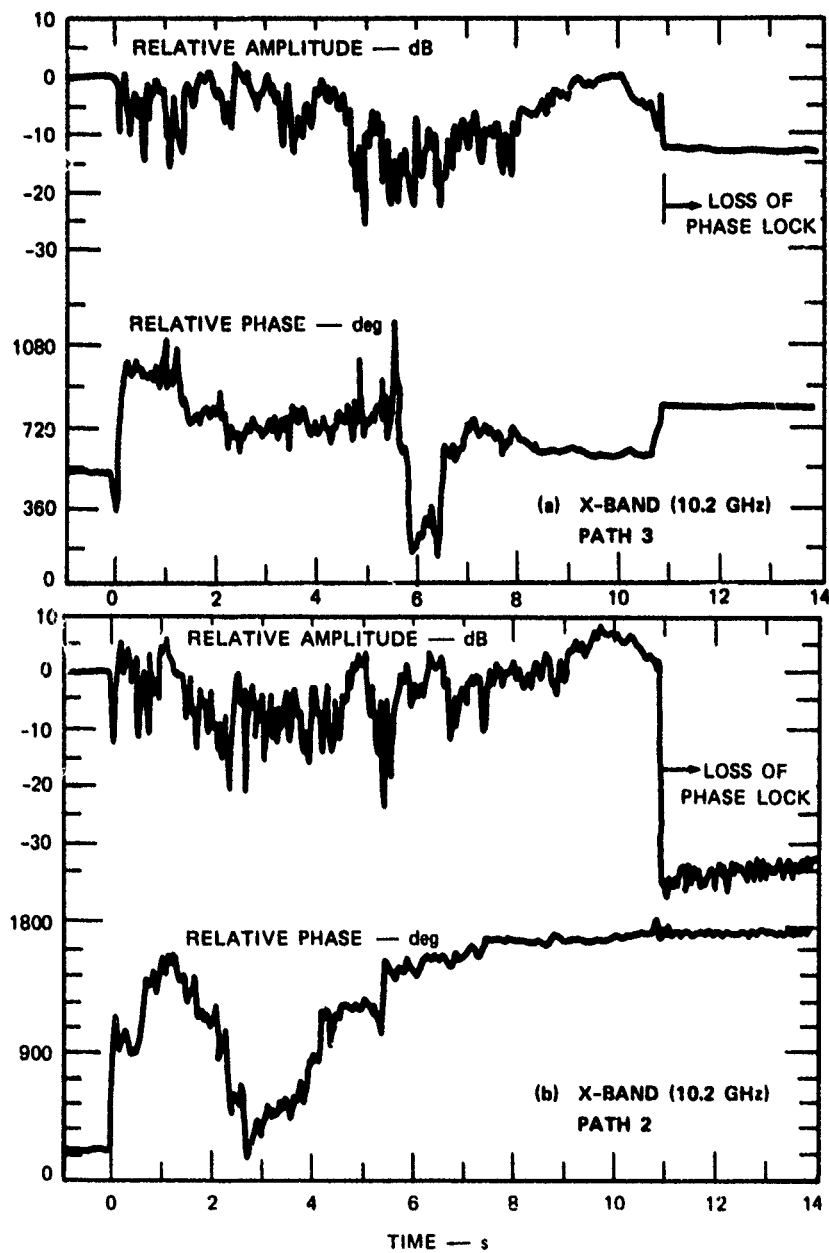


FIGURE 16 PATH 2 AND 3 X-BAND SIGNAL FLUCTUATIONS

variable. This may be due to temporal nonstationarity of conditions within the dust cloud and changes in the path lengths through the cloud with time.

Consistent with the cloud motion (Figures 5, 6, 9, and 10), the rf effects on Path 1 ceased at $T + 25.5$ s. Figure 17 shows the Path 1 S-band amplitude and phase between $T + 3$ and $T + 30$ s. Following the initial fallout, the phase shift was relatively steady at about -35° from $T + 12$ to $T + 21$ s, followed by a fairly linear return to the clear-atmosphere baseline at $T + 25.5$ s. Amplitude fluctuations were rather weak throughout this entire period. The Path 2 and 3 behaviors were similar to this except that effects terminated at $T + 22$ and $T + 15.5$ s, respectively. These times, plus the termination time of Path 1, correspond closely to a 12.5-m/s lateral cloud drift speed. The Path 2 and 3 UHF phase shifts* were about -5° to -6° before starting their return to their clear-atmosphere values. These values are consistent with the $\approx -35^\circ$ value measured on Path 1, which, using the average of the values in Table A-3, corresponds to an integrated dust density of about 2.7 g/cm^2 .

The strong surface wind and lower-than-anticipated cloud height precluded all but a grazing occultation on the upper paths. Figures 5 through 10 show that only a small part of the dust cloud intercepted Path 4. Paths 5 and 6 always remained clear of dust. Figure 18 presents the 8.9-GHz Path 4 results. For this signal, an increase of matter in the path would cause a positive phase shift; therefore, negative phase shifts are due to the heating of the air. The long-term background phase drift is shown as a dashed line in Figure 18.

According to the photographic records, the dust cloud did not intercept Path 4 until $T + 14.2$ s. All of the effects before then were caused by energy deposited by the shock wave and by the heated air in the flow field outside of the dust cloud. This is consistent with the HULL-code calculations, which predicted that the dust cloud would occupy only a

*The X-band signals were not reacquired until about $T + 58$ s, well after any effects were over.

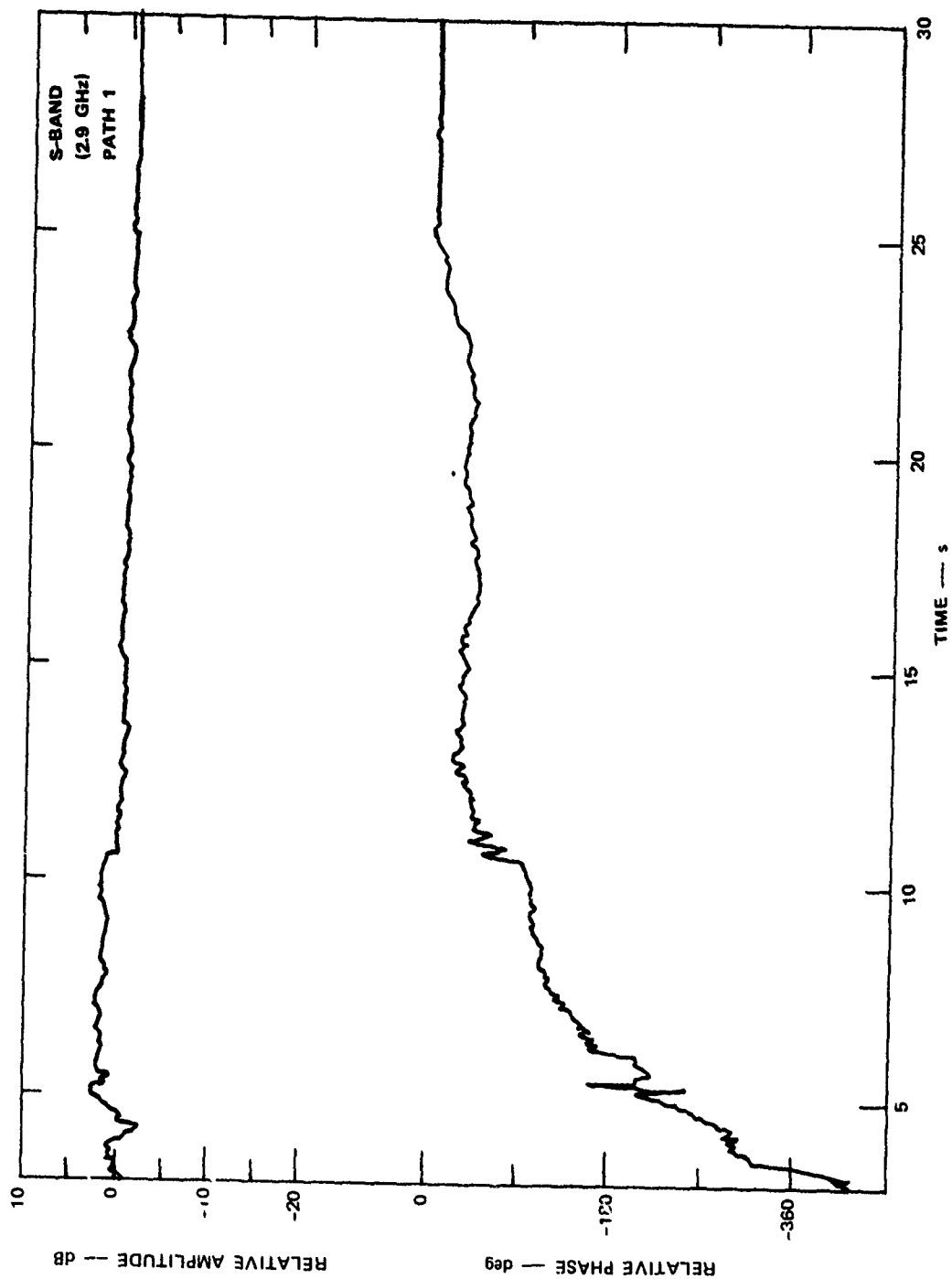


FIGURE 17 PATH 1 S-BAND AMPLITUDE AND PHASE FROM $T + 3$ s TO $T + 30$ s

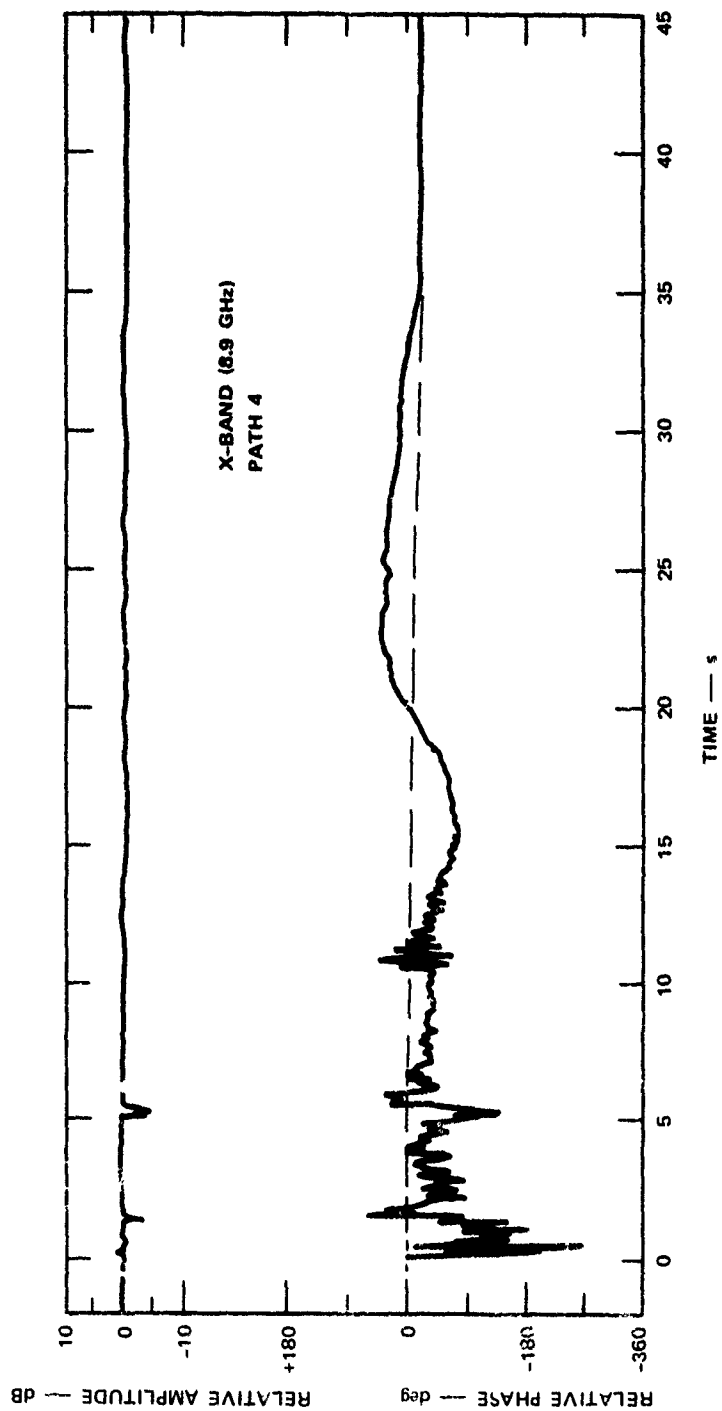


FIGURE 18 PATH 4 X-BAND SIGNAL FLUCTUATIONS

fraction of the appreciable flow field for a substantial length of time (cf., Figures B-10, B-15, B-20, and B-24). The strong phase fluctuations in the interval T_0 to $T + 6$ s were probably due to turbulence following the shock wave. That was followed by a period lasting more or less until $T + 12$ s, when the phase had a small negative value resulting from heated air in the signal path (the oscillations beginning just before $T + 11$ s were caused by the shock wave striking the receiving antenna structure). Either the volume or the temperature of the heated air increased, starting around $T + 12$ s, just preceding the dust cloud. After the dust cloud intercepted the signal path, beginning at $T + 14.2$ s, the phase began to shift in a positive direction. Both dust and heating effects were present during the occultation, and we believe that there would have been close to twice the approximately 60° peak positive phase shift measured, had there been no heating effects. That is, the phase shift due to dust of about $+120^\circ$ was partially offset by a heating phase shift of about -60° . This is a crude estimate, however, because there is no direct way to separate the two effects and it is based on the pre-occultation behavior. In agreement with the photographic data, the phase returned to its background level when the dust cloud cleared Path 4 at $T + 35$ s. For phase shifts of 60 and 120° at 8.9 GHz the corresponding integrated dust densities are 1.75 and 3.5 g/cm^2 , respectively.

Figure 19 shows the amplitude and phase of the Path 4 UHF signal, which was time-multiplexed with the Path 5 and 6 signals. Except for the opposite sign of phase changes, the effects were consistent with the S-band results. The heating effects and turbulence caused by the shock wave perturbed all of the upper-path signals (Figure 20), even though Path 6 passed 720 m away from ground zero. At UHF, however, these effects were very weak.

C. Spectral Analyses

The spectra of the complex signal fluctuations were computed for 4-s periods immediately before and after detonation. These spectra were calculated using standard fast-Fourier-transform techniques after the (complex) mean value of the data had been subtracted. Then the magnitudes

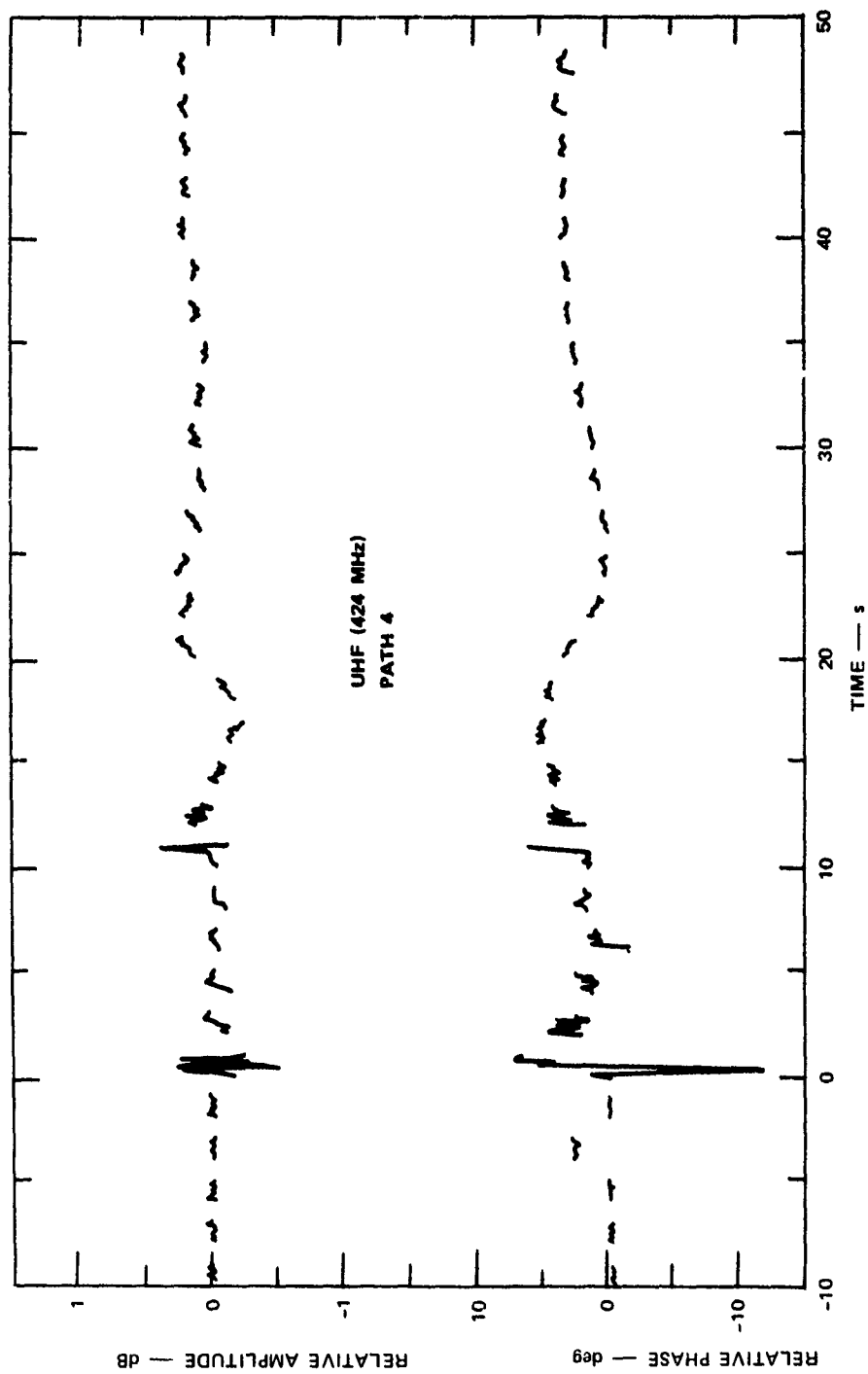


FIGURE 19 PATH 4 UHF SIGNAL FLUCTUATIONS

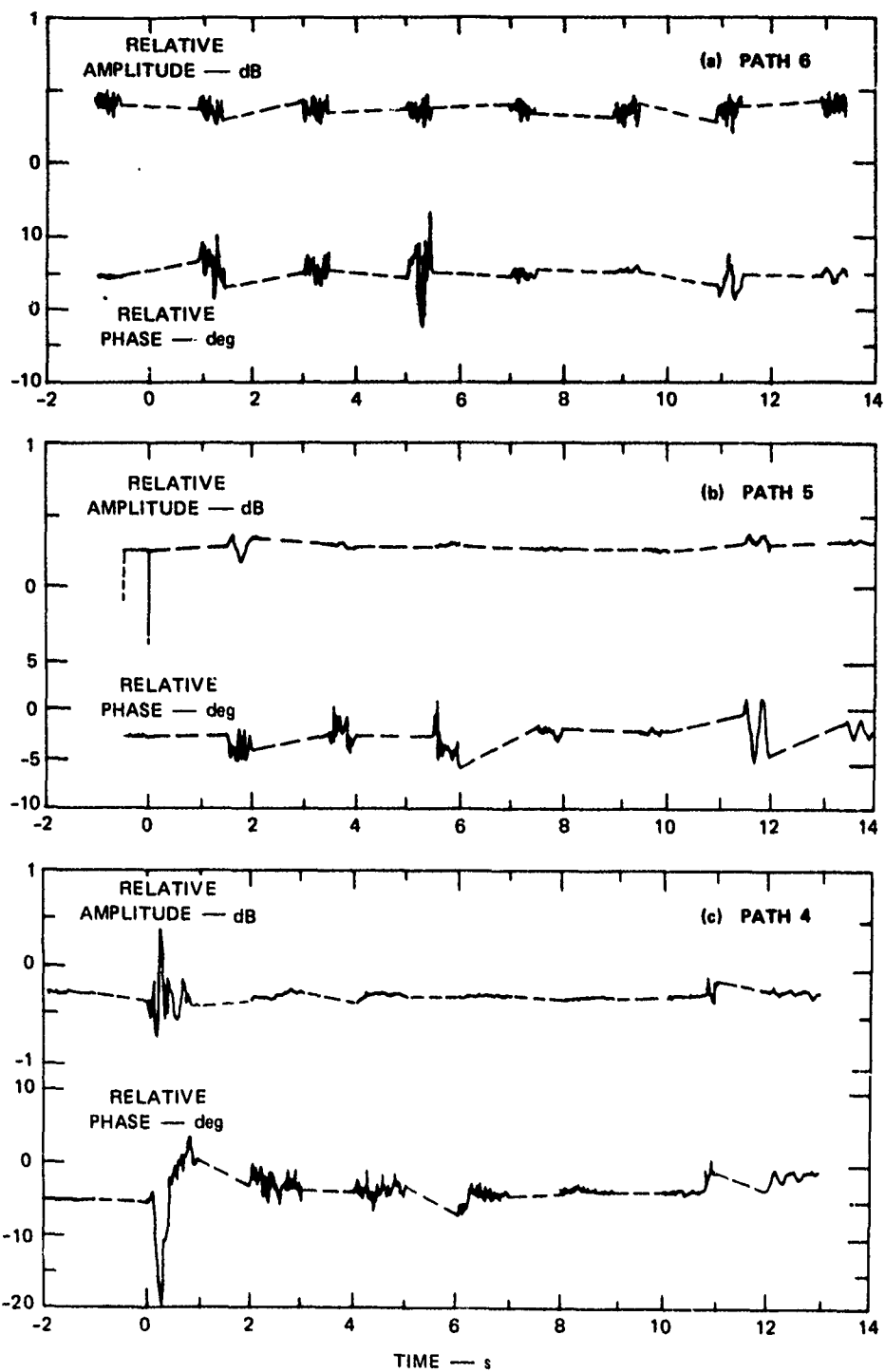


FIGURE 20 UHF SIGNAL FLUCTUATIONS FOR PATHS 4, 5, AND 6

of the positive and negative frequency components were summed, and the resulting spectra were smoothed, using a running average. Tests with some of the data using prewhitening techniques did not lead to any but differences in detail, so these more sophisticated methods were not used for the most part.

The fluctuation spectra for the various frequencies and paths were very similar to one another. Thus we will show only a few examples here. Figure 21 presents the 413-MHz Path 1 UHF spectra. After detonation, the spectrum exhibited an f^{-2} dependence. The other Path 1 UHF and the L-band spectra were virtually identical to this one, and the S-band spectrum was very similar. At X-band, however, there was less difference between the pre- and post-detonation spectra, and the spectrum was flatter below about 20 Hz (Figure 22). There also appears to be a peak between 20 and 50 Hz, which also occurred to a lesser degree at S-band. This peak also appears in the Path 3 X-band spectrum (Figure 23), which is virtually identical to the Path 1 and Path 2 spectra as well. In general, except for being slightly weaker, the post-detonation spectra for the paths offset from ground zero were the same as the ones at the same wavelength for Path 1. Furthermore, Figure 24 shows that the Path 4 X-band spectrum is only slightly different from the Path 1 spectrum (Figure 22), even though the dust cloud had not yet reached Path 4. This result may show that turbulent air density fluctuations contributed significantly to signal fluctuations for paths penetrating the dust cloud.

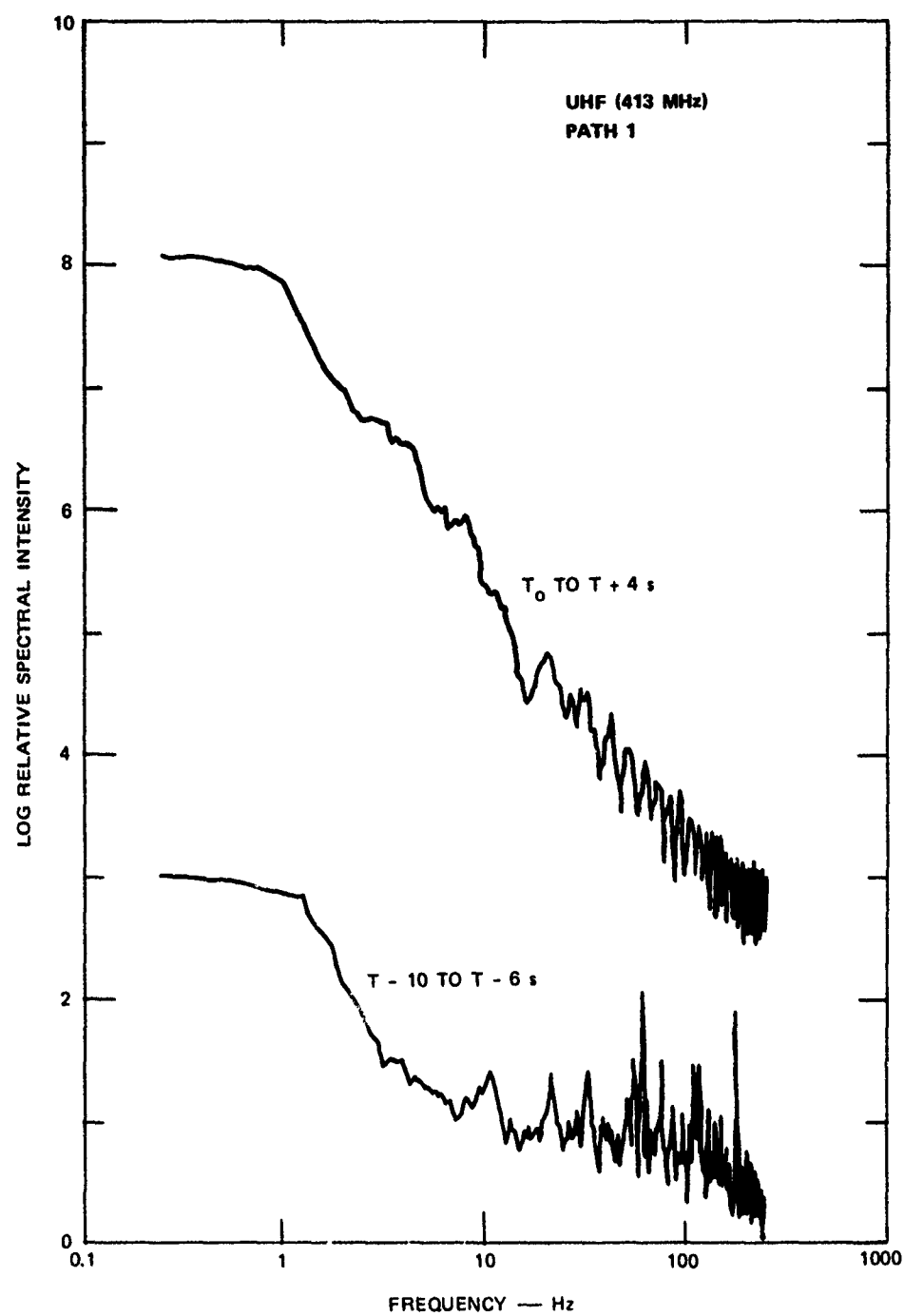


FIGURE 21 POWER SPECTRUM OF THE UHF PATH 1 COMPLEX SIGNAL FLUCTUATIONS

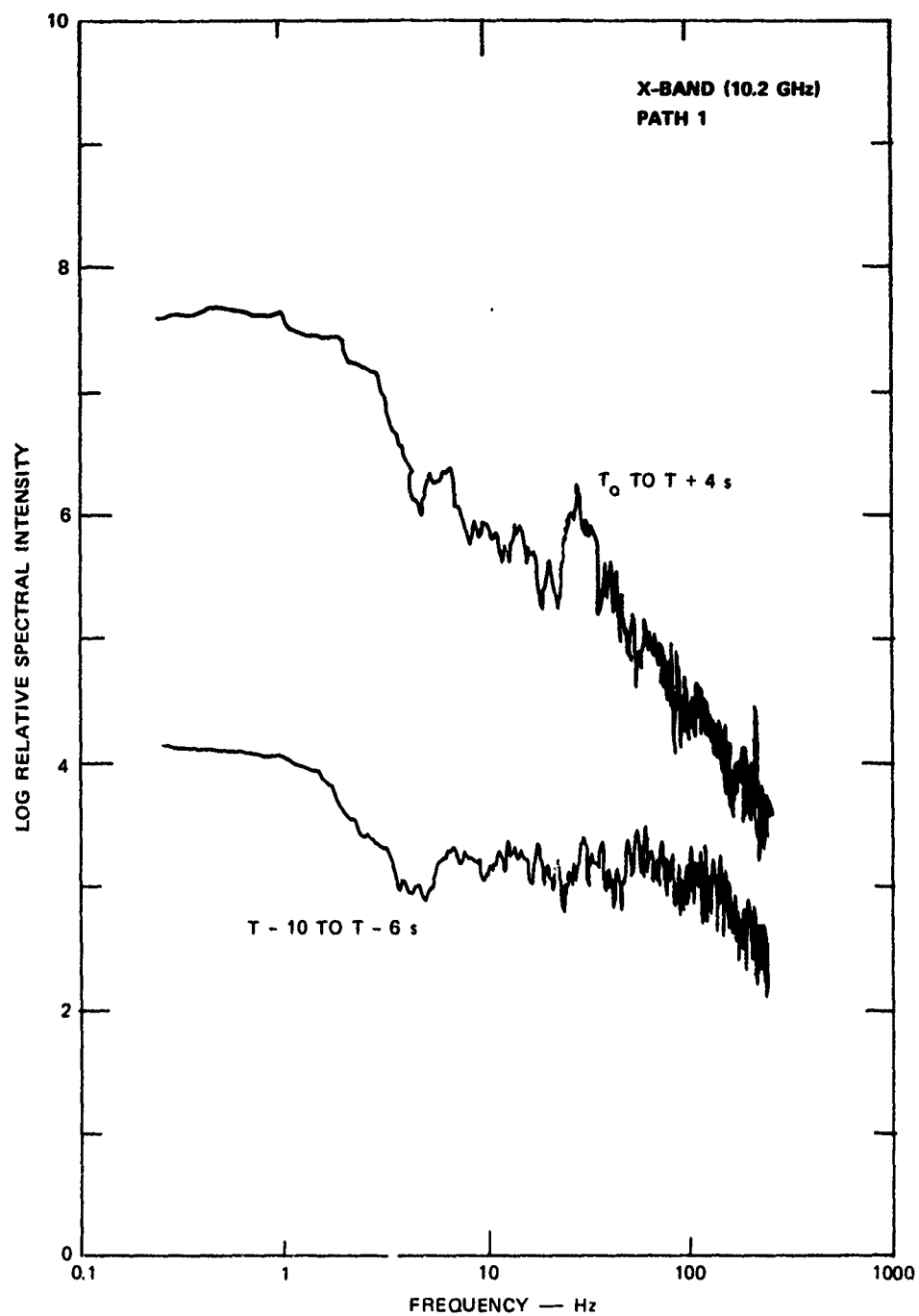


FIGURE 22 POWER SPECTRUM OF THE PATH 1 X-BAND COMPLEX SIGNAL FLUCTUATIONS

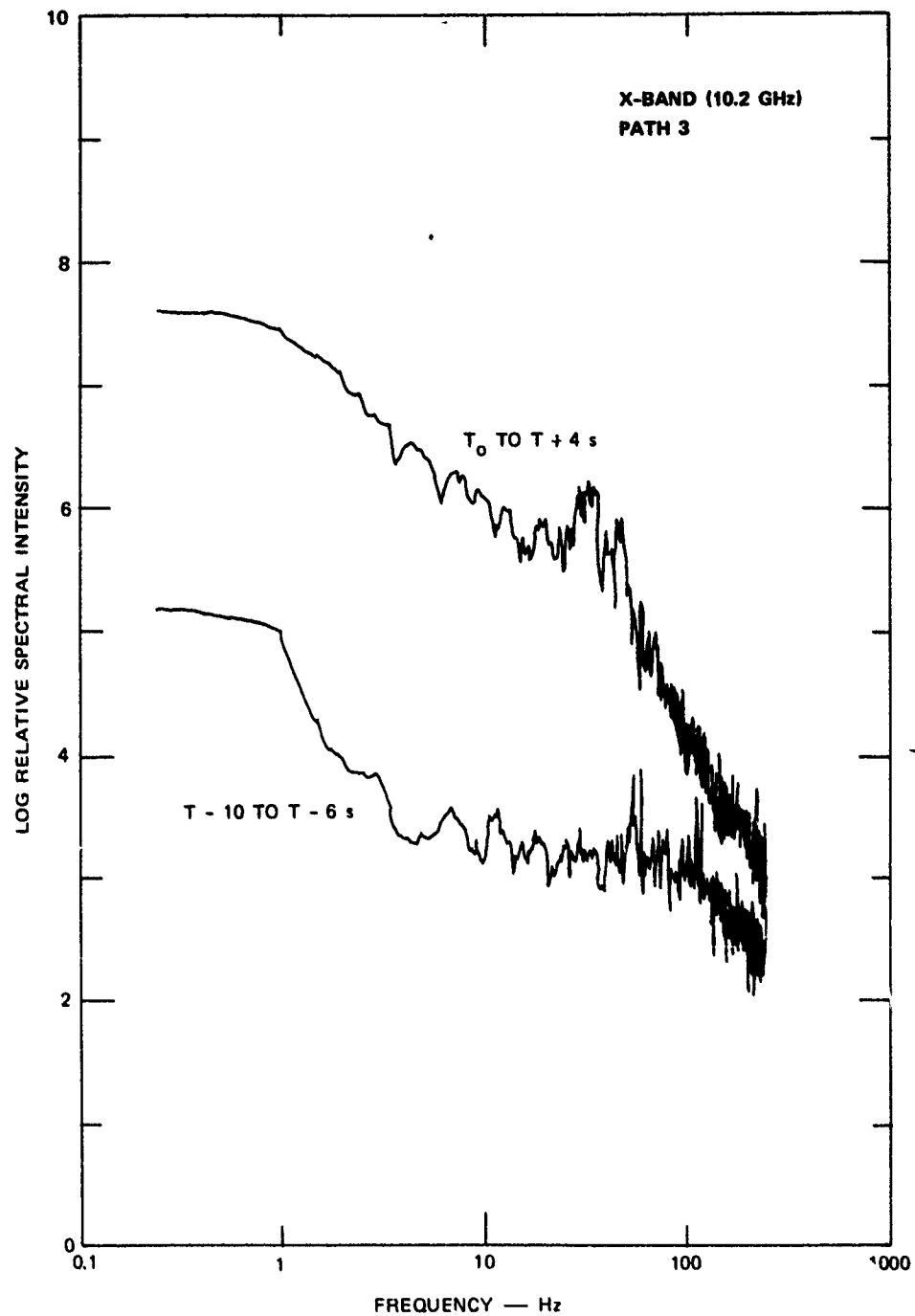


FIGURE 23 POWER SPECTRUM OF THE PATH 3 X-BAND COMPLEX SIGNAL FLUCTUATIONS

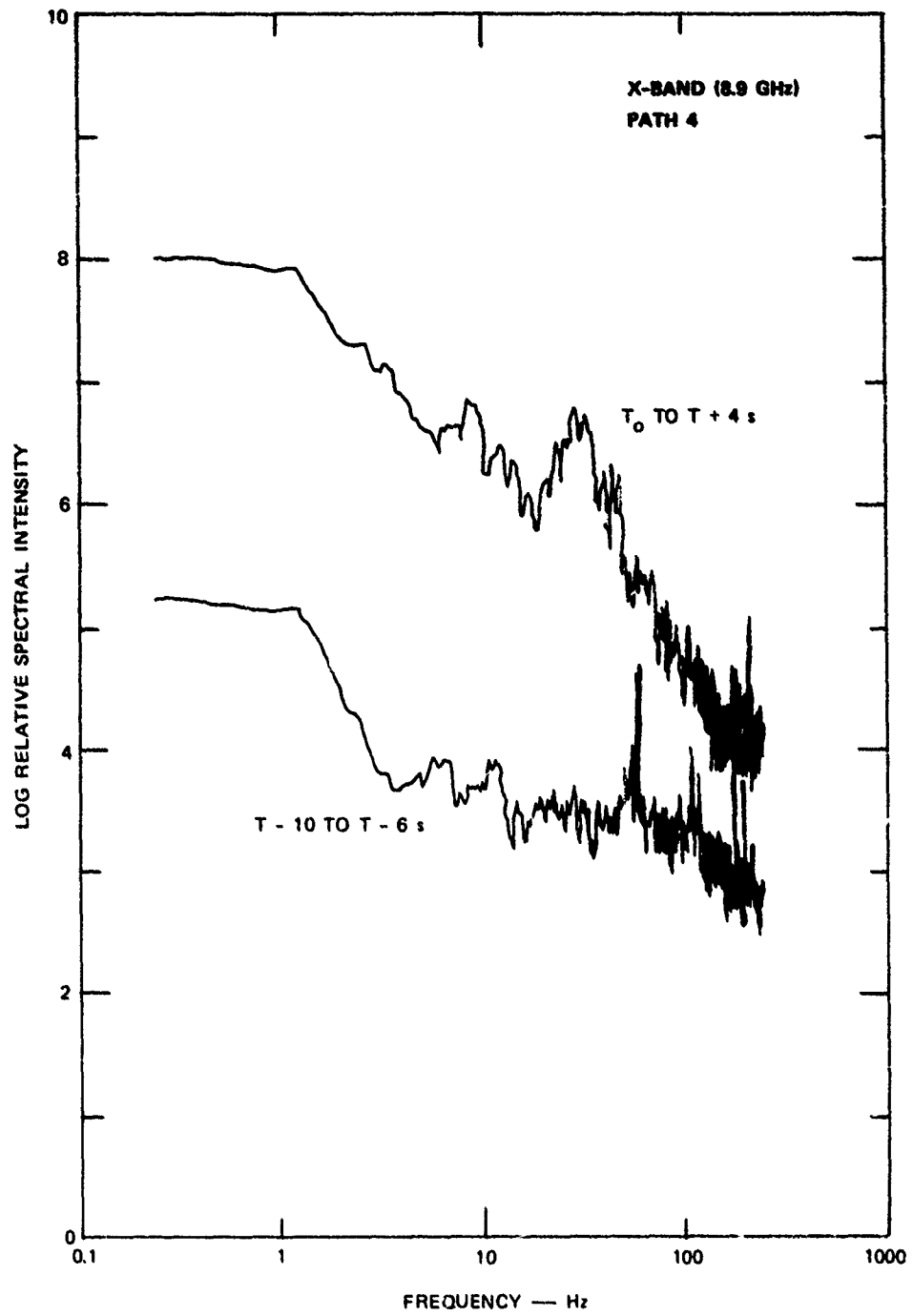


FIGURE 24 POWER SPECTRUM OF THE PATH 4 X-BAND COMPLEX SIGNAL FLUCTUATIONS

IV INTERPRETATION

Figure 25 compares the measured 413-MHz path phase shift to that computed using a simple model for the average dust density and the measured width of the cloud. As discussed in Appendix B, this model is based on the measured volume of the DICE THROW dust cloud. Figure 26, which is the same as Figure B-38, presents the average dust density as a function of time. At first, it is assumed that 10 kt of soil was aloft. As time went on, the amount of soil aloft is assumed to decrease so as to cause the average dust density to follow the interrupted line in Figure 26. After $T + 20$ s, the amount of mass aloft is assumed to have been constant, and further average dust density decreases were the result of cloud volume increases. The computed absorption is also compared to the measured amplitude fluctuations. The averages of the properties of the soil samples summarized in Table A-3 were used for these computations. Before $T + 4$ s, this model only predicts about one-third of the measured phase shift. The discrepancy can easily be accounted for by nonuniformity of dust density within the cloud.

At these early times, the dust density was certainly much greater in the center of the cloud. The much smaller phase shifts on Paths 2 and 3 (Figure 12) demonstrate that. Also, the comparison made in Figure B-4 shows that the crater was much smaller in extent than the dust cloud. Greater dust densities would be expected near the crater. Consider a simple, cylindrical model of the dust cloud in which the dust density decreases exponentially with radius from the center to the edge. For the same average density as with the uniform cloud, the peak density at the center would only have to be four times the average value to increase the phase shift by a factor of three. At the boundary, the density for this nonuniform model would be about one-third of the average value. This arbitrary model illustrates how an actually rather modest amount of nonuniformity can greatly affect the result.

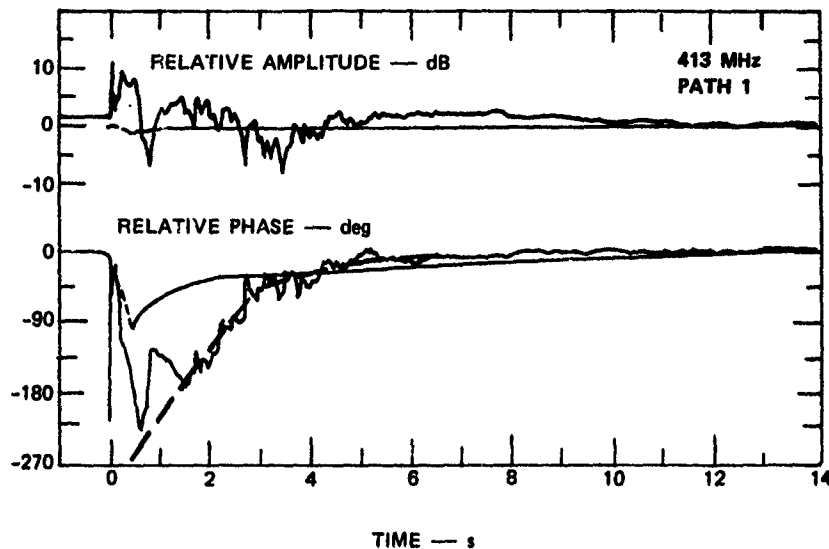


FIGURE 25 COMPARISONS BETWEEN COMPUTED ABSORPTION AND PHASE SHIFT AND MEASURED AMPLITUDE AND PHASE CHANGES

At 413 MHz, absorption was clearly negligible compared to the effects of diffractive fading. Nor is it likely that scattering losses were significant either. Of course, these conclusions apply for the small DICE THROW event, and it should be recognized that UHF systems are not automatically immune from degradations due to dust clouds.

Distortions caused by the very complex diffraction phenomena make it very difficult to determine the time-phase-shift-versus-time behavior. The interrupted curve in Figure 25 represents our best estimate of the 413-MHz phase shift. We believe that that signal underwent a phase shift larger than that measured before $T + 2$ s because of the positive phase shift seen on Path 2 (Figure 12), where the fading pattern was very similar to that of Path 1.

The interrupted curve in Figure 25 is the basis for computing the absorption at higher frequencies. Figure 27 shows comparisons between the computed absorption and the actual signal power fluctuations measured at L-, S-, and X-band. At all three frequencies, the computed absorption was less than the measured signal-strength decline. The rest of the loss was caused by scattering. At L-band, the total extinction curve appears to have roughly the same shape as the calculated absorption curve. Even

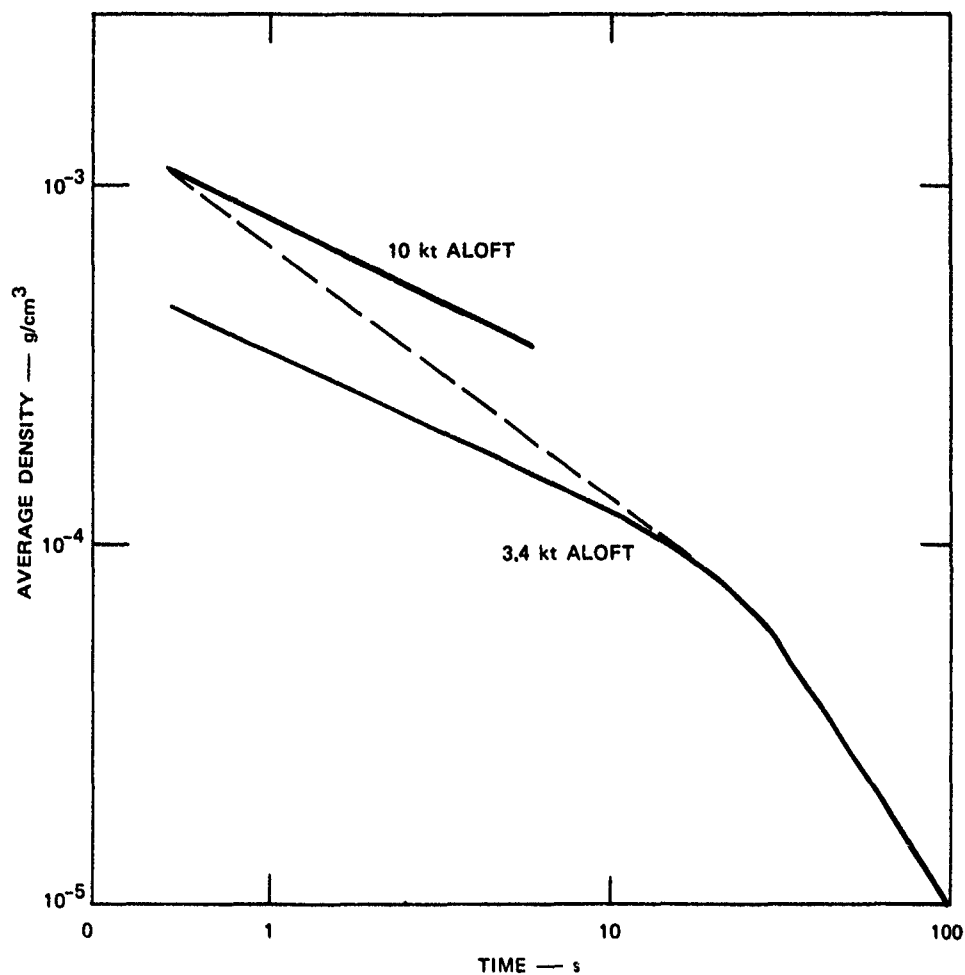


FIGURE 26 AVERAGE DUST DENSITY IN DICE THROW CLOUD INFERRED FROM VOLUME MEASUREMENTS

though the coherent signal was lost during part of the time, the scattering loss, which was approximately equal to the absorption loss, was proportional to the integrated dust density along the signal path.

That was not the case at S- and X-band. Both of those signals experienced a sort of saturation effect, whereby the signal amplitudes fell to low, but steady (except for short-term fluctuations) values until rather rapid recoveries occurred. Note that the recovery at S-band significantly preceded that at X-band. This means that the recovery was not caused by a simple decrease of material in the signal path. Unlike the

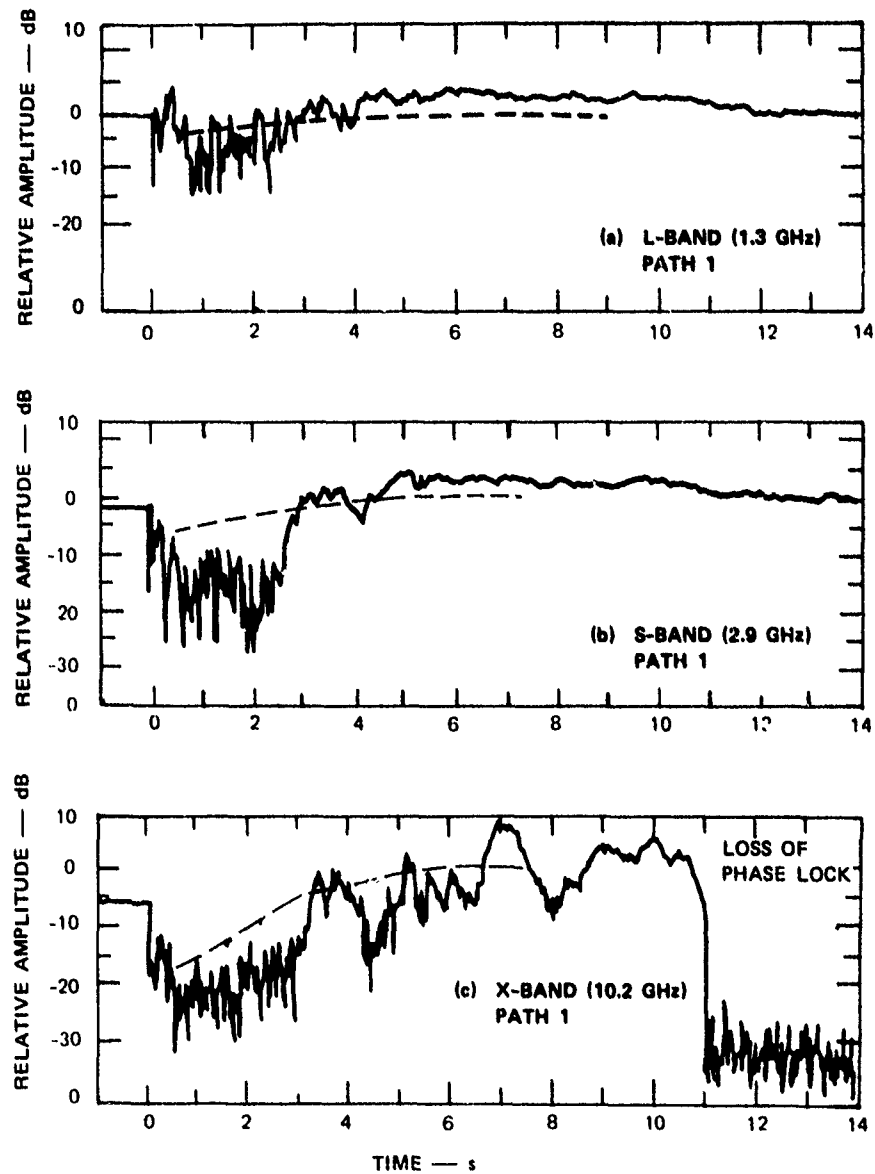


FIGURE 27 CALCULATED ABSORPTION COMPARED TO MEASURED AMPLITUDE FLUCTUATIONS AT L-, S-, AND X-BANDS

L-band case, multiple scattering evidently was very important at the two higher frequencies. One of the effects of multiple scattering would be to redirect energy back into the forward direction, thus limiting the amount of scattering loss. Multiple scattering is also apparently the explanation why the measured extinction in decibels was not approximately proportional to frequency. Based on the S-band result, there should have been a 45-dB signal decrease at X-band.

As the dust density decreased and larger particles fell out, a critical value of density or of the size-distribution parameter, γ , was reached and the extinction decreased dramatically. Because the integrated dust density was changing very gradually, and, as discussed in connection with Figures A-6 and A-7, because of the extreme sensitivity of the scattering loss to the value of γ , this threshold was probably primarily controlled by the size-distribution parameter.

In Section III-B we noted that after initial fallout, the phase shifts (see Figure 17) corresponded to an integrated dust density of 2.7 g/cm^2 . This value stayed rather constant until the dust cloud was blown out of the signal path. During this time interval (i.e., $T + 10 \text{ s}$ to $T + 20 \text{ s}$), the cloud was about 560 m across (Figure B-34), giving an average dust density of $4.8 \times 10^{-5} \text{ g/cm}^3$. The Path 4 occultation (see Figure 18) gave rise to a phase shift that corresponded to a maximum integrated dust density of about 3.5 g/cm^2 . However, because the signal path penetrated only a small part of the cloud, the maximum affected path length was only about 125 m. Thus the average dust density in that upper part of the cloud was approximately $2.8 \times 10^{-4} \text{ g/cm}^3$. After the initial fallout phase, the dust density apparently was much greater on the upper parts of the cloud than toward the base. Our crude model based on measured cloud volume and estimates of soil initially lofted and of that eventually missing from the crater predicted dust densities (Figures 26 and B-38) that are in reasonably good agreement with these values.

A dust cloud density in the range of 10^{-4} to 10^{-3} g/cm^3 is also consistent with observed attenuation and computed extinction. If multiple-scattering phenomena are ignored and all of the attenuation is

accounted for by scattering loss, the extinction coefficients at S- and X-bands are roughly 7 and 10 dB/km respectively. According to the results shown in Figure A-6 for our simple extinction model, the average cloud mass density would only have to be about 10^{-4} g/cm³ for $\gamma = 3.5$. Because of the effects of multiple scattering, this can be considered an upper limit, within the accuracy of the model. This means that large particles comprising only a small fraction of the mass in the dust cloud can easily account for the measured extinction, giving a consistent interpretation of the observed behavior.

As the larger particles fell out, the effective value of γ decreased until scattering losses suddenly diminished. However, the total mass in the dust cloud apparently declined only a little during that time. According to Figure A-5, the X-band result shows that there were a substantial number of particles larger than 0.1 cm in the signal path until about $T + 3$ s. Since the critical particle size at L-band was about 1 cm, there were numerous particles larger than that present.

In general, except when the threshold combination of density and γ was exceeded, rf effects were fairly mild. Most of that can be ascribed to the small size of the DICE THROW event. In the nuclear situation, however, where much larger amounts of soil can be lofted over much larger areas and volumes for much longer periods of time, the cumulative effect of even low-density dust clouds over long signal paths could be very serious. And, once the threshold is crossed, a signal can deteriorate very quickly. It is probable that the fallout of very likely less than a few percent of the total lofted mass during DICE THROW effectively led to signal recovery at the higher frequencies. Conversely, a patch of particles within a much larger cloud having characteristics exceeding the threshold could lead to a decline in signal strength and quality even though the density changed very little. Furthermore, the loss of a coherent signal component would cause a very serious decline in signal quality for many systems that could otherwise compensate for large changes in signal levels.

V CONCLUSION

The DICE THROW UHF/SHF coherent-transmission experiment was generally very successful. Although three signals were lost after the detonation due to shockwave effects, all 14 signal channels functioned properly for at least the first 10 seconds, during which the most significant rf effects occurred. There is fairly good agreement between the computed effects using a very simple model of the dust cloud and the measured signal perturbations. A consistent explanation of the effects is thereby obtained.

For much of the time, the DICE THROW rf effects were very mild. Most of this can be ascribed to the small size of the detonation. Besides that, the capped-cylinder ANFO charge configuration also tends to produce low flow-field velocities, resulting in rapid fallout and early cessation of strong effects. Worse yet, the downdraft in the center of the flow field intensifies the fallout rate of large particles. Even at the same yield, in the nuclear situation the higher velocities and the updraft would keep larger particles and more overall mass aloft for much longer periods of time. Strong rf degradations and perturbations would, therefore, be expected to persist much longer than simple yield-scaling would predict. Scaling from the DICE THROW configuration to the nuclear situation needs to be quantified.

The onset of and, more significantly, the decay of strong effects were very sudden. There appears to have been a threshold combination of dust density and particle-size distribution. Once the threshold was crossed, average extinction coefficients rose to as much as 10 dB/km. Locally, this attenuation must have been much larger, perhaps reaching 30 dB/km or more. This was accompanied by complete losses of the coherent signal components, and apparently, multiple scattering became dominant. Besides the large decrease in average signal strength, very strong fading

also occurred, which was more variable than Rayleigh fading. All of these effects were frequency dependent, becoming worse as the frequency increased.

Inferred average dust densities ranged between 10^{-5} and 10^{-3} g/cm³, depending on the part of the DICE THROW cloud in the signal path and on the time after detonation. However, even though the average density along a signal path was low, nonuniformity apparently caused the threshold condition to be crossed locally, resulting in very large losses from the higher-density patches. It would be likely that in the nuclear case the threshold would be exceeded for much longer periods of time and that scattering losses would be similar to those responsible for the extinction coefficients measured during DICE THROW. The possibility of encountering local high-loss patches within a cloud should be considered when evaluating the performance of any given system. Attenuation in such patches could be as great as 30 dB/km at S-band and above.

Although they are not as dramatic, the effects of a low-density or relatively homogeneous cloud of sufficient extent must be considered as well. In that case, the attenuation, which is dominated by absorption, could become sufficiently large to affect certain systems. Even at UHF, where the effects of dust clouds are fairly weak, the attenuation could be greater than tolerable for a low-margin system. For example, suppose there were a 30-km-wide region of dust having an average density of 3×10^{-5} g/cm³. Then, using the average dielectric properties of the DICE THROW soil samples, the absorption would rise from a possibly significant 1.4 dB at 300 MHz to a definitely serious value of 14 dB at 10 GHz.

Unlike scattering losses, absorption is proportional to the loss tangent of the material comprising the dust particles, and is therefore very sensitive to moisture content. In the nuclear situation, then, the effects of heating by the hot fireball on the soil lofted needs to be considered. The amounts of water vaporized and recondensed are the important questions. If a large amount of water initially locked up in crystalline structures were liberated, it is conceivable that absorption

losses could be greater after recondensation than for the same cloud composed of unheated particles. Although predicted temperatures were several hundred degrees Celsius above ambient in the DICE THROW cloud for a number of seconds, heating effects were undoubtedly not as significant as they would have been for a nuclear detonation of the same yield. Nevertheless, heating of clear air outside the dust-laden region in the DICE THROW flow field resulted in a phase shift comparable in magnitude to that produced by the dust. This effect tended to enhance refractivity gradients, which in turn would lead to more fading and dispersion.

A test such as DICE THROW only reproduces some aspects of the nuclear environment. In general, rf effects were weaker than would be expected from a nuclear event that lofted the same amount of soil initially. However, the results from the DICE THROW UHF/SHF coherent transmission experiment showed that very serious signal degradations can occur and that there are a number of interacting phenomena that need to be considered.

Appendix A

EFFECTS OF DUST CLOUDS ON ELECTROMAGNETIC PROPAGATION

1. Introduction

Figure A-1 summarizes the phenomena associated with the interaction of electromagnetic waves with dust clouds. Part of the incident energy is absorbed by the dust cloud. Matter in the dust cloud also causes differential phase retardations, causing irregular emergent wave fronts, which in turn lead to angle-of-arrival fluctuations and diffractive phenomena associated with propagation over distance that manifest themselves as scintillations or fading behavior. Frequency-selective fading (coherent-channel-bandwidth reduction) can also occur. Under most circumstances (e.g., when all the dust particles are small compared to the wavelength), absorption and phase shifts are thought to be closely related aspects of the same phenomenon--a change in the bulk complex dielectric properties

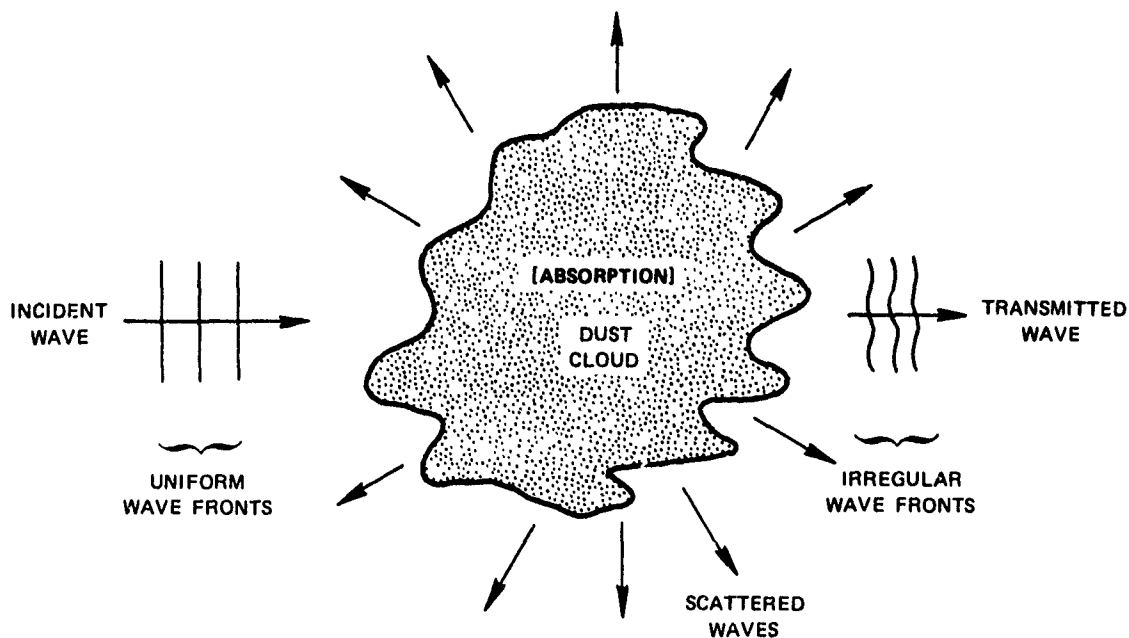


FIGURE A-1 RF PROPAGATION AND DUST CLOUDS

of the propagation medium (dust-laden air) that can be related to the mass-density and electromagnetic properties of the individual solid grains. Under the small-particle approximation, the particle size distribution does not affect the results.

Besides the absorption loss, scattering losses also contribute to the extinction, or attenuation, of the electromagnetic waves. Unlike absorption, which is usually treated as a coherent, bulk (or "fluid") phenomenon, scattering is considered an incoherent or semicoherent phenomenon that depends crucially either on the particle size distribution, the spectrum of (turbulent) dust density fluctuations, or both.

Backscatter, which can cause radar clutter interference, is only one aspect of the scattering problem. Indeed, all the phenomena mentioned above are merely different aspects of the same thing--the interaction of the electromagnetic energy with matter in a grain of dust. However, rather than trying to treat this interaction in a general way, it has been far more convenient to study its different aspects in more restrictive ways that try to isolate the most important and relevant parameters for the application. The division into coherent and incoherent or semicoherent effects mentioned above is an example.

Several aspects of the interaction of electromagnetic waves with dust clouds have been reported on by SRI International as part of this or closely related work. Bollen et al.⁵ considered the bulk phase shift and scattering loss problem in the DICE THROW effects-predictions part of their discussion of dust clouds and crater ejecta from nuclear and HE detonations. Burns and Winkleman³ related measured solid-grain dielectric and absorptive properties to those of the DICE THROW Main Event dust cloud. Chesnut⁶ investigated the relative intensities of incoherent backscattering and backscattering from density fluctuations in turbulent dust clouds. This appendix is primarily a summary of the results in those reports, which will be used to interpret the experimental results.

2. Bulk Absorption and Phase Shift

The relationship between the dielectric properties of powders (a dust

cloud is a very-low-density powder) and those of the solid grains is specified by a so-called "mixing formula." Some experimental evidence⁷ supports the use of the Rayleigh mixing formula,

$$\frac{1}{\rho_d} \left(\frac{\epsilon_d - 1}{\epsilon_d + 2} \right) = \frac{1}{\rho_s} \left(\frac{\epsilon_s - 1}{\epsilon_s + 2} \right) \quad (\text{A-1})$$

where

ρ_d = Mass density of powdered material

ρ_s = Mass density of solid grains

ϵ_d = Complex relative dielectric constant of powder

ϵ_s = Complex relative dielectric constant of solid.

This formula, which is closely connected to the Lorentz-Lorenz or Clausius-Massotti equations,^{8,9} is based on the approximation that all the grains have induced dipole moments. This means that they are all smaller than the wavelength and are Rayleigh scatterers. The forward (i.e., in the direction of propagation) scattered waves add up coherently according to the Ewald-Oseen extinction theorem in such a way that the properties of the resulting wave can be obtained using Eq. (A-1).

The resulting absorption, α , and phase constants, β , for waves in dust clouds are:³

$$\alpha = \frac{9}{2} k \left(\frac{\rho_d}{\rho_s} \right) \frac{\epsilon_r \tan \delta}{(\epsilon_r + 2)^2} \quad (\text{A-2a})$$

and

$$\beta = k \left[1 + \frac{3}{2} \left(\frac{\rho_d}{\rho_s} \right) \left(\frac{\epsilon_r - 1}{\epsilon_r + 2} \right) \right] \quad (\text{A-2b})$$

where

$k = 2\pi/\lambda$ = Wave number

ϵ_r = Real part of ϵ_s

$\tan \delta = \epsilon_i/\epsilon_r$ = Loss tangent

ϵ_i = Imaginary part of ϵ_s

ρ_d/ρ_s = Relative dust cloud density.

Thus, in a distance d , Eq. (A-2) predicts that there will be

$$\varphi = \frac{3}{2} k \left(\frac{\rho_d}{\rho_s} \right) \left(\frac{\epsilon_r - 1}{\epsilon_r + 2} \right) d \quad (A-3)$$

radians of extra phase shift and

$$a = 39.1 k \left(\frac{\rho_d}{\rho_s} \right) \frac{\epsilon_r \tan \delta}{(\epsilon_r + 2)^2} d \quad (A-4)$$

decibels of absorption through the dust cloud. Hence, for every radian of excess phase shift, there will be

$$26.1 \frac{\epsilon_r \tan \delta}{(\epsilon_r - 1)(\epsilon_r + 2)} \quad (A-5)$$

decibels of absorption, independent of dust cloud density.*

Our measurements³ of DICE THROW soil samples showed that the loss tangent should be broken into an "intrinsic" loss term and a "conduction" loss term:

$$\tan \delta = \tan \delta_o + \frac{\sigma_o}{\omega \epsilon_o \epsilon_r} \quad (A-6)$$

The intrinsic loss term, $\tan \delta_o$, and the conductivity, σ_o , and ϵ_r , were found to be nearly independent of frequency from 0.1 to 12 GHz [$\epsilon_o = (36\pi \times 10^9)^{-1}$ in MKS units]. Table A-1 summarizes the measurements made on the three DICE THROW soil samples collected after the event from the crater and lip ("sand," "caliche A," and "caliche B"). While ϵ_r did not change significantly as the samples were dried, both $\tan \delta_o$ and σ_o were very sensitive functions of moisture content. The solid-grain properties inferred using the Rayleigh mixing law are given in Table A-2 for 1 and 10 GHz.

* Equation (A-5), and some equations leading to the equivalent of Eq. (A-2a), were in error in Ref. 3; the conclusions drawn there were unaffected, because the effects of the errors were slight.

Table A-1

SUMMARY OF DIELECTRIC PROPERTY MEASUREMENTS

Sample	Moisture Content (percent)	Density in Fixture (g/cm ³)	ϵ_r		$\tan \delta_o$	σ_o (mmho/m)
			1 GHz	10 GHz		
Sand (undried)*	2.74	1.521	2.9	2.5	0.025	2.4
Sand (dried) [†]	≈ 0	1.512	2.7	2.5	0.004	$< 5 \times 10^{-3}$
Sand (dried and exposed) [‡]	0.90	1.549	2.8	2.5	0.008	$< 10^{-2}$
Caliche A (undried)	12.73	1.207	2.8	2.4	0.024	3.1
Caliche A (dried and exposed)	3.38	1.200	2.5	2.1	0.007	$< 10^{-2}$
Caliche A (dried)	≈ 0 0	1.201	2.4	2.1	0.006	$< 10^{-2}$
Caliche B (undried)	9.03	1.472	3.0	2.7	0.021	1.4
Caliche B (dried)	≈ 0	1.388	2.6	2.2	0.007	$< 10^{-2}$

* As collected.

[†] Baked for 4 days in vacuum chamber at 110°C.[‡] Exposed to ambient conditions for several days after being dried.

Table A-2

INFERRED AVERAGE DIELECTRIC CONSTANT, MOLECULAR LOSS TANGENT, AND CONDUCTIVITY FOR SOLID PARTICLES

Sample	Solid-Particle Density (g/cm ³)	Moisture Content (percent)	f (GHz)	Solid-Particle Properties		
				ϵ_r	$\tan \delta_o$	σ_o (mmho/m)
Sand	2.56	2.74	1	6.6	0.051	4.9
			10	4.8	0.043	4.1
Caliche A	2.64	12.73	1	14.7	0.11	14.2
			10	7.9	0.072	9.3

The curves shown in Figure A-2 result from inserting the parameter values listed in Table A-2 into Eq. (A-5). The conductivity term does not appreciably contribute to absorption above about 1 GHz. Table A-3 lists the excess phase retardation and absorption per kilometer normalized to a uniform dust cloud density of 10^{-3} g/cm^3 at several frequencies in the 0.3-to-10-GHz range for the DICE THROW samples. Finally, Figure A-3 presents the excess phase retardation and absorption per kilometer as a function of uniform dust density computed at 1 and 10 GHz. The dielectric property measurements and calculations presented in this appendix were used to interpret the experimental results.

3. Scattering Loss

The other component of extinction is loss due to energy scattered away from the forward direction. Two processes are responsible for the scattering.⁶ The first process is incoherent scattering, where the power scattered from each grain is summed for all of the grains. Chesnut⁶ has termed the other process "semicoherent." This type of scattering arises from nonuniformities in the particulate cloud density, and depends on the strength and scale size of the density fluctuations. It is termed "semicoherent" because scattered fields from nearby particles are added coherently. A limiting case is the example of a perfectly uniform dust cloud where the only density discontinuity occurs at its edge; then the scattering can be found using the results of the preceding section to determine boundary reflection coefficients. In that example, scattering from the grains acts in a completely coherent way within the cloud. However, very abrupt boundaries (i.e., transition distances small compared to the rf wavelength) are required to cause appreciable scattering. In general, incoherent scattering has been consistently considered the dominant process of scattering from particulate clouds.

Because incoherent-scatter strength depends strongly on the particle-size-distribution function, it is necessary to adopt a model for the grain size function in a dust cloud. Although there is very little or no theoretical justification for such a choice, an inverse-power-law function is apparently often picked on the basis of empirical, soil-sieving evidence.

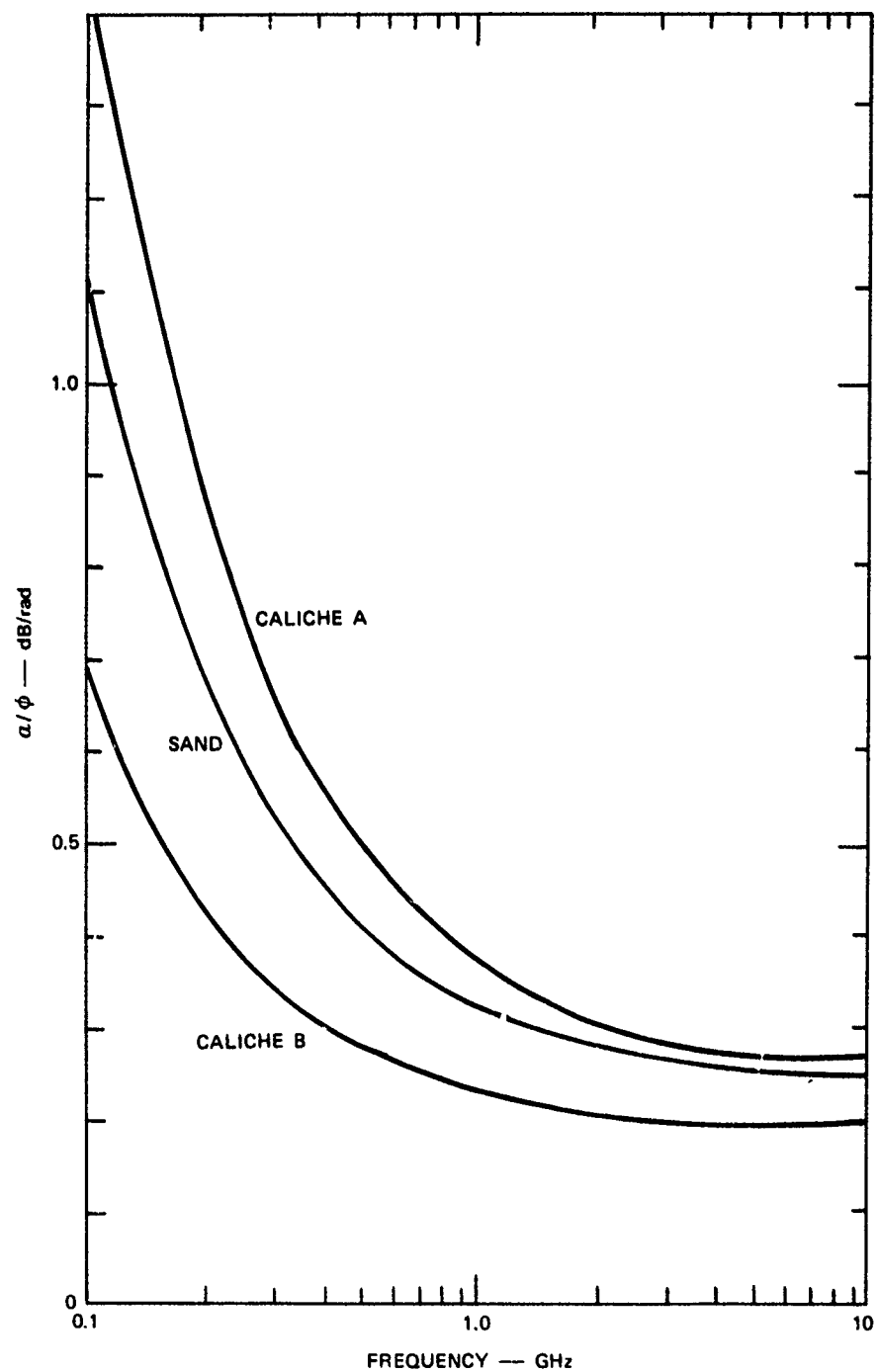


FIGURE A-2 ATTENUATION PER RADIAN (a/ϕ) EXCESS PHASE SHIFT vs FREQUENCY

Table A-3
EXCESS PHASE RETARDATION AND ABSORPTION VERSUS FREQUENCY AT 10^{-3} g/cm^3 DUST CLOUD DENSITY

Frequency (GHz)	Sand		Caliche A		Caliche B		Average	
	φ/d (rad/km)	a/d (dB/km)	φ/d (rad/km)	a/d (dB/km)	φ/d (rad/km)	a/d (dB/km)	φ/d (rad/km)	a/d (dB/km)
0.3	2.5	1.4	3.1	2.1	2.7	1.0	2.8	1.5
1.0	7.2	2.3	8.8	3.3	7.7	1.8	7.9	2.5
3.0	22	6.0	27	7.6	20	4.1	23	5.9
10.0	61	15	74	20	70	14	68	16

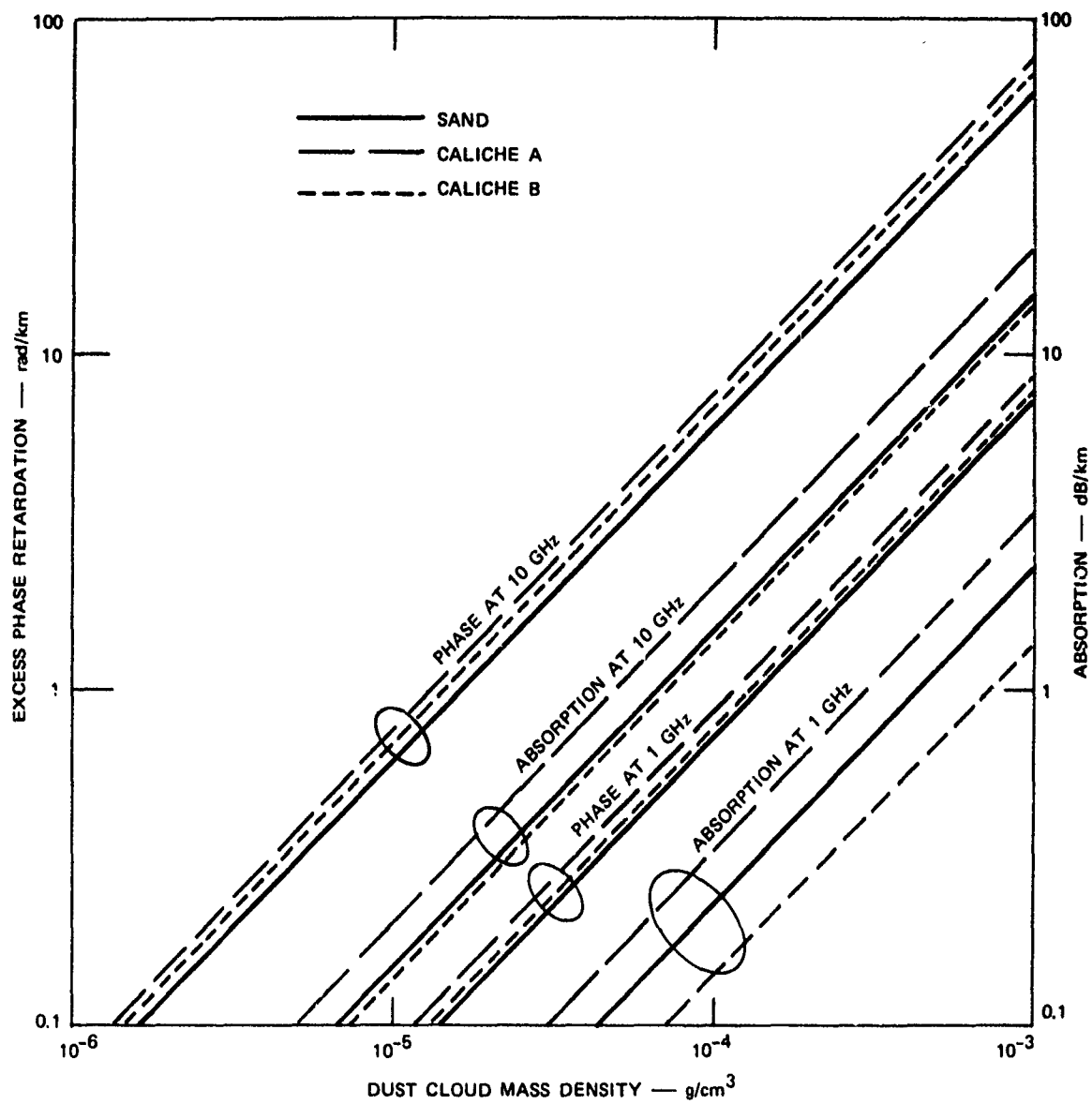


FIGURE A-3 EXCESS PHASE RETARDATION AND ABSORPTION PER KILOMETER

As an example, this is the choice made by Kownacki and Welty,¹⁰ and it is the choice made here, although we will modify it somewhat. Then, if a is the grain size (e.g., the radius, for spherical grains),

$$n(a) = Ka^{-\gamma} \quad (A-7)$$

is the number of particles per unit volume between a and $a + da$. Typical values for γ range from 3.5 to 9.¹¹ For spherical grains the mass density in the dust cloud is given by

$$\rho_d = \frac{4}{3} \pi \rho_s \int a^3 n(a) da \quad (A-8)$$

For a particle in the Rayleigh regime (where $ka \ll 1$), the scattering and absorption cross sections are given, respectively, by

$$\sigma_s = \frac{8\pi}{3} k^4 a^6 \left(\frac{\epsilon_r - 1}{\epsilon_r + 2} \right)^2 \quad (A-9)$$

and

$$\sigma_a = 12\pi ka^3 \frac{\epsilon_r \tan \delta}{(\epsilon_r + 2)^2} \quad (A-10)$$

when $\tan^2 \delta \ll 1$.

When $ka \ll 1$, $\sigma_a \gg \sigma_s$ and extinction is essentially all due to absorption. The ratio of wavelength to radius for which $\sigma_a = \sigma_s$ is

$$\frac{\lambda}{a} = 2\pi \left[\frac{2(\epsilon_r - 1)^2}{9 \epsilon_r \tan \delta} \right]^{1/3} \quad (A-11)$$

For our typical soil values--say, $\epsilon_r = 5$ and $\tan \delta = 0.03$ -- $\lambda/a = 18$. This value is only about one-third that where the Rayleigh and optical-scattering asymptotes intersect (Figure A-4). We therefore conclude that scattering loss is negligible for the relevant materials here in the range where the Rayleigh approximation is valid.

Absorption by grains in the Rayleigh region was considered in the preceding section. Because

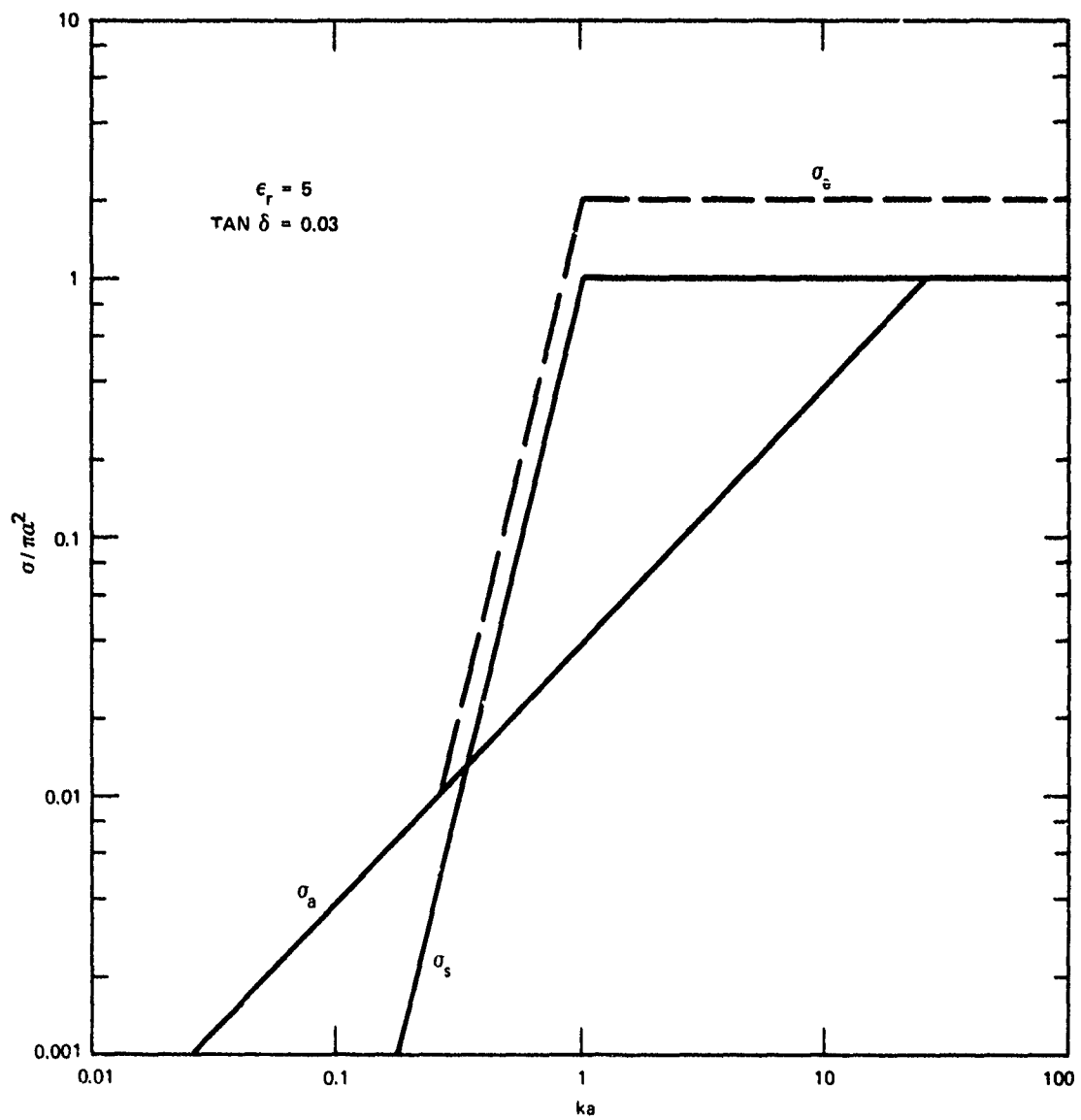


FIGURE A-4 INTERSECTIONS OF OPTICAL AND RAYLEIGH ABSORPTION AND SCATTERING ASYMPTOTES

$$\alpha = 1/2 \sigma_a^{(t)} = 1/2 \int \sigma_a n(a) da = \frac{6\pi k \epsilon_r \tan \delta}{(\epsilon_r + 2)^2} \int a^3 n(a) da \quad (A-12)^*$$

and, from Eq. (A-8),

$$\int a^3 n(a) da = \frac{3}{4\pi} \frac{\rho_d}{\rho_s}, \quad (A-13)$$

Eq. (A-2a) follows. Not surprisingly, the same expression for absorption can be derived using either approach.

Extinction when all of the grains are Rayleigh scatterers seems, therefore, to be well understood (semicoherent scattering--to be considered below--is probably much weaker than the incoherent process).⁴ On the other hand, the situation is very uncertain when many particles are in the optical region. Mie resonances may occur, may not occur, or may be significant, depending on the geometric regularities (e.g., perfect sphericity) of the particles and the loss tangent of the material comprising the scatterers. Also, there has been some question^{5,6} whether the extinction cross section in the optical regime is twice the geometrical cross section or equal to the geometrical cross section.

Born and Wolf⁸ assert that the extinction cross section is twice the geometrical cross section for large, totally absorbing obstacles. They also report the work of other authors that support this conclusion for perfectly reflecting, nonabsorbing, and weakly absorbing spheres. Other calculations¹⁰ provide further support for that result. The question seems to be whether or not energy diffracted in the forward direction into the region around the geometric shadow is truly "lost" from the incident wave and should be counted as extinction. In this report, we will assume that the short-wavelength extinction cross section σ_e is twice the geometric one, and, for simplicity, essentially ignore any possible Mie resonances. Our extinction model will then be the one shown in Figure A-4

*The limits of integration in Eq. (A-12) should be over all sizes, if all of the grains are Rayleigh scatterers, or, if there are large particles, up to a limit ($ka \cong 0.25$), obtained from considerations discussed below.

by the dashed line, which is twice the scattering cross section, for $ka \geq 0.25$ (σ_e was set to $2 \sigma_s$ on the Rayleigh asymptote to compensate roughly for any Mie resonances, which tend to raise σ_e in the $0.25 \leq ka \leq 1$ range). Figure A-5 shows the values of a for which $ka = 0.25$ and $ka = 1$, which turns out to be very close to the value (for $\epsilon_r = 5$) where the Rayleigh and optical asymptotes intersect, for the frequency interval relevant to the DICE THROW transmission experiment. It is clear that scattering losses could have been very important for the higher measurement frequencies at early times after detonation, when many centimeter and larger particles were probably airborne.

Bollen et al.⁶ made predictions of DICE THROW transmission experiment effects using a particle size distribution thought to have been representative of the DICE THROW site. Their particle size distribution ("distribution A") can be reasonably well approximated by a two-segment modification of Eq. (A-7):

$$n(a) = \begin{cases} K a^{-5} & a_s < a < a_o \\ K a_o^{-3/2} a^{-7/2} & a_o < a < a_b \end{cases} \quad (A-14)$$

where

$$a_s = 7 \times 10^{-6} \text{ m}$$

$$a_o = 10^{-3} \text{ m}$$

$$a_b = 0.5 \text{ m}$$

and

$$K = \frac{3}{4\pi} \frac{\rho_d}{\rho_s} \left[a_s^{-1} - 3a_o^{-1} + 2a_o^{-3/2} a_b^{1/2} \right]^{-1}$$

$$= 1.3 \times 10^{-5} \left(\frac{\rho_d}{\rho_s} \right) \text{ m}.$$

About half the mass is in particles bigger than 5 cm. Because all of the particles in the $\gamma = 5$ segment (i.e., those with $a < 0.1$ cm) are below the $ka = 0.25$ point for frequencies of interest here (cf., Figure A-5), they will make a negligible contribution to the scattering component

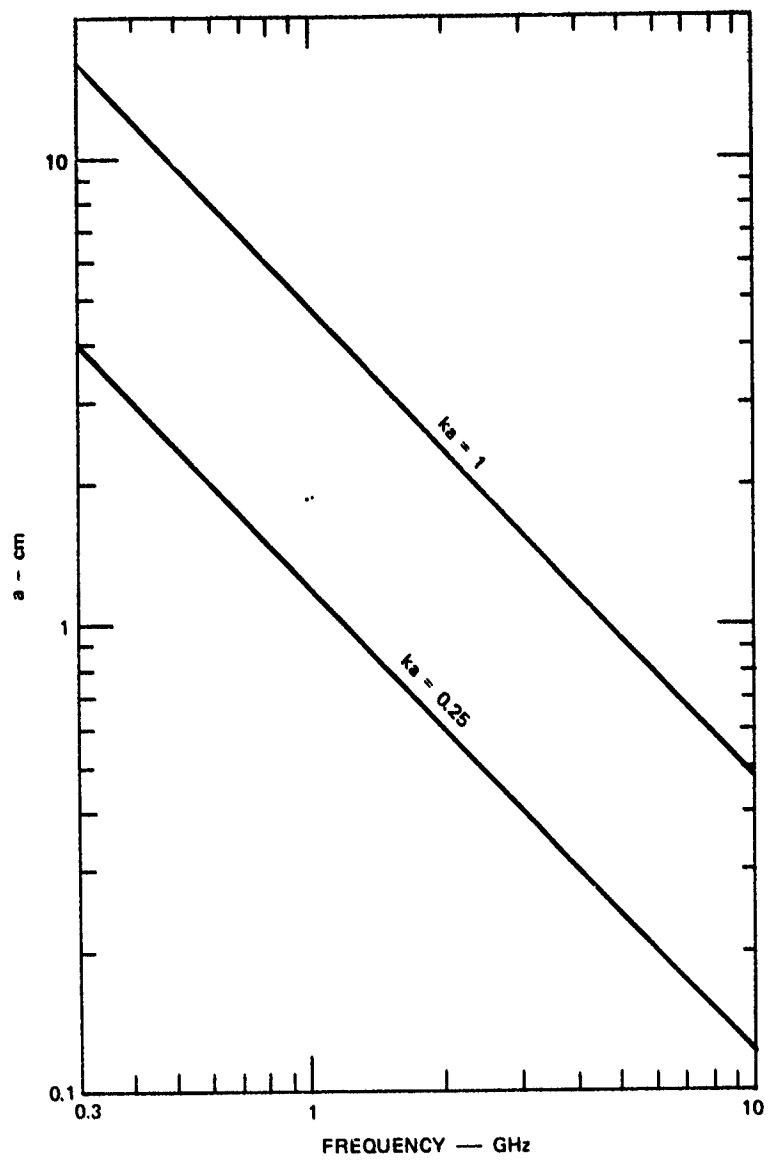


FIGURE A-5 CRITICAL RADII vs FREQUENCY

of extinction and can be ignored. Thus, only the $\gamma = 3.5$ segment needs to be considered, and the expression for attenuation equivalent to Eq. (A-12) for this extinction model is

$$\alpha = 1/2 \sigma_e^{(t)} = 1/2 \int_{(4k)^{-1}}^{a_b} \sigma_e(a) n(a) da \quad (A-15)$$

where

$$\sigma_e(a) = \begin{cases} 2\pi a^2 & a \geq k^{-1} \\ 2\pi k^4 a^6 & a < k^{-1} \end{cases}$$

$$n(a) = K a_0^{-3/2} a^{-3.5}$$

Carrying out the integration gives

$$\alpha = 1.3 (2.3 k^{1/2} - 2.8) \left(\frac{\rho_d}{\rho_s} \right) \quad (A-16)$$

As expected, the lower integration limit makes less than a 1% contribution to this expression for α ; this result further supports ignoring the $\gamma = 5$ segment. The second term in Eq. (A-16) comes from the upper integration limit, and, since it varies as $a_b^{-1/2}$, it becomes relatively less important as there are more large particles or as the frequency increases. Values for α obtained using Eq. (A-16) are comparable to those computed by Bollen et al.,⁵ where numerical integration was used with the actual particle size distribution rather than with this model.

Extremely large values of attenuation can occur when there are many large scatterers as compared to absorption by a cloud of Rayleigh regime grains. The solid lines of Figure A-6 present the attenuation computed from Eq. (A-16) at $\rho_s = 2.5 \text{ g/cm}^3$ versus ρ_s . A comparison with the absorption curves of Figure A-4 reveals that extinction losses for this model are enormously larger than absorption losses from the smaller grains. However, extinction losses are very sensitive to γ . The dashed line in Figure A-6 is the extinction computed for a model where $\gamma = 5$ from

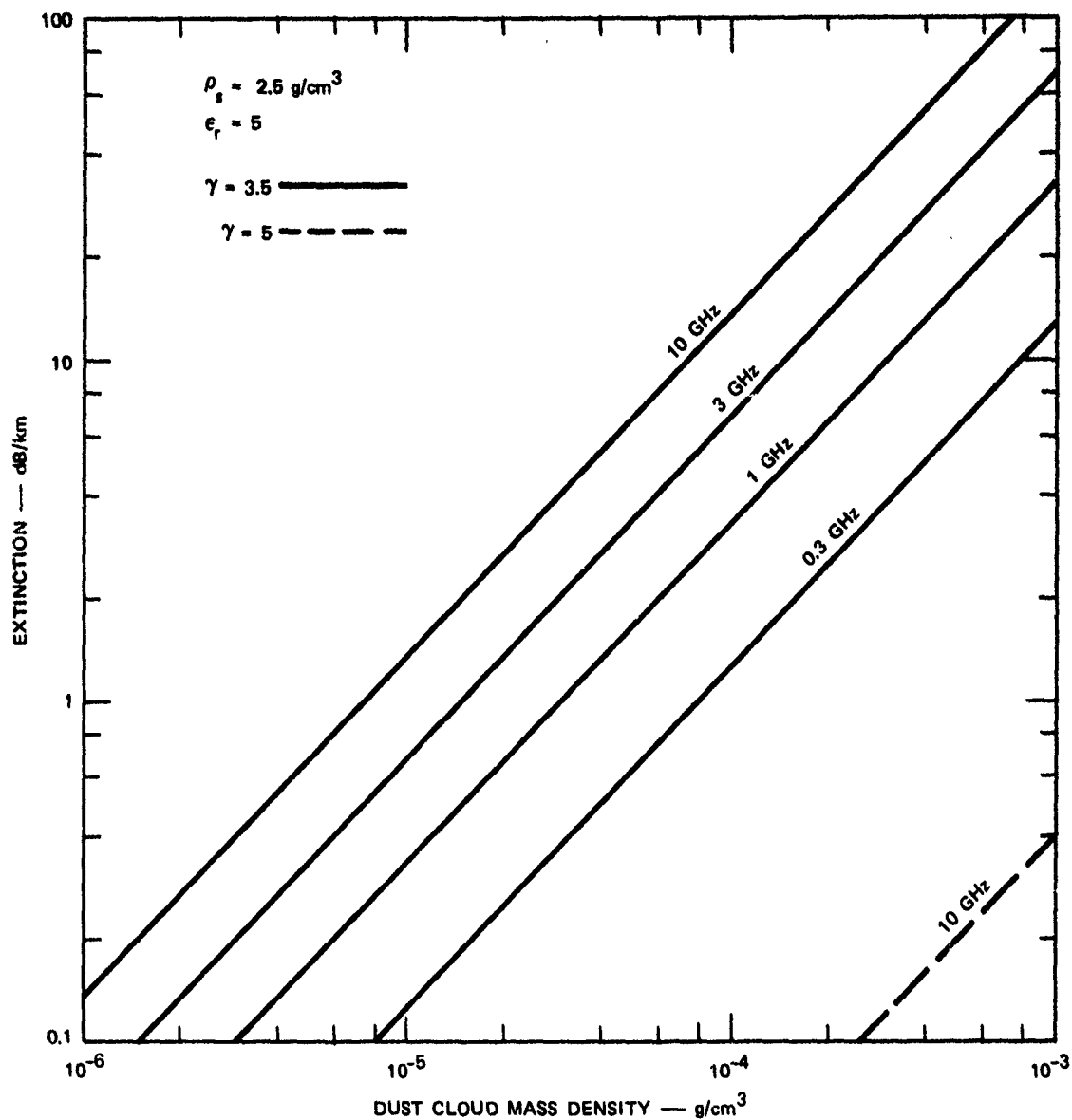


FIGURE A-6 ATTENUATION DUE TO EXTINCTION CAUSED BY LARGE SCATTERERS

$a_s = 7 \times 10^{-6}$ m to $a_b = 0.5$ m; this curve is substantially below the absorption curves. Figure A-7 shows that the ratio of scattering loss for $\gamma = 5$ to that of $\gamma = 3.5$ for these models is in the range of 10^{-5} to 10^{-2} over the frequency interval of interest here. Larger values of γ lead to even smaller values for scattering loss.

Chesnut considered the relative strengths of incoherent (σ_{incoh}) and semicoherent backscattering (σ_{coh}), and concluded that coherent scattering was substantially the weaker for dust clouds. Figures A-8 and A-9 summarize his results. The dashed curves apply for particulate clouds having only one grain size, and the solid lines apply for a continuous size distribution dominated by small particles ($\gamma \cong 6$ for $0.6 < a < 3$ mm and $\gamma \cong 9$ for $a > 3$ mm). These results were also based on $\rho_g = 2\text{g/cm}^3$, an outer scale of 100 m, and a turbulent spectrum approximating the Kolmogorov spectrum. Perhaps the most significant assumption made was that the variance of particle number was equal to its expectation, which probably greatly overestimates $\sigma_{\text{coh}}/\sigma_{\text{incoh}}$ in most circumstances. Although semicoherent scattering is relatively more important when particles are small and at low frequencies, it is very small in an absolute sense. Because a preponderance of small grains is likely to occur only at low dust cloud mass densities, semicoherent scattering is probably negligible.

4. Summary

Scattering losses are probably negligible except at early times before large particles have fallen out of the dust cloud. Absorption losses, which dominate in the Rayleigh regime, can be estimated from knowledge of the dielectric properties of the solid grains without requiring knowledge of the particle size distribution. When scattering losses are important, however, knowledge of the particle size is crucial. Semicoherent scattering due to density fluctuations is probably negligible compared to incoherent scattering for conditions likely to be present in dust clouds. Because extinction coefficients appear as exponents, it should be kept in mind that small errors in estimating those coefficients can lead to many decibels of error when losses are appreciable.

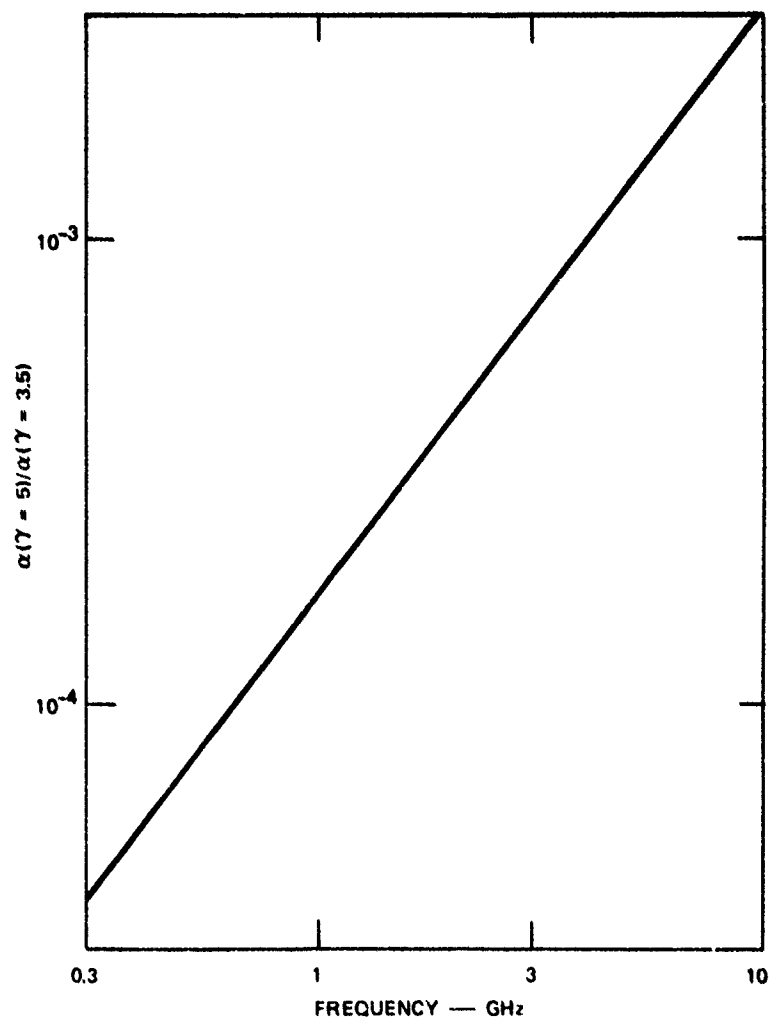


FIGURE A-7 RATIO OF SCATTERING LOSSES vs FREQUENCY

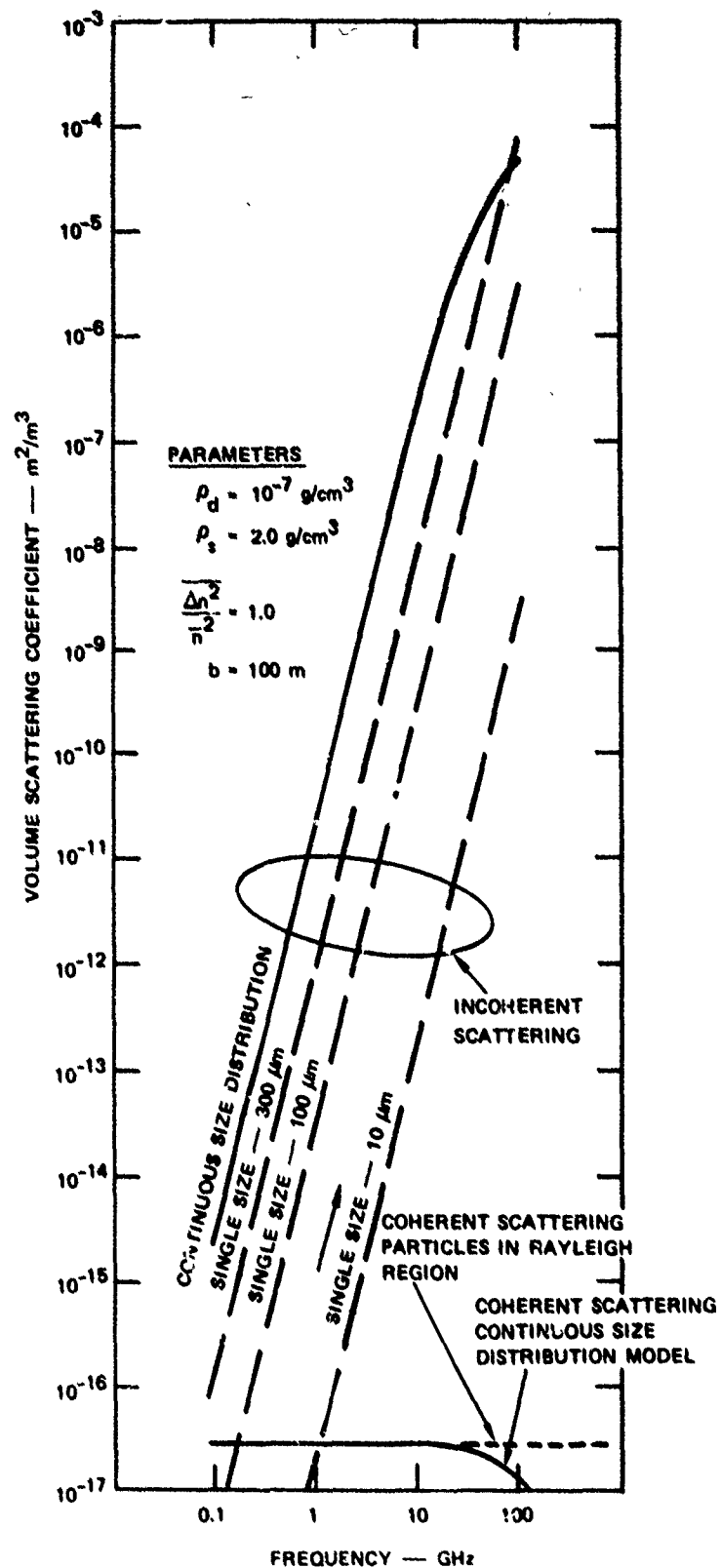


FIGURE A-8 VOLUME SCATTERING COEFFICIENT vs RADAR FREQUENCY FOR VARIOUS DUST PARTICLE SIZE DISTRIBUTIONS-- INCOHERENT AND SEMICOHERENT SCATTERING

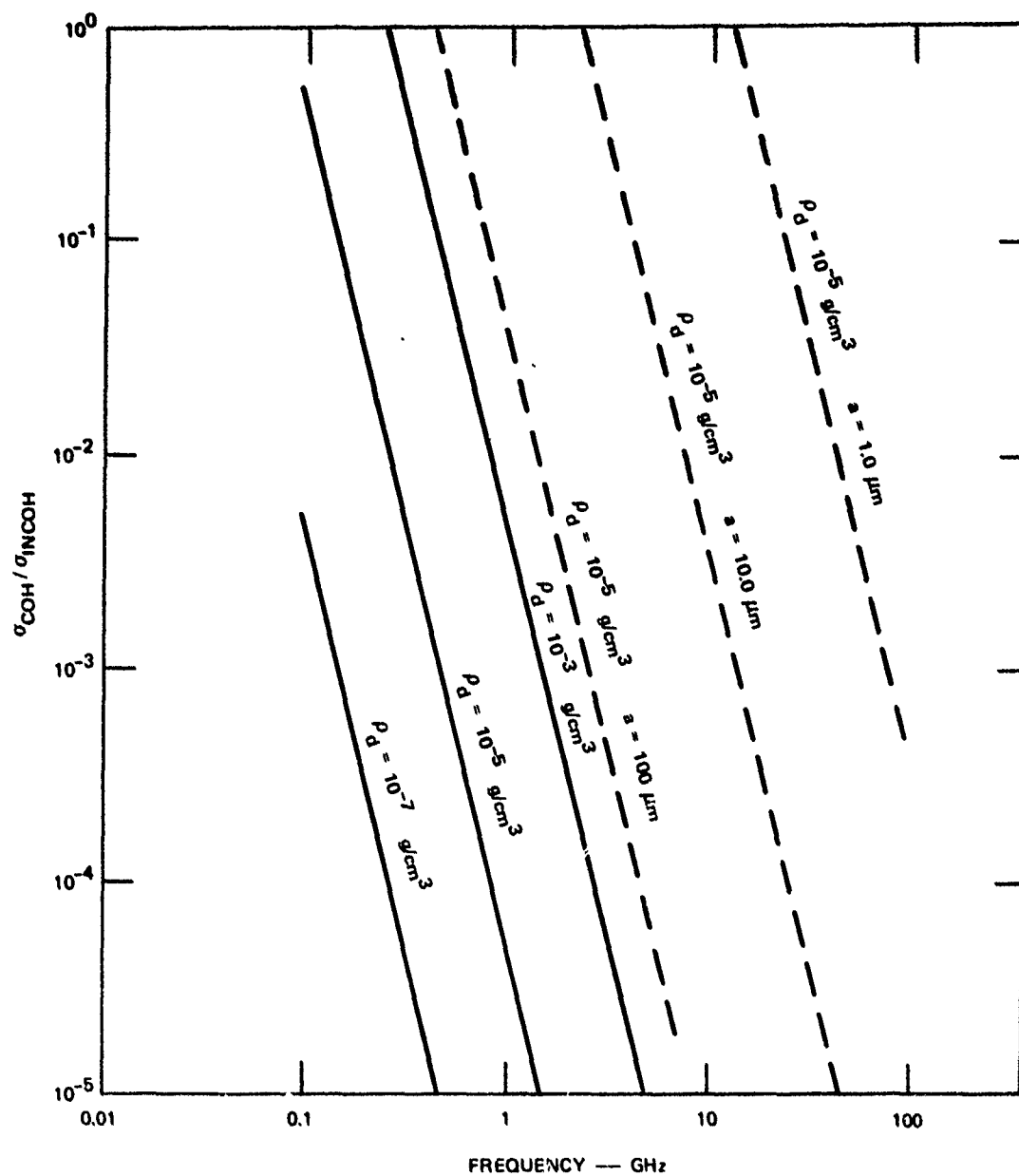


FIGURE A-9 RATIO OF COHERENT TO INCOHERENT SCATTERING vs. RADAR FREQUENCY FOR VARIOUS MODELS OF DUST PARTICLE SIZE DISTRIBUTION

Appendix B

DICE THROW CLOUD DEVELOPMENT

1. Introduction

In support of the primary rf experiment, photographic coverage of the DICE THROW event was used to document cloud morphology and position versus time for correlation with microwave measurement results. Seven 35-mm Automax framing cameras containing color positive film (Kodak type 5256 Ektachrome) were mounted at various locations along and roughly perpendicular to the signal paths. The camera locations with respect to ground zero (GZ) and the transmission experiment layout were shown in Figure 2.

Relatively slow framing rates of 1, 2, and 5 frames per second (fps) were selected. Two cameras were switched from 5 fps to 1 fps after 2 minutes in order to extend late-time coverage of cloud development. Focal lengths of lenses were varied in an effort to increase the quality of photographic documentation and allow for two different field-of-view coverages at each site (except at the main transmitter). Table B-1 lists the camera positions, parameters, and approximate event-time coverages. Cameras at the unmanned main transmitter (MT) and phase repeater (PR) sites were remotely activated at T - 1 min, whereas the others were manually controlled. All cameras were in a fixed position with line of sight to GZ, thus facilitating cloud motion measurement.

Photographic documentation of the DICE THROW event has provided a pictorial history of the event and scaled measurements of cloud morphology in direct support of data interpretation. DICE THROW morphology can be compared with actual Pre-DICE THROW II-2 (PDT II-2) morphology, as well as to the predicted ANFO behavior calculations of Pre-DICE THROW for early-, intermediate-, and late-time phenomenology, rise rates, and velocity fields. Comparisons with PDT II-2 are pertinent because PDT II-2 was used to predict the DICE THROW behavior.⁵ Other spatial data--i.e.,

Table B-1

AUTOMAX 35-mm FRAMING CAMERA PARAMETERS

No.	Location *	Range from GZ (m)	Focal Length (mm)	Field of View °V x °H	Framing Rate (per second)	Approximate Event Coverage (minutes)
1	R-1	3,963	35	30 x 38	5	4-1/2
2	R-1	3,963	85	12 x 17	5	4-1/2
3	MT	630	18	53 x 70	2	2
4	PR	2,110	35	30 x 38	2	10
5	PR	2,110	85	12 x 17	2	8
6	NOP	16,033	85	12 x 17	5, then 1	15
7	NOP	16,033	300	3.6 x 4.8	5, then 1	12

* R-1: Receiver Site 1
 MT: Main transmitter
 PR: Phase repeater
 NOP: North Oscuro Peak.

height, width, and volume versus time--as well as a general description of cloud development, aid the understanding of dust cloud evolution and eventual disposition.

2. Photographic Time Histories

Familiarity with the overall DICE THROW cloud morphology as a function of time is necessary in order to correlate microwave transmission data with specific cloud features at the points of raypath intersections. In addition, the macrophenomenology of the DICE THROW event, a 628-ton ANFO detonation, can be a useful form of comparison between HE and nuclear detonations, and among different HE charge configurations. The following description of explosive geometrics and cloud motion of DICE THROW is divided into time domains designated as early, intermediate, and late. The time coverages selected are deemed appropriate for an HE detonation produced by an explosive weight of hundreds of tons.⁵ Composites of scaled photographs exposed by cameras at Sites R-1, PR, NOP, and MT (see Figure 2) are presented together according to times after detonation. Where appropriate, photographs of HE and nuclear detonations are presented to support comparative observations.

3. Early Time-- T_0 to $T + 6$ s

Figure B-1 is a pre-detonation view of the charge at GZ looking from the phase repeater site. The ANFO charge was 11.4 m high from ground level to the top of the cylinder cap and 9.1 m in diameter. Figures B-2 through B-6 show early-time (0 to 6 seconds) view of DICE THROW from as many as four camera sites (R-1, PR, NOP, and MT). In Figure B-2(a), at $T + 0.1$ s, heated detonation products are evident through the lower two-thirds of the cloud. This material had the typical white appearance of an ANFO detonation at first [Figures B-2(b) and (c), $T + 0.2$ s] and became dome-shaped as it rose. This mound of material was most likely a consequence of shockwave reflection at the surface; that is, the upward velocity of material is greatest directly over the detonation point since initial upward velocity is proportional to the pressure of the direct

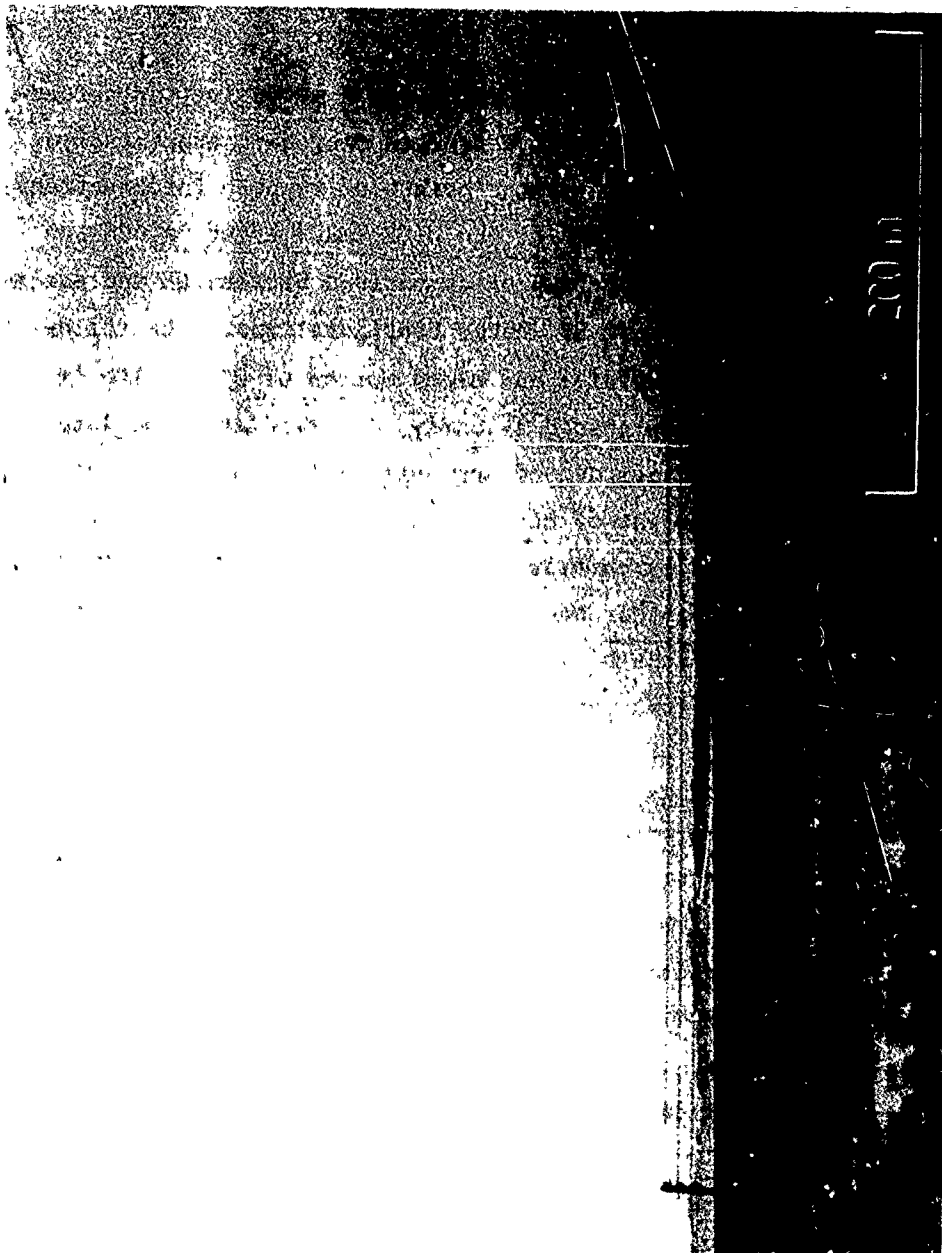
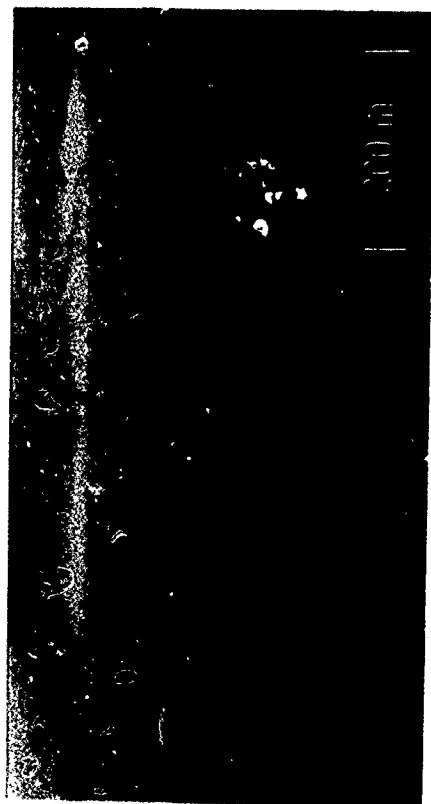
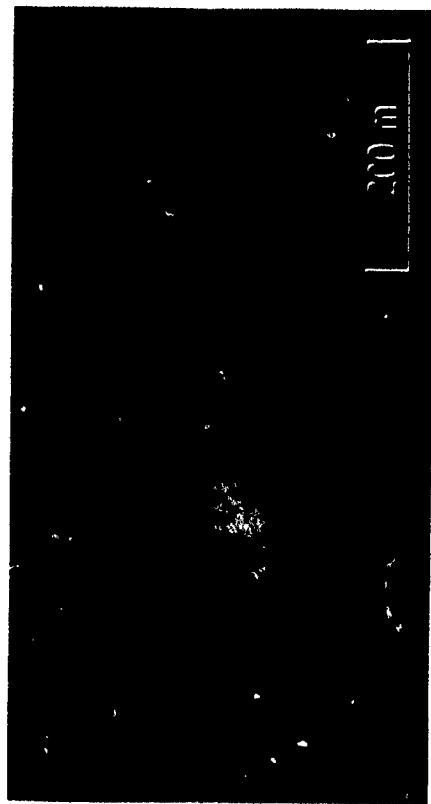


FIGURE B-1 DICE THROW CAPPED CYLINDER CHARGE OF ANFO--PRE-ZERO VIEW FROM PHASE REPEATER SITE



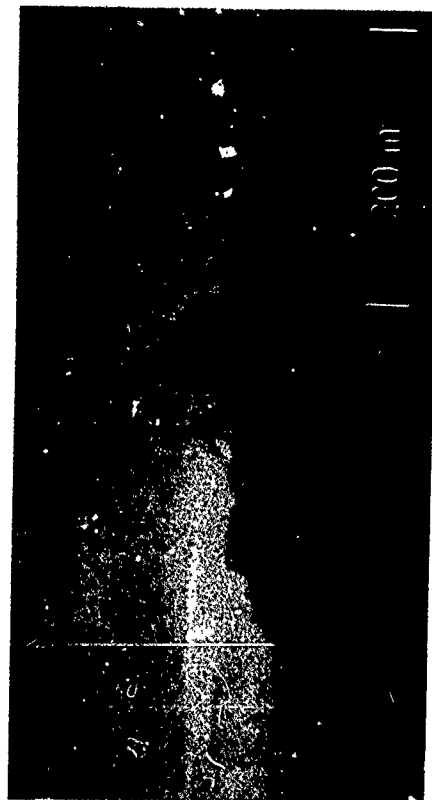
(a) R-1, $T + 0.1$ s



(c) NOP, $T + 0.2$ s



(b) PR, $T + 0.2$ s



(d) MT, $T + 0.5$ s

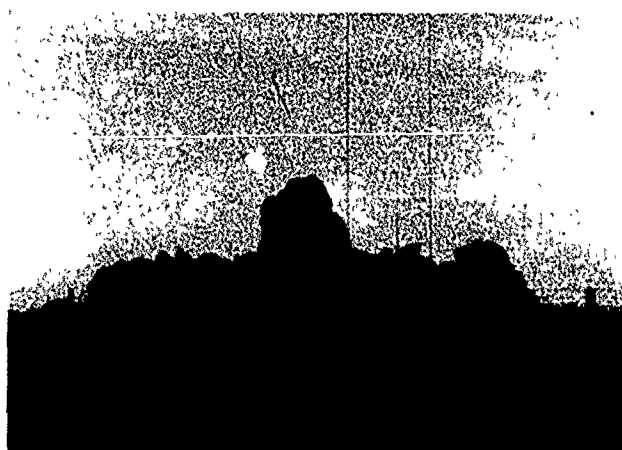
FIGURE B-2 DICE THROW EARLY TIMES $T + 0.1$ s TO $T + 0.5$ s, FROM FOUR CAMERA SITES



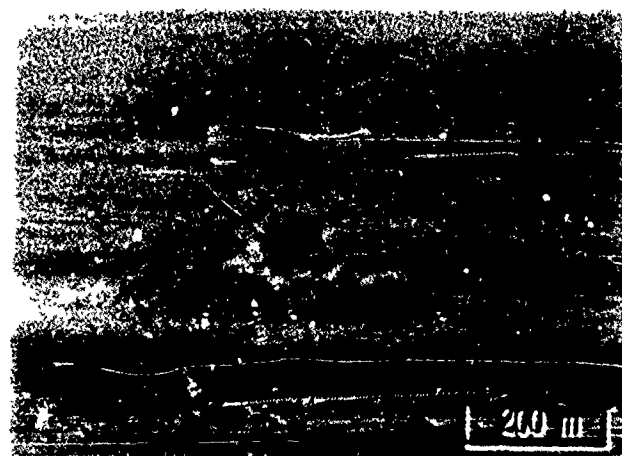
FIGURE B-3 DICE THROW WILSON CLOUD AT $T + 1$ s. VIEWED FROM PHASE REPEATER



(a) R-1

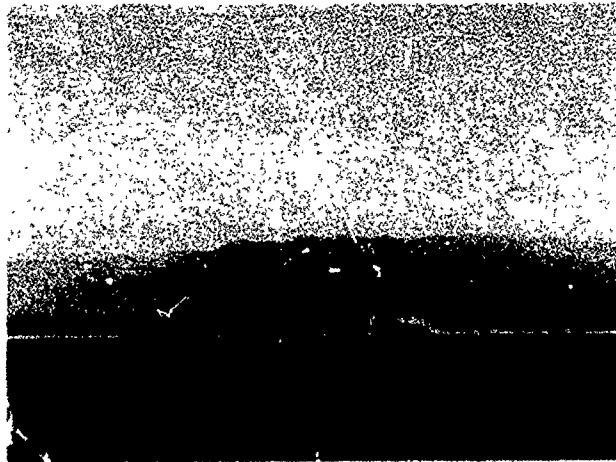


(b) PR



(c) NOP

FIGURE B-4 DICE THROW AT 2 s



(a) R-1

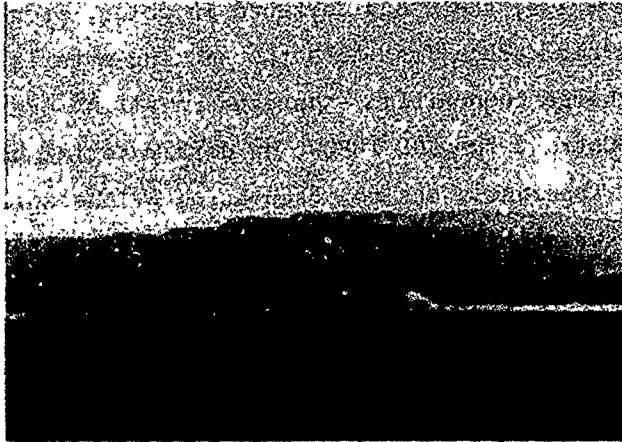


(b) PR



(c) NOP

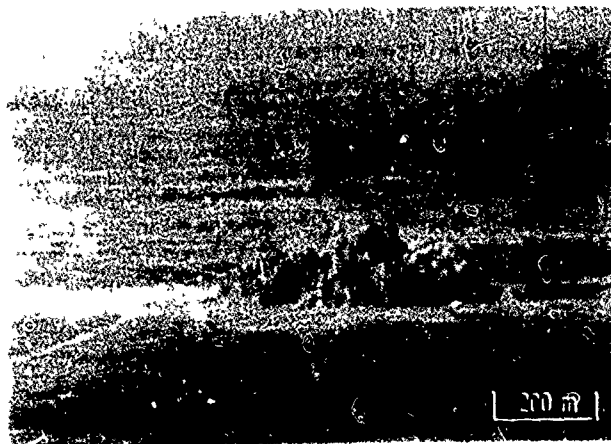
FIGURE B-5 DICE THROW AT 4 s



(a) R-1



(b) PR



(c) NOP

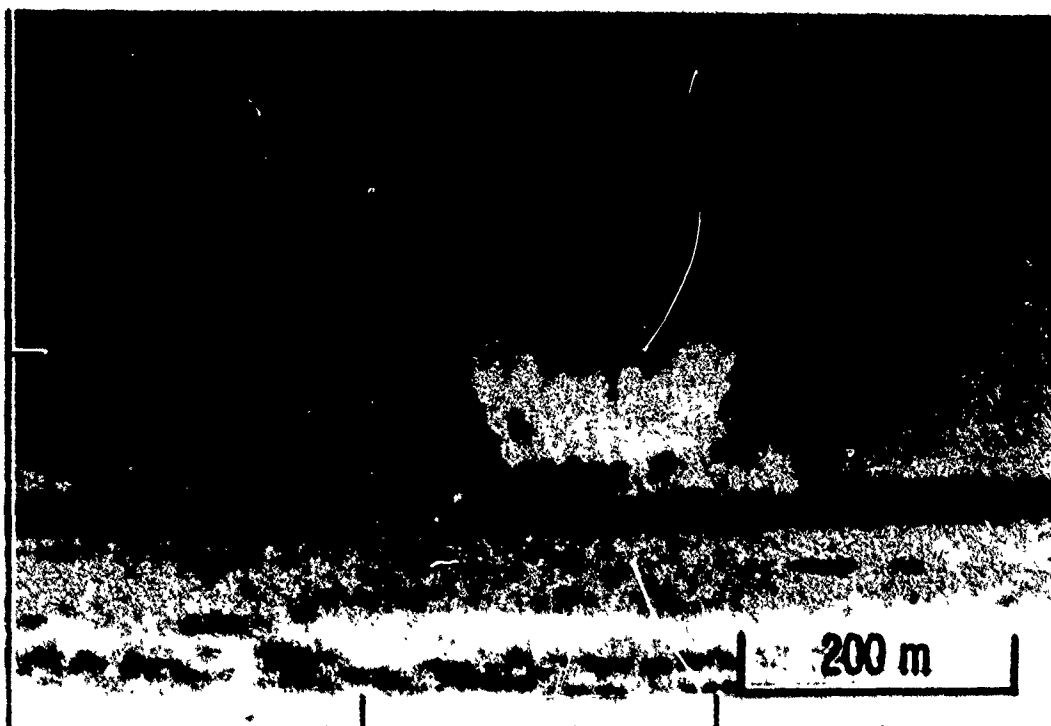
FIGURE B-6 DICE THROW AT 6 s

shockwave. By $T + 1$ s, the cloud darkened in color, presumably due to the presence of unburned carbon from both the sacking material and the non-stoichiometric charge composition (there was a slight overabundance of fuel oil). In contrast to DICE THROW, no dark material was observed during PDT II-2, apparently due to obscuration by the spires of heavy ejecta and base surge [Figure B-7(a)]; however, such material was evident in the Canadian hemispherical 100-ton ANFO detonation in 1969 [Figure B-7(b)].³ A small Wilson (condensation) cloud lasted from $T + 0.5$ s to $T + 1.2$ s (Figure B-3).

An overhead view* (Figure B-8) at $T + 0.8$ s (with the apparent crater rim outline approximately drawn to scale) reveals some interesting features. Dust billows radiating out from the cloud center like wheel spokes are aligned along existing dirt roads near GZ. Vehicle traffic churned the dirt along these roads and the dirt was looser to greater depths than the soil on surrounding surfaces. This dust was more readily lofted than that from other, less disturbed areas.

The early-time morphology of DICE THROW also differed from that of PDT II-2 in another respect. In PDT II-2, large, water-saturated clay "missiles" were radially ejected or thrown out from the center at high angles, forming very noticeable spires. This effect was not characteristic of DICE THROW, apparently because the water table at the DICE THROW Main Event site was at least 25 m deep, compared to only 2-3 m at the PDT site. However, the conditions near the surface appeared similar for both events. Therefore, as in PDT II-2 (Figure B-9), noncohesive ejecta from the surface surged up in rounded billows (but at lower angles than in PDT II-2), moving outward with slight expansion (Figures B-4 and B-5).

* Overhead 16-mm film made by the Williamson Aircraft Company and provided by Field Command, DNA.



(a) 120-T ANFO, PRE-DICE THROW II-Z A1 1 s



(b) 100-T ANFO, CANDIAN 1989 AT 1 s

FIGURE B-7 EARLY-TIME PHOTOS FROM TWO OTHER ANFO EVENTS

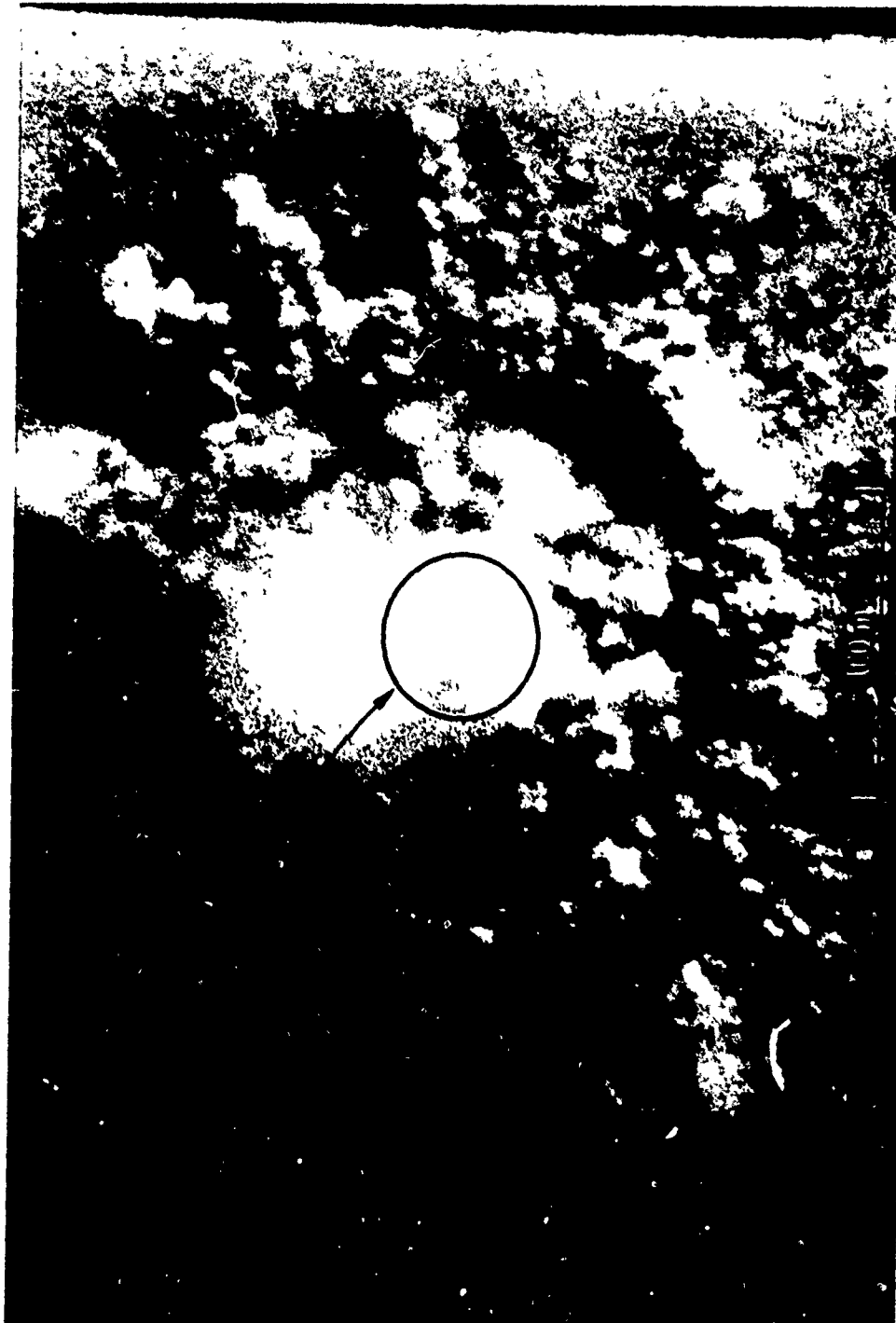
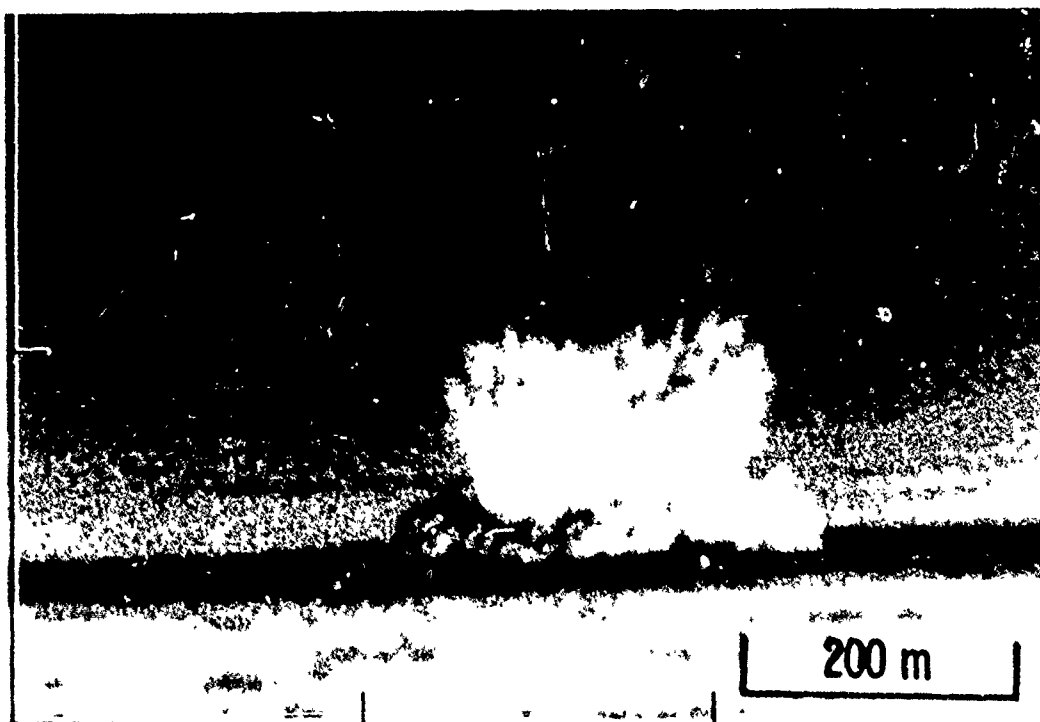
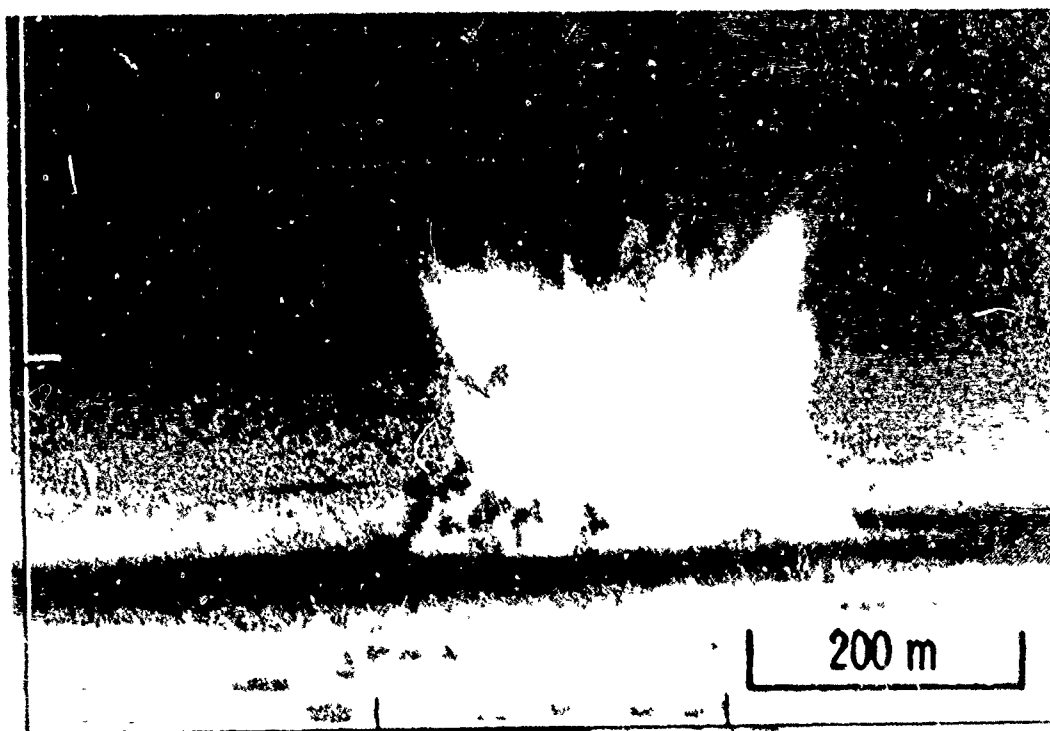


FIGURE B-8 OVERHEAD VIEW OF DICE THROW CLOUD AT $T + 0.8 \text{ s}$



(a) $T + 2 \text{ s}$



(b) $T + 4 \text{ s}$

FIGURE B-9 120-T ANFO, PRE-DIC: THROW II-2

Similar to nuclear "base surge," this "dirt surge" was caused by gust-lofted debris and some missiles (rock chunks) falling back onto the surface. After the rock chunks and heavier dirt clods rapidly fell out, these ejecta probably comprised most of the late-time dust cloud material. By $T + 6$ s (Figure B-6), this ejected surge reached an altitude of only 100 to 150 m, much less than the 300 m that the PDT II-2 spires had attained by 5 s.⁵

The center protuberance, presumably composed principally of detonation products, reached an almost stationary height by about $T + 6$ s, although measurements from two views (R-1 and PR) give evidence of a 5-to-7-m oscillation during the time span $T + 4$ s to 8 s. This is consistent with the velocity field calculations provided by AFWL, which now utilize a newly developed "special rezone technique"* of the HULL code. Figure B-10 displays the HULL velocity field calculation for DICE THROW[†] at $T + 5$ s superimposed to scale on the R-1 view of DICE THROW. This computation predicts a downdraft in the center of the cloud that is part of a "reverse" vortex in the cloud. Thus, the initial upward movement of the cloud center is rapidly stopped; moreover, according to the calculation, a normal vortex is beginning to form outside the dust-laden region.

4. Cratering

A study of crater geometry is necessary in order to determine the approximate mass of lofted dust and debris. The apparent crater formed by DICE THROW was about 54 m in diameter and 8 m deep.[‡] Figures B-4(b) and B-8 show the scaled crater outline overlayed on photographs taken from the PR site and from above GZ, respectively.

* Descriptions of this technique were published in Appendix C of Bollen et al.,⁵ in the form of a memorandum authored by Dr. Charles Needham of AFWL and in the Proceedings of the DICE THROW Symposium as well.

† The HULL code calculations for DICE THROW presented in this report were kindly provided by Major G. P. Ganong of AFWL.

‡ Cratering data, which were originally supplied to us by Field Command, DNA, have been published in the Proceedings of the DICE THROW Symposium.¹

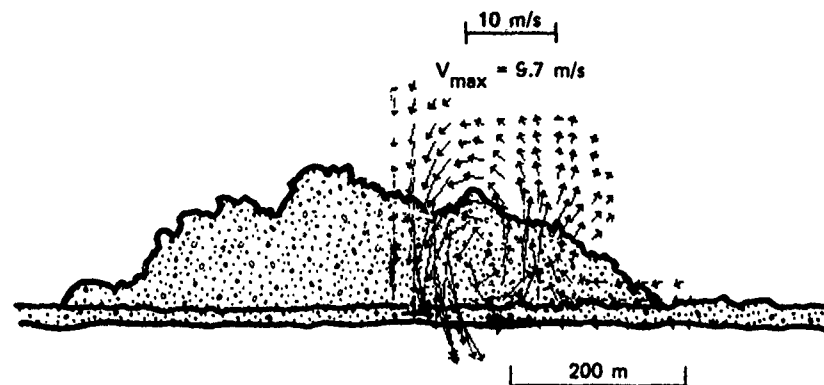


FIGURE B-10 DICE THROW CLOUD COMPARED TO HULL VELOCITY FIELD CALCULATION AT 5 s

As discussed earlier, water table conditions for the DICE THROW event probably prevented the ejection of as much dense material into the air as occurred in PDT II-2. In addition, the local geologic setting was deliberately modified in order to reduce the number of large particles or "missiles" for DICE THROW, in the hope of reducing ejecta-caused damage to the equipment used in the experiments. Since the ejected dirt in DICE THROW was rather noncohesive gypsum sand, one would expect a smaller crater in DICE THROW than in PDT II-2. This should then result in a lower cratering efficiency, measured by the cubic feet of material permanently displaced from the crater region per ton of TNT yield.

In order to determine the maximum amount of crater ejecta lofted into the air, it is necessary to estimate the amount of soil missing from the crater. This is done by calculating the volume of the apparent crater and reducing it by the volume of the dirt forming the lip. The crater and lip profiles were measured shortly after the test. Figure B-11 shows the cumulative volume as a function of the distance from the crater center, numerically integrated from the measured profile.

From the data presented in Figure B-11, it appears that the "missing" volume of crater ejecta asymptotically approaches 1560 m^3 . This volume is significantly less than the cratering volume of 4250 m^3 predicted for DICE THROW; that prediction was based on an estimate of 8.5 m^3 of ejecta per ton of TNT and on the 500-ton TNT equivalence for the DICE THROW event.

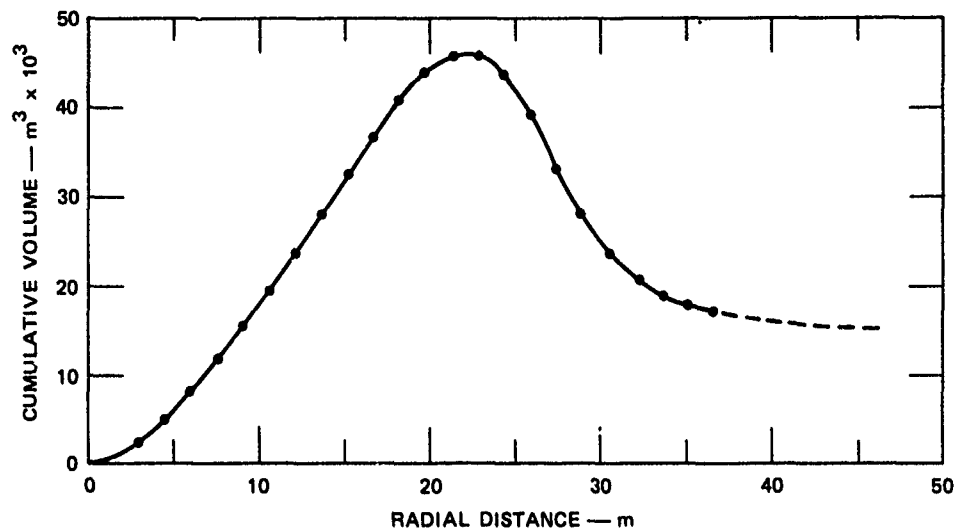


FIGURE B-11 CUMULATIVE CRATER VOLUME vs DISTANCE AWAY FROM CRATER CENTER

For an average soil density of approximately 2 g/cm^3 , the maximum total mass of DICE THROW ejecta lofted an appreciable distance into the air is estimated to be 3.4 kt. This value is about half of our predicted value of 8 to 9 kt. Much of the discrepancy may result from reducing the apparent crater volume by the volume of material in the lip. Although the lip material may have been part of the "cloud" at early times, the smaller value is better at late times because it more fairly represents the amount of soil carried away in the cloud. The value chosen for the mass aloft should be determined by the time segment being studied.

5. Intermediate Time-- $T + 6 \text{ s}$ to $T + 15 \text{ s}$

In this epoch, the darker protuberance in the center, produced by the material used in the detonation, disappears from view as the surrounding dust cloud rises above it (Figures B-12 and B-13). This behavior is consistent with the predicted downdraft in the center of the cloud (see Figure B-10). Photographs taken from the aircraft at 6 and 15 s [Figures B-14(a) and (b)] are also consistent with an initial center downdraft, exterior vortex, and low velocities. The HULL velocity field calculation at 10 s, shown superimposed on the cloud outline in Figure B-15, shows only the normal vortex direction--the close-in reverse vortex has



(c) NOP



(d) MT

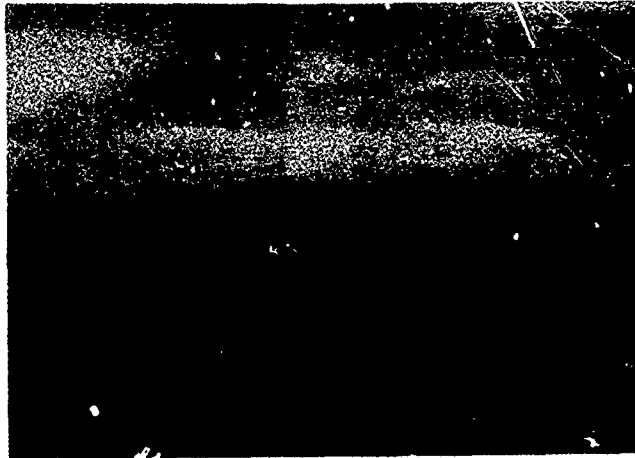


(a) R-1



(b) PR

FIGURE B-12 DICE THROW AT 8 s



(a) R-1

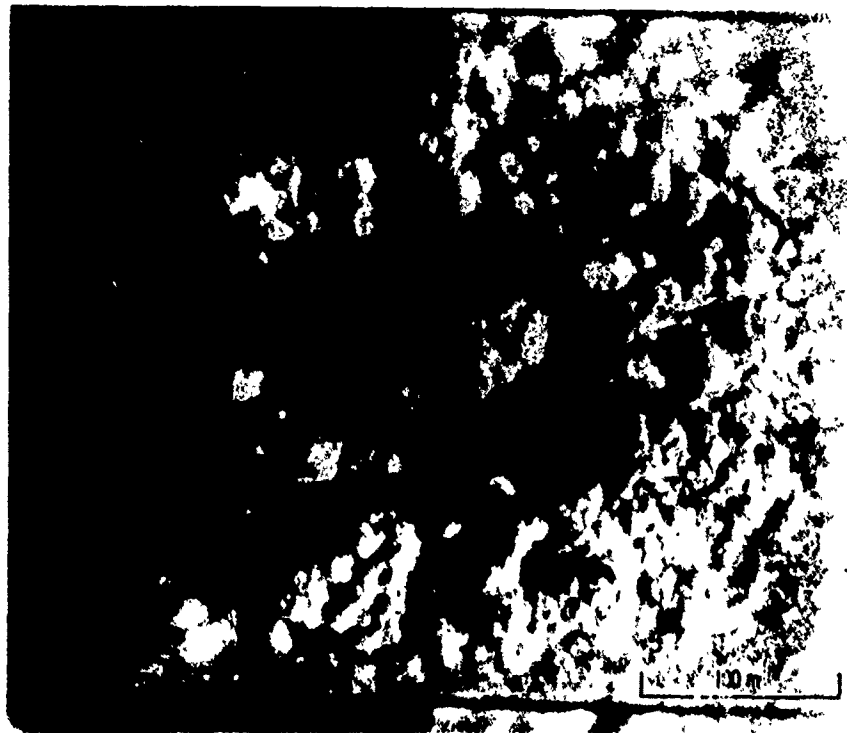


(b) PR

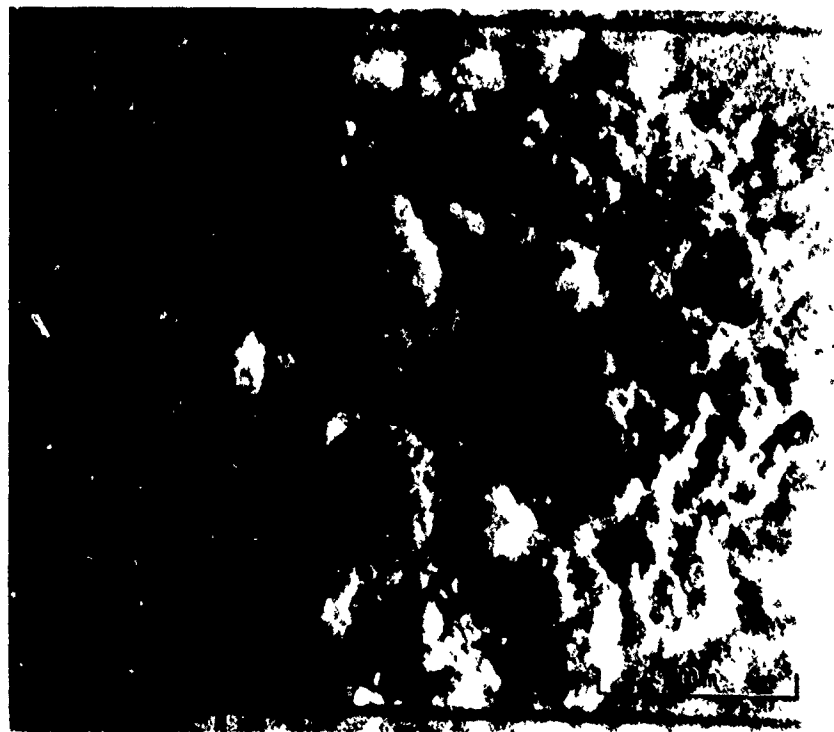


(c) NOP

FIGURE B-13 DICE THROW AT 10 s



(a) $T + 6 \text{ s}$



(b) $T + 15 \text{ s}$

FIGURE B-14 OVERHEAD VIEWS OF DICE THROW CLOUD

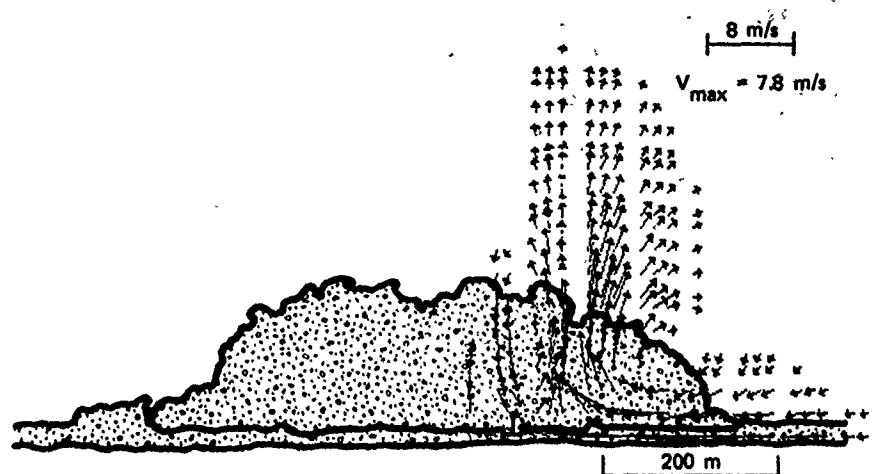


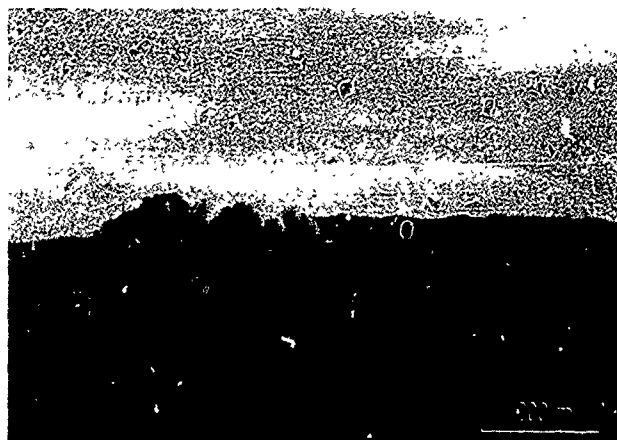
FIGURE B-15 DICE THROW CLOUD COMPARED TO HULL VELOCITY FIELD CALCULATION AT 10 s

dissipated. But this comparison suggests that no material was injected into the region where the normal vortex formation was predicted. The general appearance of the cloud resembles a "doughnut" with a "hollow" in the center by 15 s [Figure B-14(b)].

By about $T + 10$ s, it is readily evident that the cloud had begun to move appreciably to the northwest or away from the phase repeater, to the left of R-1, and to the right of the line of sight from North Oscuro Peak. Before $T + 15$ s, the residual dust cloud maintained an overall shape similar to that at early times except for the absence of the upward-protruding structure of detonation material. During this time sequence the main part of the cloud steadily rose and expanded around the dome of detonation products in the center. At about $T + 15$ s, particularly as viewed from the R-1 and NOP sites, a pedestal-like "stem" started to form as the lower part of the cloud above the ground dust layer became "pinched-off" [Figure B-16(a) and (c)].

6. Late Time--After $T + 15$ s

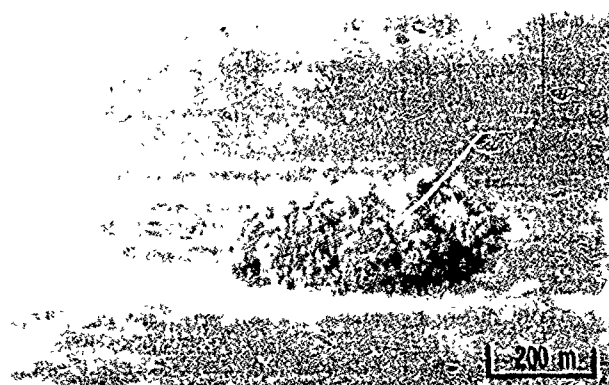
If it had behaved in a way similar to a nuclear or tangent-sphere HE detonation after $T + 15$ s, the DICE THROW cloud should have been affected by cool air rushing in under the rising vortex ring and bringing



(a) R-1



(b) PR



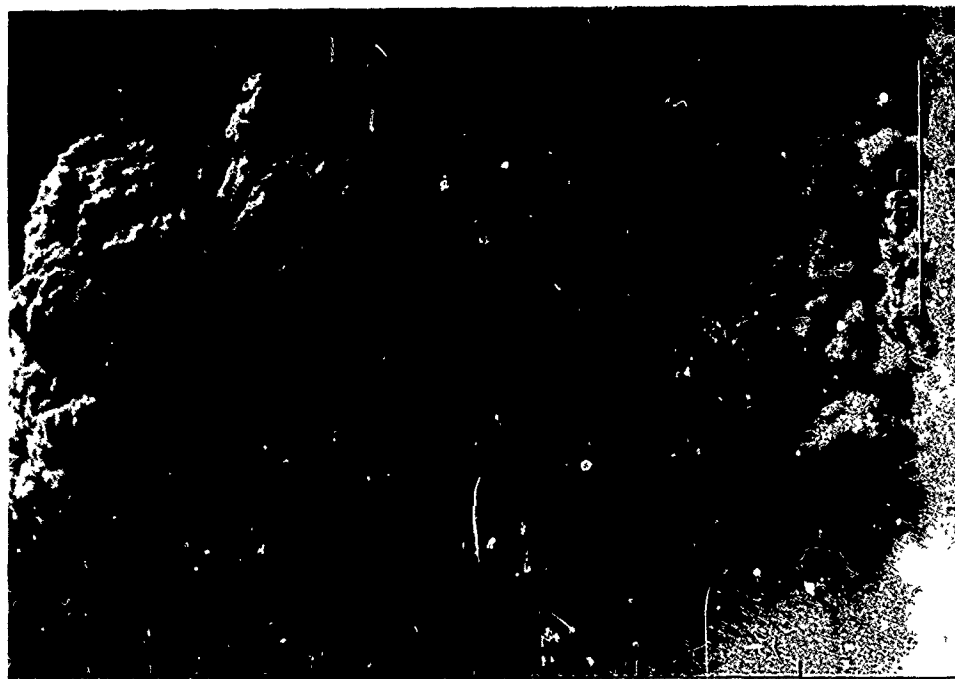
(c) NOP

FIGURE B-16 DICE THROW AT 15 s

in residual dust or "sweep-up" material. (Figures B-17, B-18, and B-19 show such characteristics for nuclear and tangent-sphere TNT detonations after $T + 15$ s.) However, according to HULL calculations, which the photographic data support, the DICE THROW vortex was outside the center of the dust cloud and was quite weak. Figure B-20 shows both the HULL linear-scale (superimposed on the cloud outline) and the log-scale velocity field calculations at $T + 20$ s. The maximum predicted velocity, which was 5.6 m/s, steadily decreased with time after detonation. The log-scale velocity field illustrates the extent of the circular motion of the computed vortex. In addition, there was no longer a predicted downdraft at the center of the cloud.

A stem eventually developed (Figures B-21 and B-22) that was bulky, compared to tangent-sphere HE and nuclear detonations. By $T + 45$ s, a very evident updraft began to influence the lofting of sweep-up and crater ejecta material up the "stem" (Figure B-23). In a nuclear cloud case, the dust traveling up the stem becomes entrained in the rising vortex ring forming the traditional "mushroom" cap; however, for DICE THROW, the dust, which appeared to move according to AFWL calculations, did not seem to become entrained in a vortex. Figure B-24 compares velocity field calculations with the DICE THROW cloud at $T + 30$ s and $T + 45$ s. The maximum (updraft) velocity slowly increased, sweeping the dust up, but the predicted weak vortex ring remained outside of the visible cloud. We believe that entrainment of dust in the vortex did not occur. Rather, the late-time morphology for DICE THROW is best described as being an amorphous and slowly rising stem, composed of several convective cells displaying their own circulation patterns, rather than a rapidly rising vortex ring with dust entrainment.

PDT II-2 did not exhibit such classical "mushroom shape" properties as strong sweep-up winds, stem, or vortex ring either (Figure B-25). Therefore, because of its same type and shape of charge, DICE THROW was not expected to develop such features. It was anticipated that DICE THROW would possess cloud morphology similar to that from buried (as deep as 17 ft) nuclear detonations--e.g., Buster Jangle: Uncle (Figure B-26).⁵ On the contrary, DICE THROW appeared less amorphous than PDT II-2 and

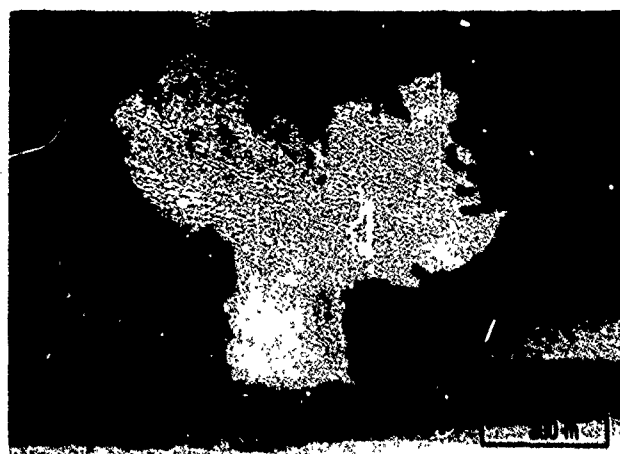


(a) 0.5-kt NUCLEAR AT -2 ft
JOHNNY BOY, 1962



(b) 1.2-kt NUCLEAR AT +4 ft
BUSTER JANGLE: SUGAR, 1951

FIGURE B-17 NUCLEAR DETONATIONS AT T + 20 s



(a) $T + 20 \text{ s}$



(b) $T + 30 \text{ s}$



(c) $T + 40 \text{ s}$

FIGURE B-18 100-T TNT, PRE-DICE THROW II-1



(a) T + 15 s

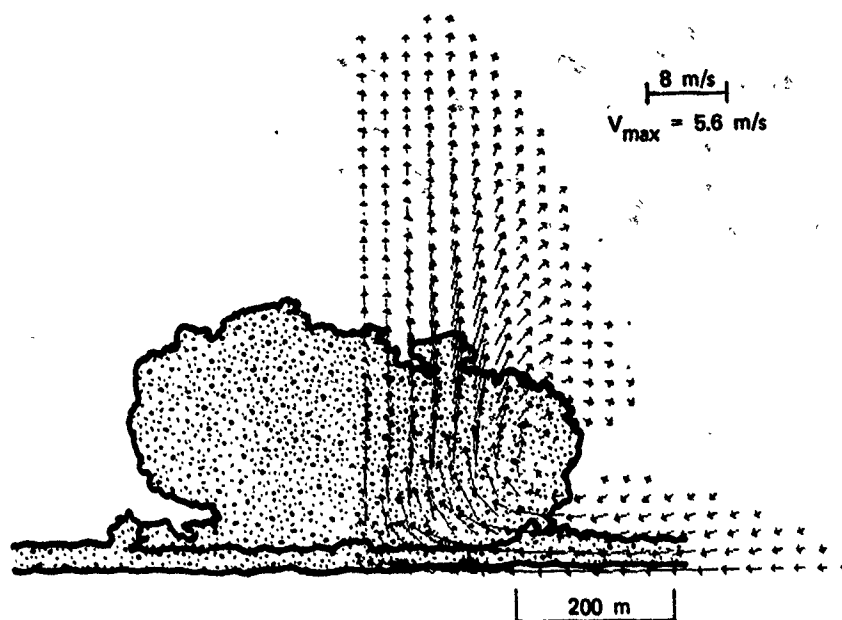


(b) T + 20 s

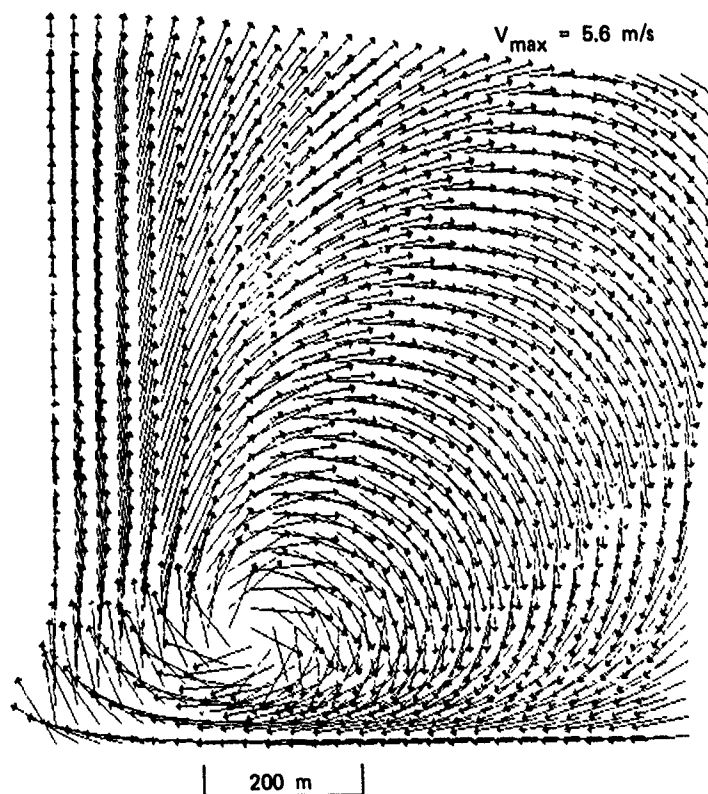


(c) T + 25 s

FIGURE B-19 500-T TNT (Tangent Sphere),
MIXED COMPANY III

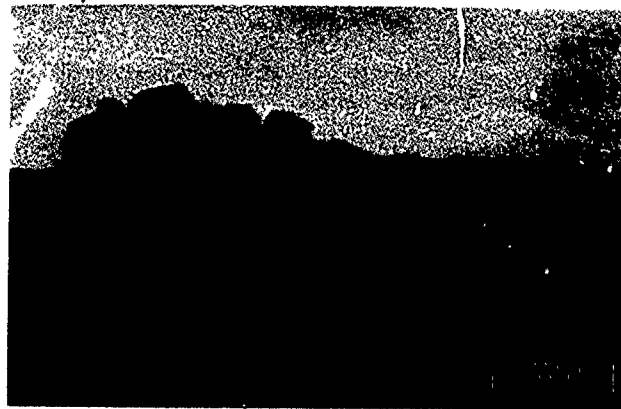


(a) LINEAR SCALE



(b) LOG SCALE

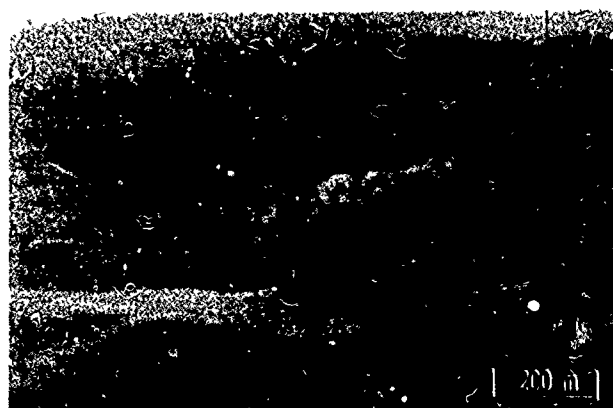
FIGURE B-20 DICE THROW CLOUD COMPARED TO HULL VELOCITY FIELD CALCULATIONS AT 20 s



(a) R-1



(b) PR



(c) NOP

FIGURE B-21 DICE THROW AT 20 s



(a) R-1



(b) PR

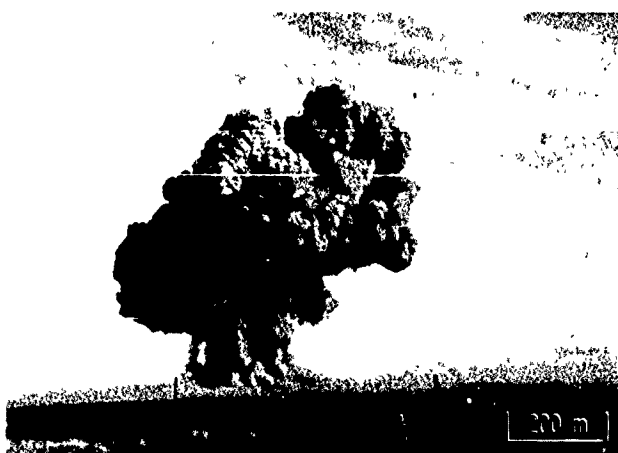


(c) NOP

FIGURE B-22 DICE THROW AT 30 s



(a) R-1

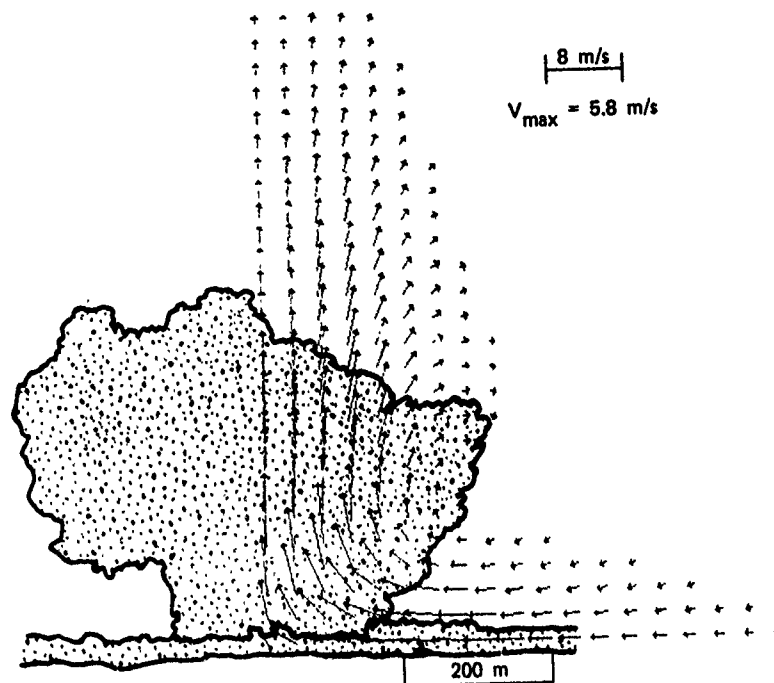


(b) PR

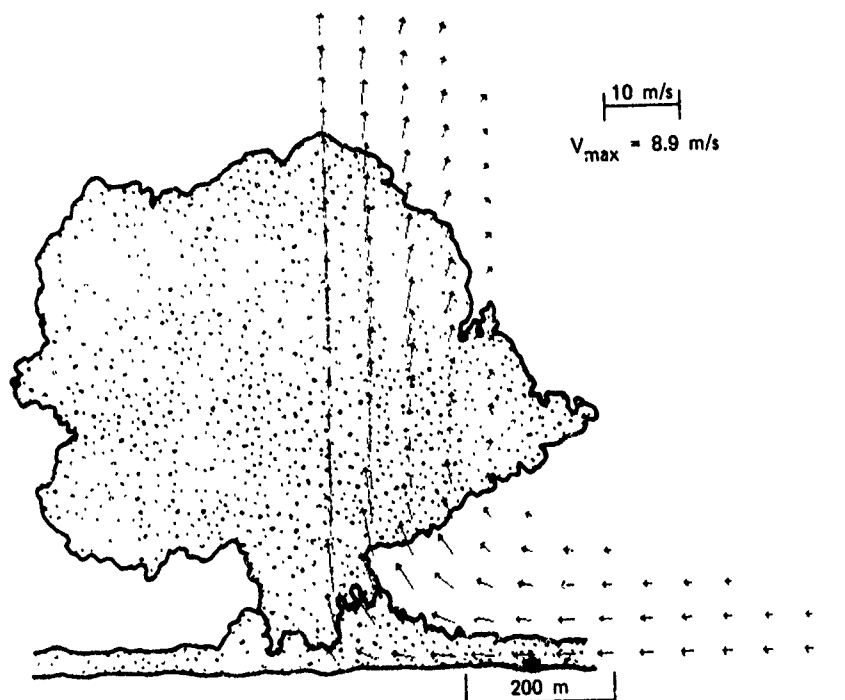


(c) NOP

FIGURE B-23 DICE THROW AT 45 s



(a) $T + 30$ s



(b) $T + 45$ s

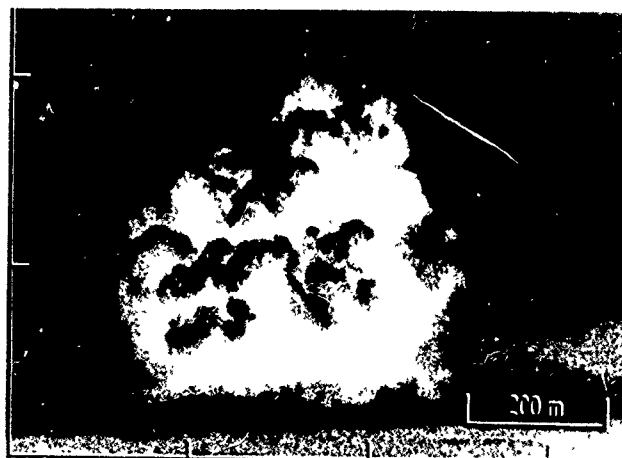
FIGURE B-24 DICE THROW CLOUD COMPARED TO HULL VELOCITY FIELD CALCULATIONS



(a) T + 20 s



(b) T + 30 s



(c) T + 40 s

FIGURE B-25 120-T ANFO, PRE-DICE THROW II-2

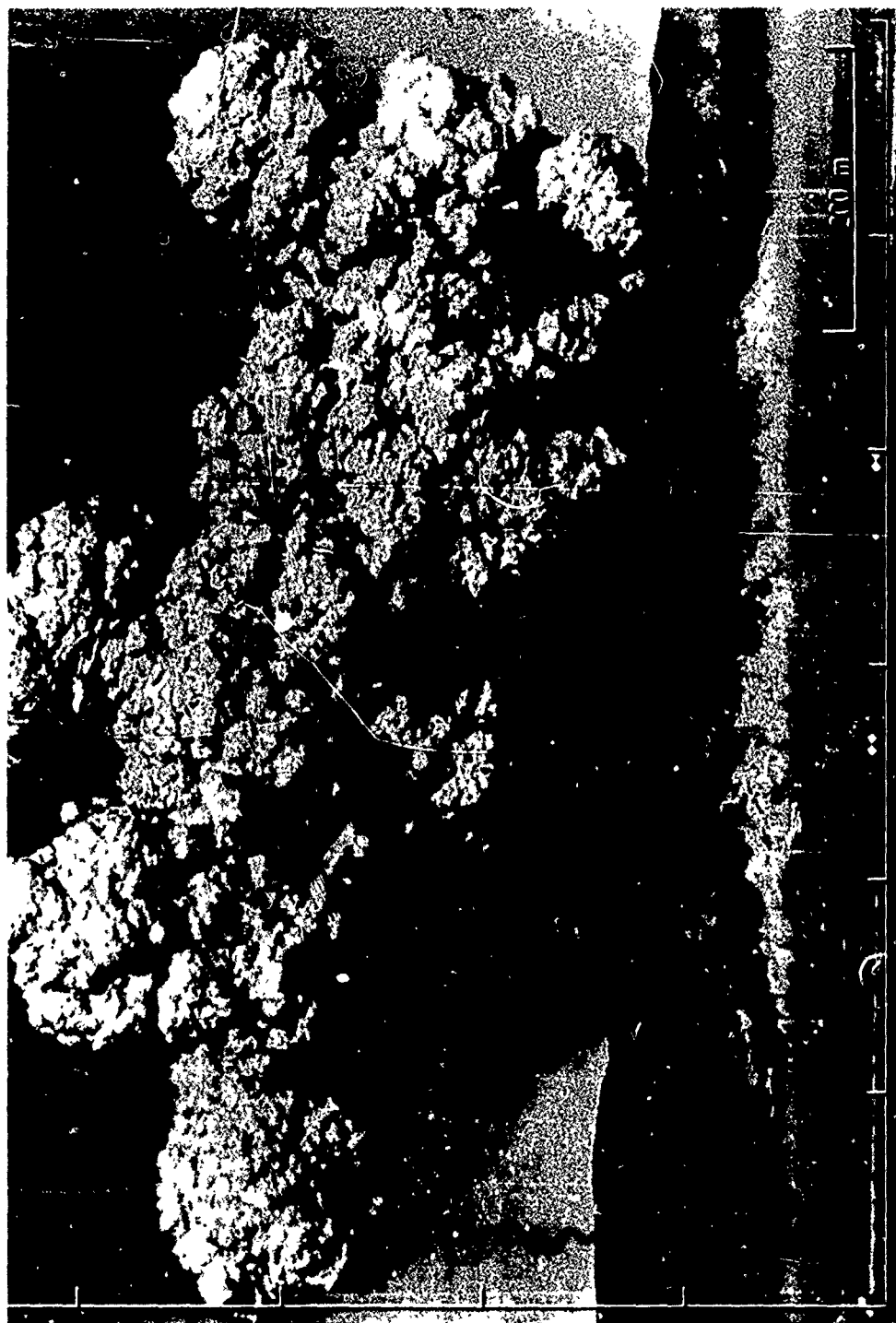


FIGURE B-26 1.2-kt NUCLEAR AT -17 ft, BUSTER JANGLE: UNCLE 1951, T + 20 s

seemed to exhibit some mushroom cloud and stem-type features. To a more-than-anticipated degree, it did resemble surface or shallow subsurface nuclear detonations such as Johnny Boy or Buster Jangle: Sugar, and, since a stem formed, it had more similarity to TNT tangent sphere detonations such as PDT II-1 (Figure B-18) and Mixed Company III (Figure B-19) at times after $T + 20$ s than expected. However, the most notable difference between PDT II-2 and DICE THROW was the lack of heavy ejecta spires in the latter.

A strong wind shear rapidly deformed the DICE THROW cloud. The lower parts of the cloud moved to the northwest, but as the cloud top rose, it was swept around to the southeast. This distortion is readily apparent in the photographs for $T + 1$ m and $T + 1$ m 30 s (Figure B-27), and makes it difficult at late times to compare the AFWL flow fields with the actual cloud shape.*

Figure B-28 compares the cloud at one minute to the AFWL velocity field calculation. The predicted vortex remains outside of the visible cloud and is still very weak. Although the predicted updraft velocity in the cloud center has increased to 9.5 m/s, it is nevertheless substantially lower than that associated with tangent sphere HE detonations. Consistent with the predicted weak vortex velocities, the material lofted appeared to remain as a stem.

As seen from the PR site [Figure B-29(b)], the main cloud began to break away from its stem at around $T + 2$ m. This separation was well developed by $T + 4$ m, by which time dissipation of both the cloud and stem has set in (Figure B-30). From personal observations, after $T + 4$ min, the main part of the cloud eventually moved to the southeast, rising and gradually dispersing up and over the South Oscuro ridge. The

*Ganong et al.,¹¹ were quite successful, however, in reproducing the appearance of the DICE THROW cloud at late times by modifying tracer particle positions in their HULL calculations according to the wind profile.



(a) R-1



(b) PR



(c) NOP

FIGURE B-27 DICE THROW AT $T + 1$ min

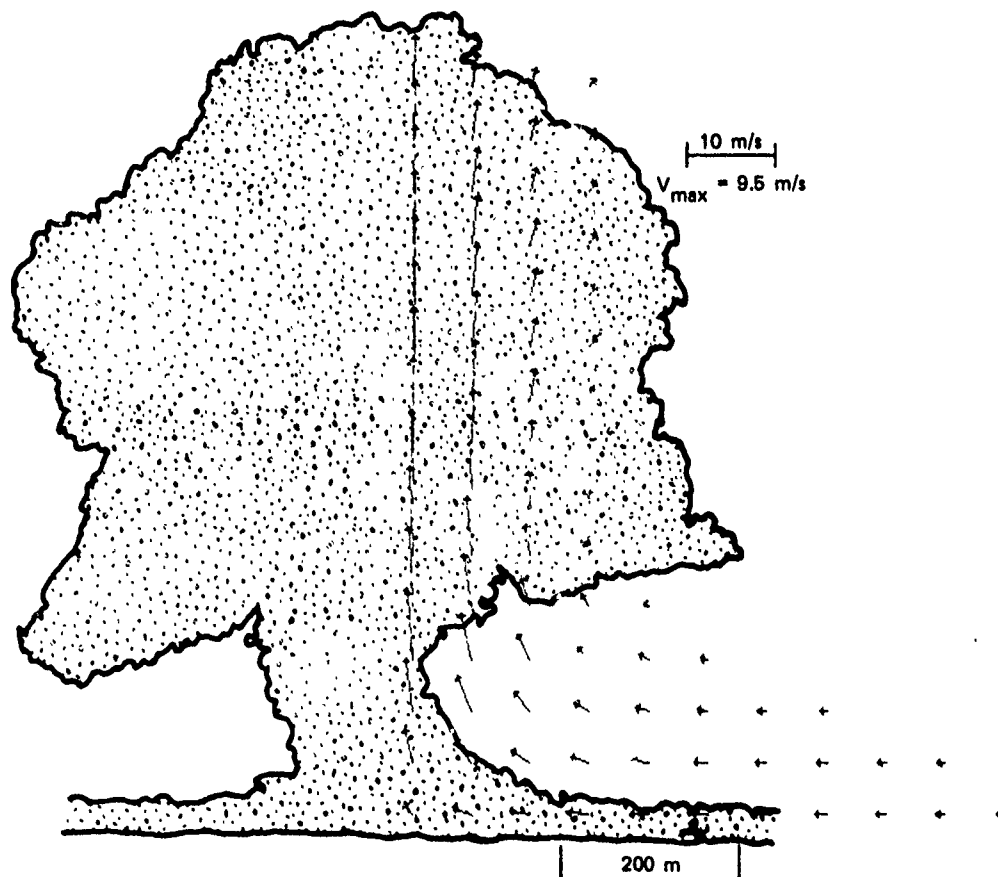
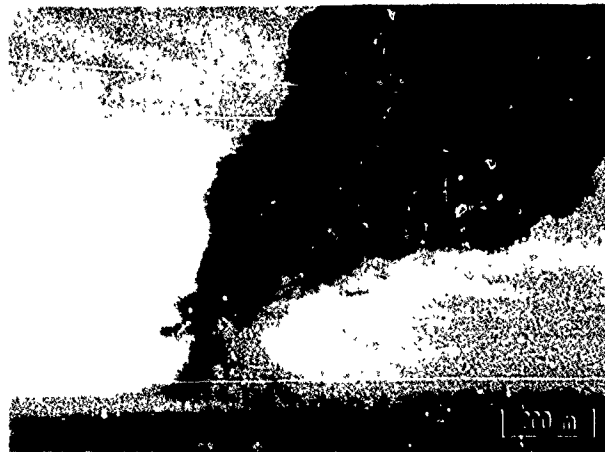


FIGURE B-28 DICE THROW CLOUD COMPARED TO HULL VELOCITY FIELD
CALCULATION AT $T + 1 \text{ min}$



(a) R-1



(b) PR

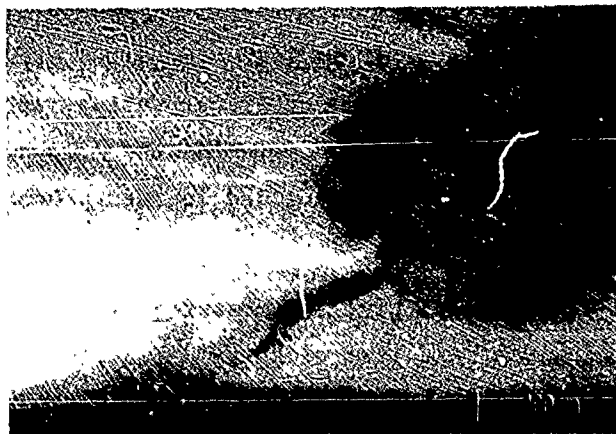


(c) NOP

FIGURE B-29 DICE THROW AT $T + 2$ min



(a) H-1



(b) PR



(c) NOP

FIGURE B-30 DICE THROW AT $T + 4$ min

lower portions of the cloud continued to be blown to the northwest, and a large part of the Jornada de Muerto basin took on a hazy appearance.

7. DICE THROW Dimensional Measurements

Scaled measurements of DICE THROW morphology were undertaken to support interpretation of the rf data. These measurements were made by measuring directly from the film records (or magnified prints thereof) and then factoring in the appropriate variables such as distance between the camera and cloud at T_0 and focal length of the lens. In some cases, where distance was questionable, known distances between objects in the field of view close to ground zero were utilized to determine the magnification factor. Accuracy is estimated to be with ± 5 m; this is established through comparison of specific dimensions measured from different film records at the same time after detonation, taking into account variables in the aspect view of cloud movement and morphology. An exposure of an Accutron clock face was included in each picture frame for timing.

Figures B-31 through B-33 give the measured DICE THROW dimensions of cloud height, cloud width, and stem width as a function of time after detonation taken from photographic data, recorded in cameras at the R-1, PR, and NOP sites, respectively. In each case, the cloud height was measured from the ground to the highest visible point on the cloud, width was determined to be the widest extent, and stem width was measured across its vertical center. In addition, the slope of the rate of cloud rise is identified and indicated. Of particular interest are the cloud height measurements. By comparing the different views with each other and with the photographs in the previous section, one can form a general idea of gross cloud movement caused by prevailing winds.

Up to about $T + 15$ s the cloud height, viewed from the three sites, was fairly even. Thereafter the height measured from the R-1 photographic record (Figure B-31) attained higher levels up to about $T + 1$ min. Data measured from the PR (Figure B-32) and NOP (Figure B-33) sites were fairly even at $T + 20$ s; thereafter, the cloud height from the NOP data

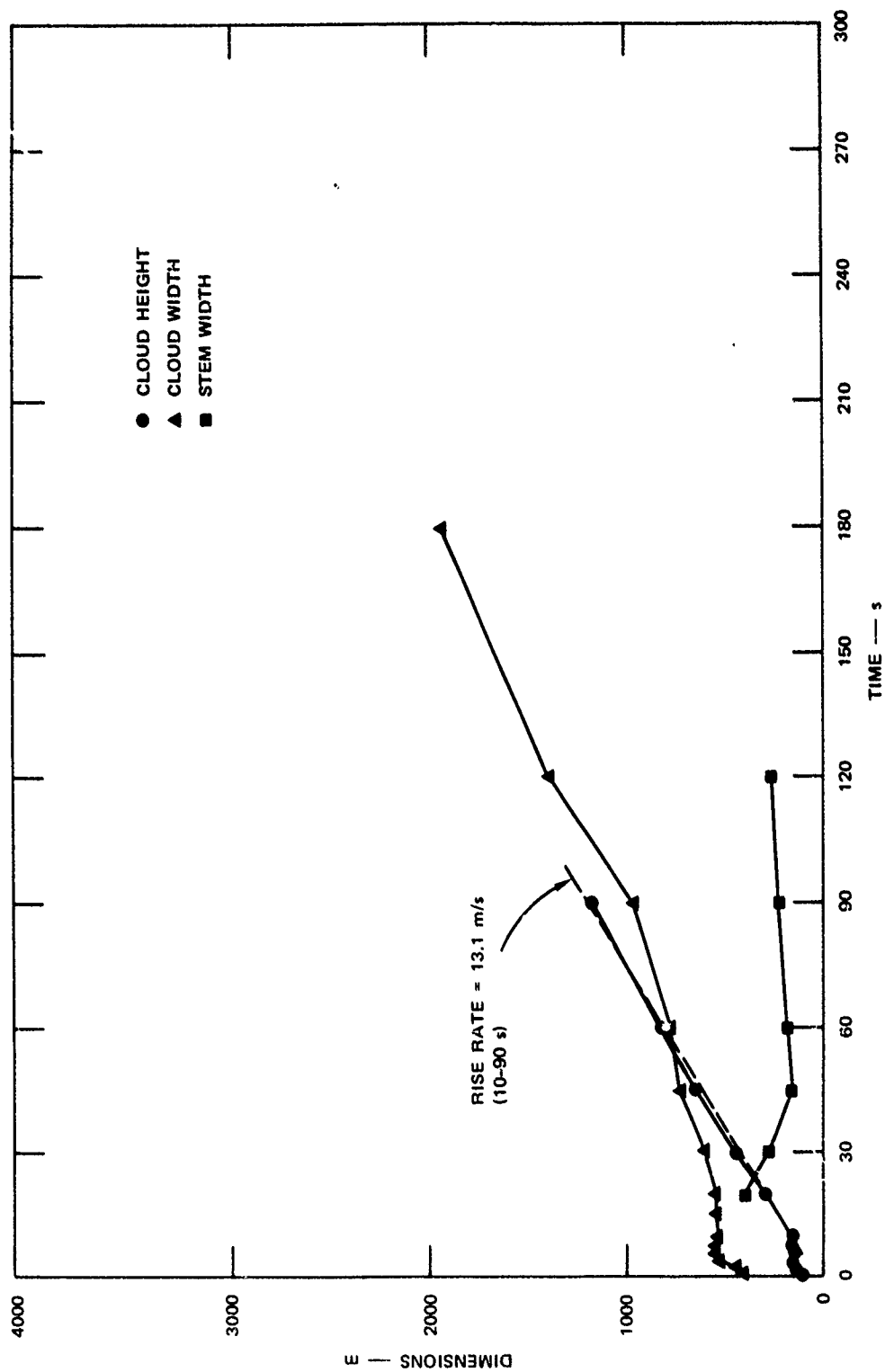


FIGURE B-31 MEASURED CLOUD HEIGHT, WIDTH, AND STEM WIDTH vs TIME FROM RECEIVER 1 CAMERA SITE

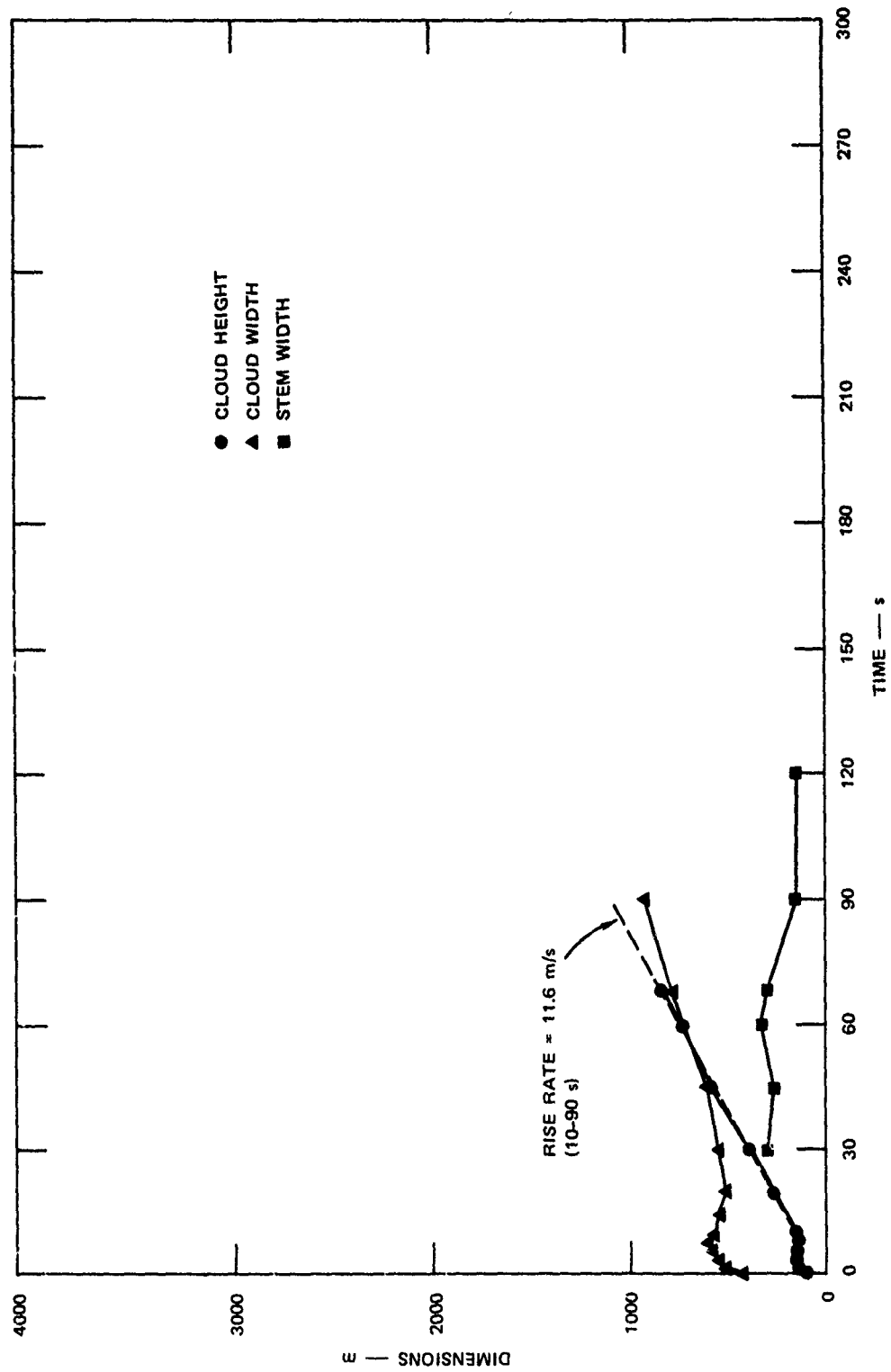


FIGURE B-32 MEASURED CLOUD HEIGHT, WIDTH, AND STEM WIDTH vs TIME FROM PHASE-REPEATER CAMERA SITE

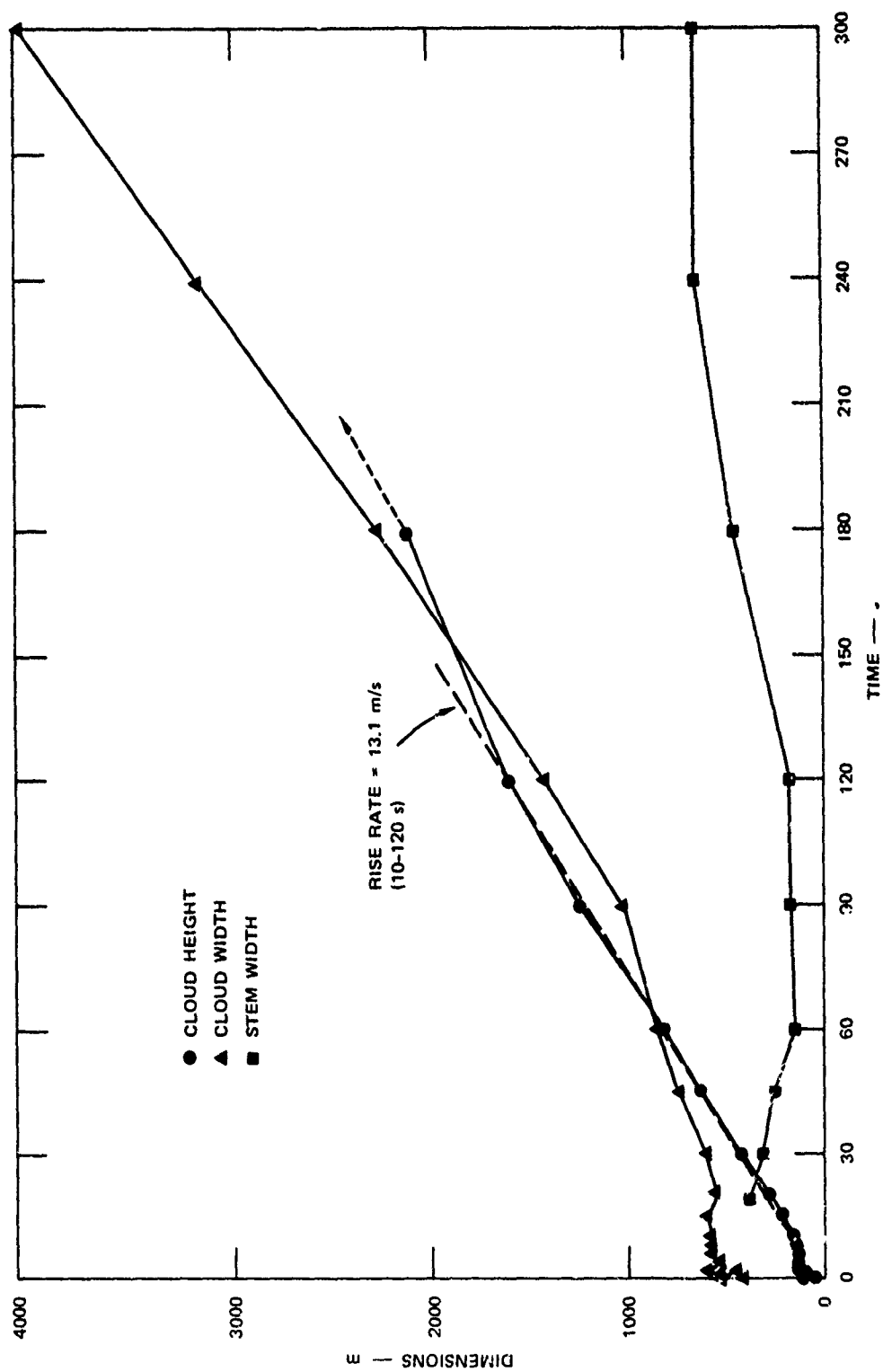


FIGURE B-33 MEASURED CLOUD HEIGHT, WIDTH, AND STEM WIDTH vs TIME FROM NORTH OSCURO PEAK CAMERA SITE

increased more than that from the PR data and rose above that from the R-1 data at T + 90 s. Rise rates for both R-1 and NOP site data were fairly even in the 10-to-90-s regime (13.1 to 13.2 m/s) and higher than the data exhibited by the PR records (11.6 m/s). The discrepancies were most likely due to low-altitude prevailing winds carrying the cloud away from the PR site and somewhat closer to the R-1 site to the northwest. Of course, as the cloud rose, the top edge moved relatively closer to the top of North Oscuro Peak, thus explaining the greater height recorded from the NOP site at T + 90 s than from the R-1 site.

The measured cloud expansion, as seen from the PR and NOP sites, was somewhat faster than from the R-1 site. Later, after T + 30 s, data from NOP showed the greatest expansion, while that from the PR site revealed the slowest. The prevailing winds that moved the DICE THROW cloud away from the PR site can explain part of this discrepancy. However, a more important effect is that of the change in the appearance of the cloud, when viewed from different directions. Figure B-34 gives height and width dimensions for DICE THROW averaged from the R-1, PR, and NOP sites; the average rise rate between T + 10 and T + 120 s was 13 m/s. Figure B-35 presents the corresponding PDT II-2 quantities.* Between T + 10 and T + 60 s, the PDT II-2 cloud had a rise rate of only 7.6 m/s compared to 13 m/s for DICE THROW during the same time period, and by T + 60 s the PDT II-2 cloud had attained a height of only 600 m compared to about 800 m for DICE THROW. The ratios of rise rate and altitude attained (1.7 and 1.3, respectively) are consistent with a cube-root-of-yield scaling rule $[(628/120)^{1/3} = 1.7]$.

The effect that prevailing winds had on displacing the DICE THROW cloud away from ground zero as seen from the R-1 site is graphically presented in Figure B-36. Up to about 1200 m of height (90 s after detonation), the cloud drifted relatively uniformly to the northwest. At higher altitudes, however, winds moving more to the south or southeast

* Measurements were made from photos provided by A. D. Thornbrough, Sandia Labs.

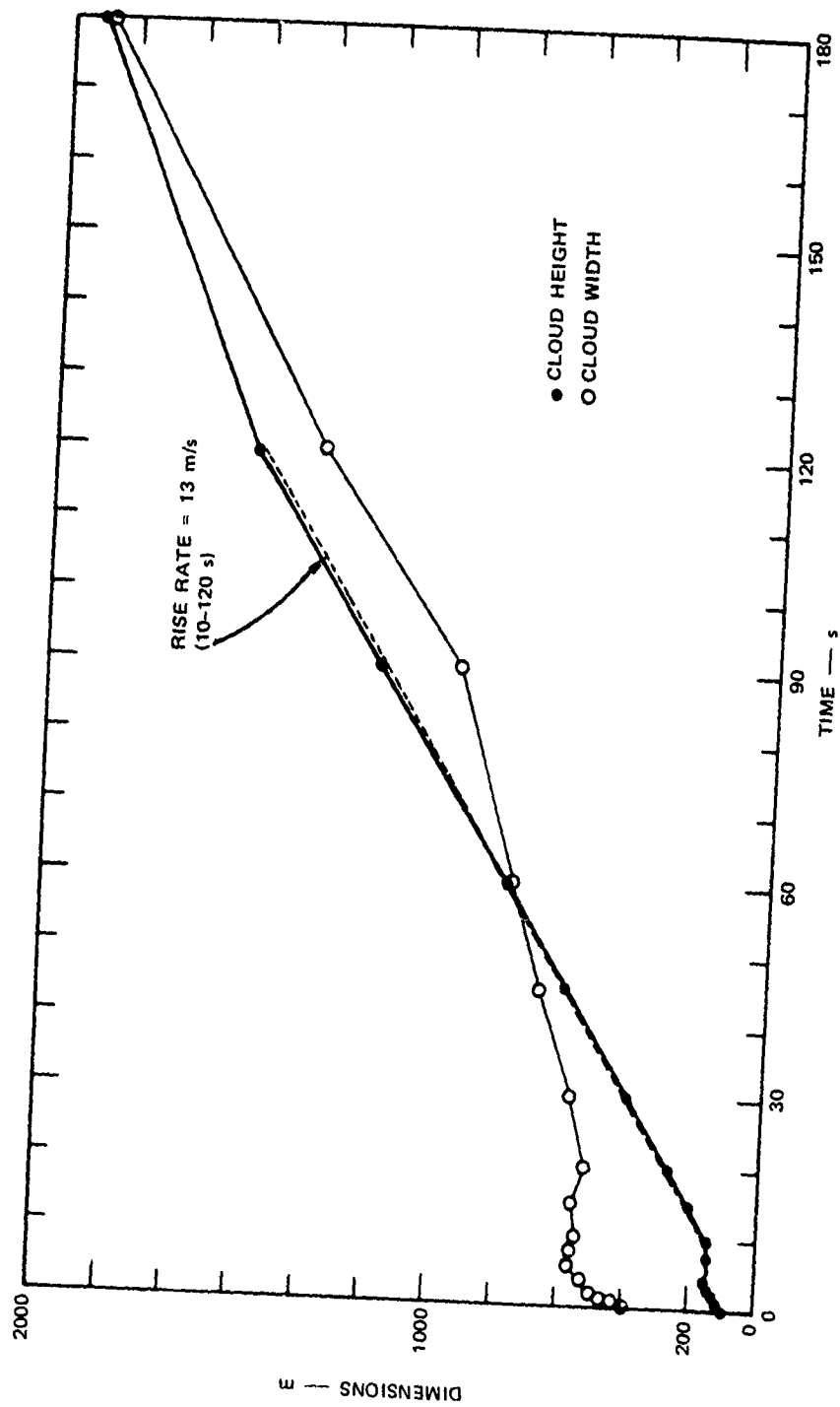


FIGURE B-34 DICE THROW CLOUD HEIGHT AND WIDTH AVERAGED FROM R-1, PR, AND NOP CAMERA SITES

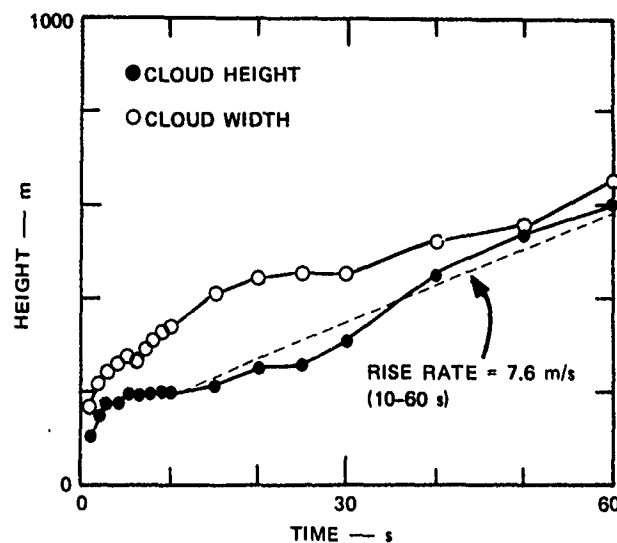


FIGURE B-35 MEASURED PDT II-2 CLOUD HEIGHT AND WIDTH vs TIME

pushed the north side of the cloud top along with them. The center and opposite side of the cloud were more gradually affected by this change in wind vector because of the previous displacement in the opposite direction and the expansion of the cloud. Thus, as noted in the photographs, the lower portions and stem of the DICE THROW cloud maintained a northwesterly movement while the upper, main part of the cloud was blown to the southeast, gradually rising and dispersing up over the South Oscuro ridge.

Figure B-37 displays the DICE THROW cloud volume as a function of time as measured from the film records of the three major camera stations, R-1, PR, and NOP. The volume data from the PR site were corrected slightly (increased) to allow for the increase in distance with time between the camera and the cloud. These data can be used to estimate the average dust density in the cloud as a function of time. Figure B-38 shows the resulting estimated average dust density between $T + 1$ and $T + 100$ s for a constant mass aloft of 3.4 kt, the value obtained from crater measurements described above. Also shown is the average dust density for $T + 1$ to $T + 6$ s for 10 kt aloft. During the initial phase when most of the

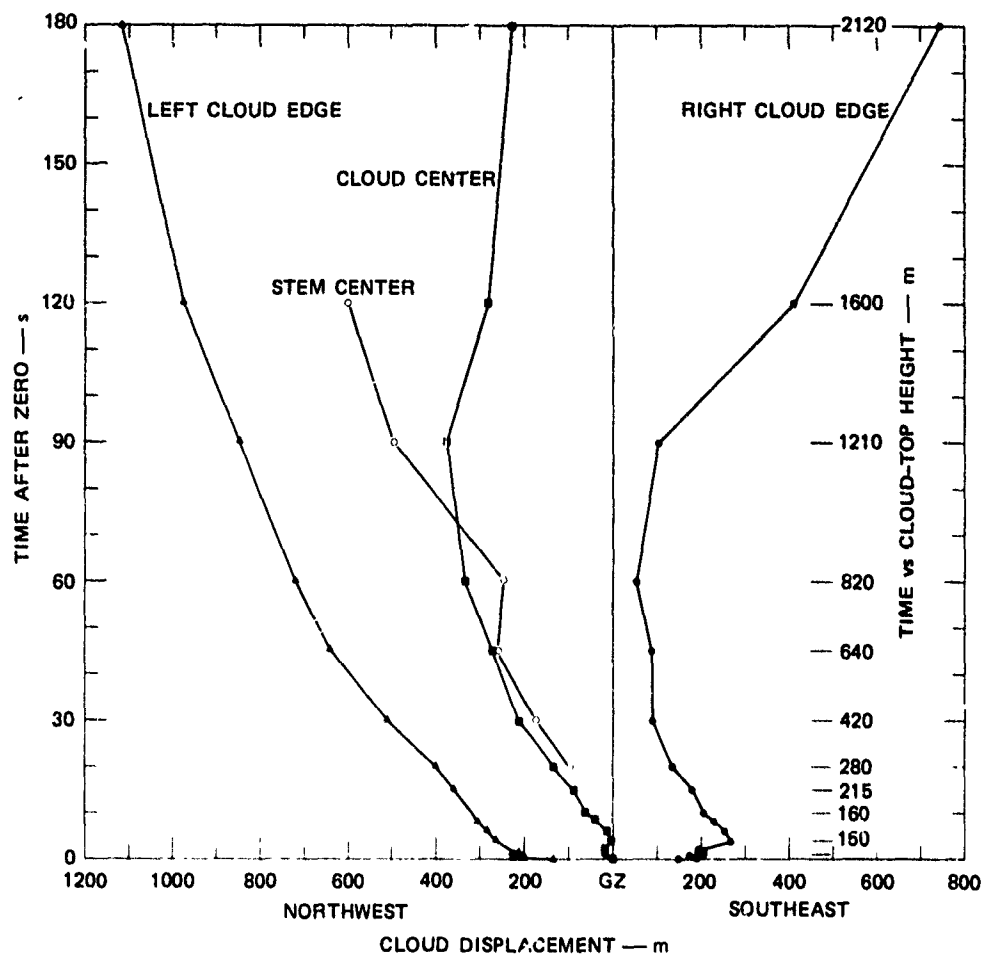


FIGURE B-36 DICE THROW CLOUD EDGE DISPLACEMENT FROM GZ (R-1 Site)

rapid fallout probably occurred, the average dust density in the DICE THROW cloud was in the range 10^{-4} to 10^{-3} g/cm³. According to this model, the average density had dropped to about 10^{-5} g/cm³ by T + 100 s.

8. HULL-Computation and DICE THROW Dust Cloud Predictions

Figures B-39 and B-40, which are reproduced from Ganong et al.,¹¹ summarize some post-event HULL-code calculations. Figure B-39 presents the mass aloft as a function of time for two particle size distributions. Figure B-40 shows the corresponding values of γ , which was defined in Eq. (A-7). Note that this DICE THROW distribution is not the same as the

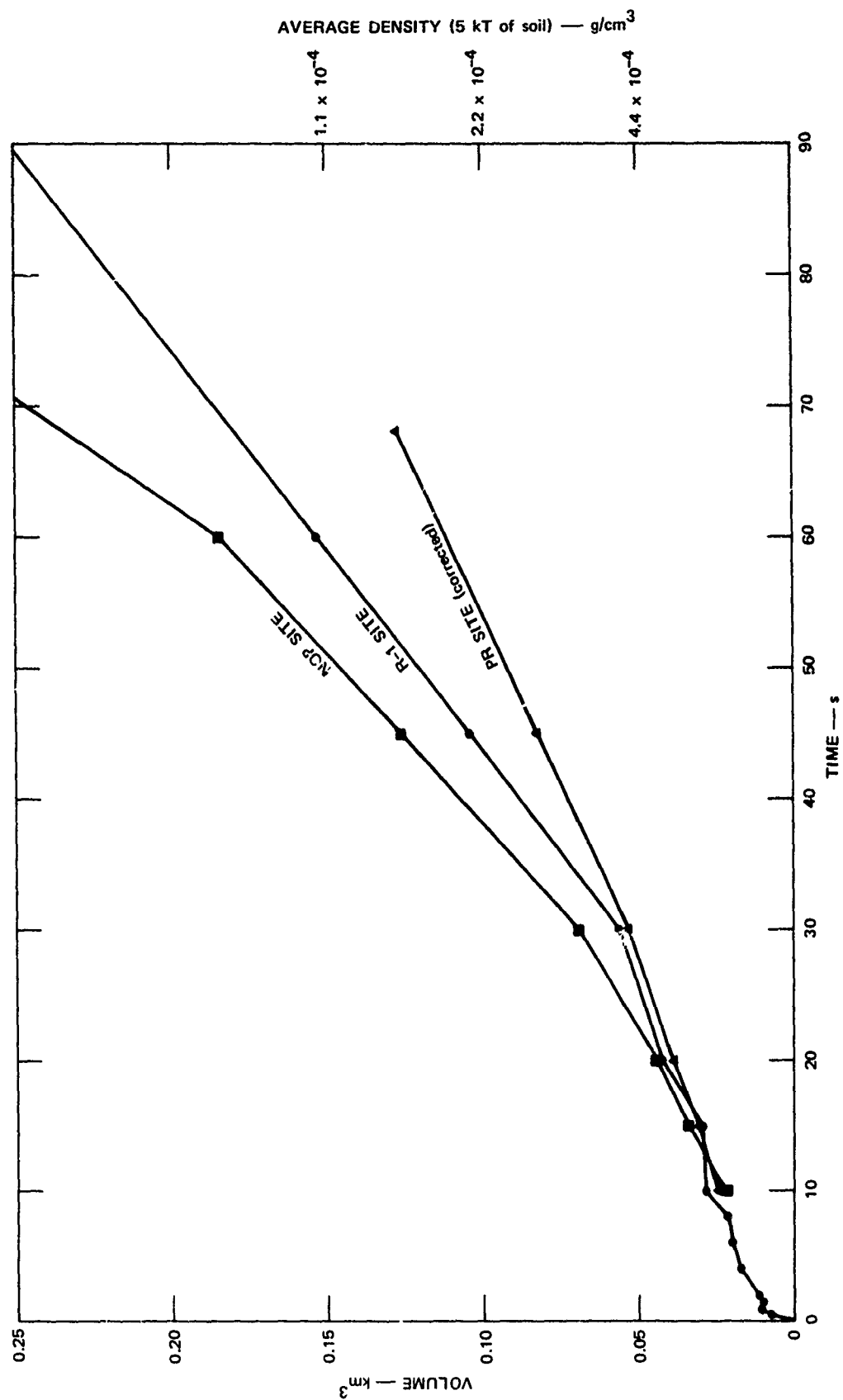


FIGURE B-37 MEASURED DICE THROW CLOUD VOLUME vs TIME

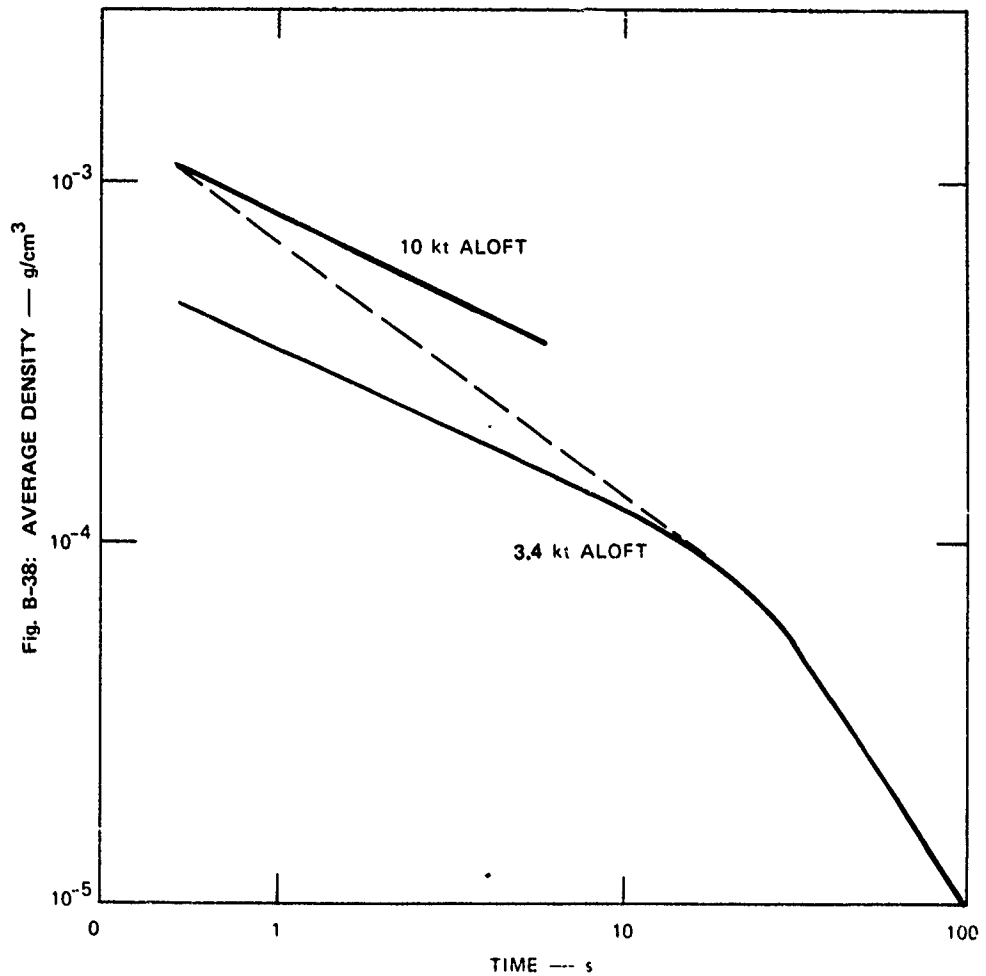


FIGURE B-38 AVERAGE DUST DENSITY IN THE DICE THROW CLOUD INFERRED FROM VOLUME MEASUREMENTS

one approximated by Eq. (A-14), which has features of both the DICE THROW and hard rock distributions. These results were obtained by assuming that 10 kt of ejecta were initially deposited in the volume occupied by the actual DICE THROW cloud at $T + 1$ s. The mass-aloft calculation agrees fairly well with the cratering volume and "missing" mass results of Section 4 of this appendix.

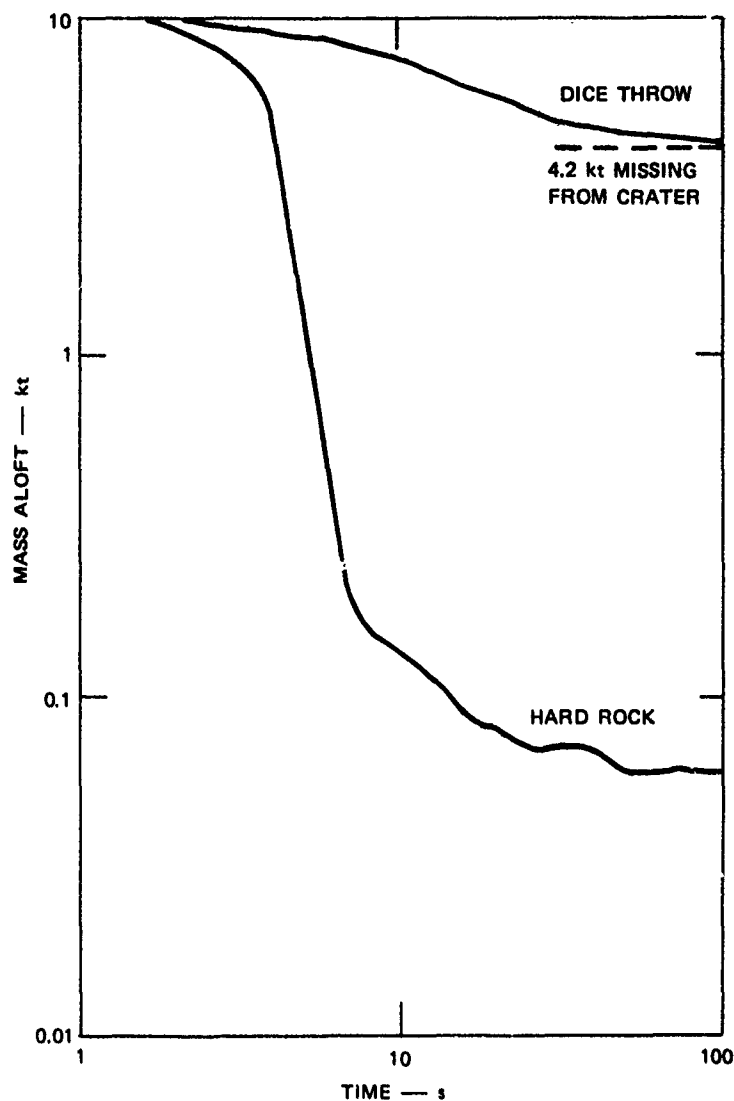


FIGURE B-39 MASS OF DUST ALOFT vs TIME FOR DICE THROW AND HARD ROCK PARTICLE SIZE DISTRIBUTIONS

9. Comparison Between Predicted and Actual Propagation-Path Cloud Penetration Points

One of the important sources of information for the criteria used to determine the physical layout of this experiment was the PDT II-2 cloud development. The PDT II-2 event was a 120-ton ANFO detonation that had exactly the same spherically capped cylinder configuration as the DICE THROW Main Event (PDT II-2 was the culmination of the DICE THROW

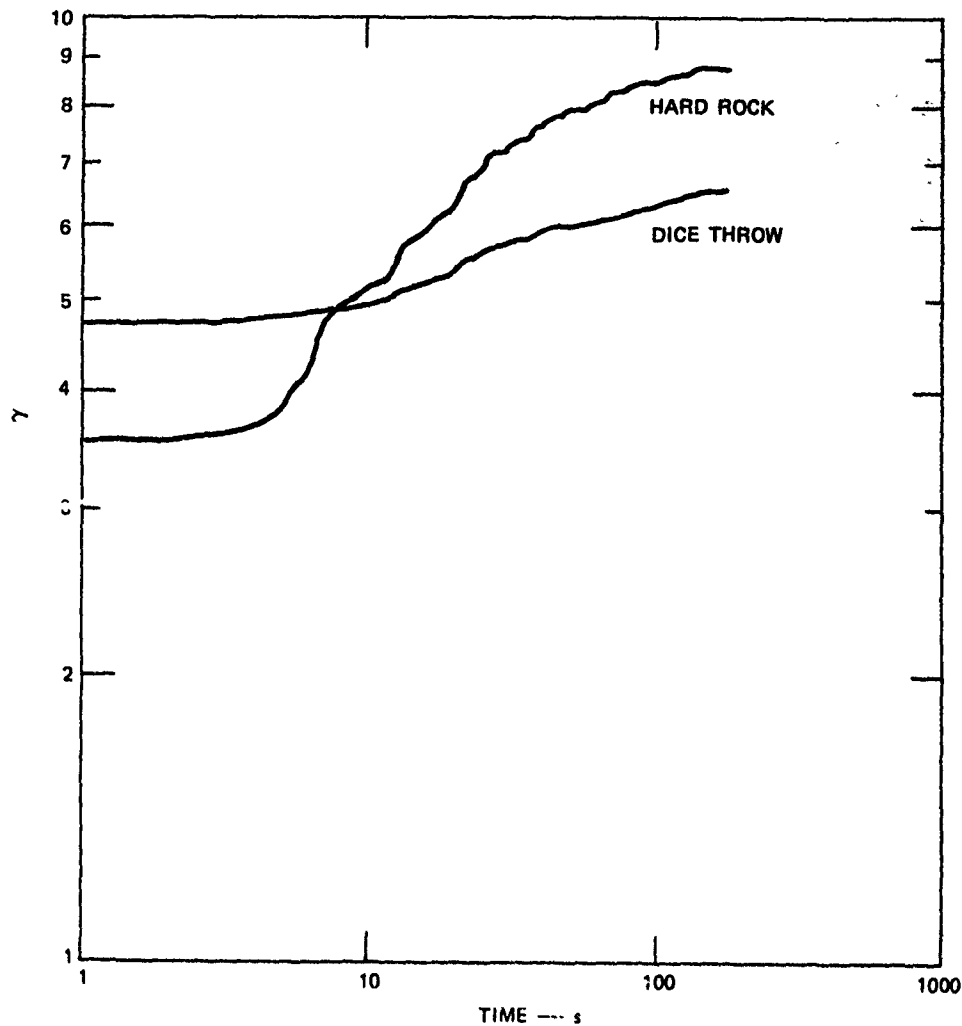


FIGURE B-40 ANFO DUST CLOUD CASE BY PARTICLE SIZE DISTRIBUTION POWER (γ) vs TIME FOR DICE THROW AND HARD ROCK PARTICLE SIZE DISTRIBUTIONS

configuration development). Because the PDT II-2 dust cloud evolved in a much different way than that of the PDT II-1 event, which used a 100-ton TNT tangent sphere configuration, PDT II-2 was believed to be the best guide for DICE THROW planning.

Figure B-41 shows the six DICE THROW propagation-path penetration points at several times superimposed on photographs of the PDT II-2 dust cloud. Both the times and dimensions have been scaled according to a cube-root-of-yield rule (i.e., by $\sqrt[3]{5}$). If this procedure were accurate, a series of long-duration occultations would have been obtained. However, as seen in Figure B-42, where the actual DICE THROW penetration points



(a) $T + 1.71 \text{ s}$



(b) $T + 3.42 \text{ s}$



(c) $T + 6.84 \text{ s}$



(d) $T + 18.68 \text{ s}$



(e) $T + 25.65 \text{ s}$

FIGURE B-41 YIELD-SCALED PHOTOGRAPHS OF PDT II-2 SHOWING ANTICIPATED INTERSECTION OF PROPAGATION PATHS WITH DICE THROW PHENOMENA. Dimensions and time scaled as $3\sqrt{5}$. (Photos courtesy of A. D. Thornbrough, Sandia Labs.)



(a) $T + 2 \text{ s}$



(b) $T + 4 \text{ s}$



(c) $T + 6 \text{ s}$



(d) $T + 15 \text{ s}$



(e) $T + 20 \text{ s}$



(f) $T + 30 \text{ s}$

FIGURE B-42 PHOTOGRAPHS OF DICE THROW SHOWING ACTUAL INTERSECTION OF PROPAGATION PATHS

are shown at about the same times as the scaled ones of Figure B-41, the predictions were quite wrong. Two major reasons for the disagreement were the high winds during DICE THROW and the different soil conditions between the two sites (the PDT series took place at the Queen 15 site about 50 km south of the Giant Patriot location).

Unlike the DICE THROW soil, the PDT soil was very wet. Large craters were formed there, and numerous large (tens of centimeters across) clay "missiles" were ejected and fell over a large area. The rapidly developing ejecta spires that can be seen in the first three frames of Figure B-41 were apparently composed of those large particles. Concern that the "bombs" might damage the equipment for various experiments arranged around the DICE THROW detonation led to the effort to suppress them by excavating the area around ground zero, and backfilling it with sand. It should not be surprising, therefore, that the spires were not seen during DICE THROW. The PDT II-2 and DICE THROW clouds appear to have developed in about the same way, otherwise, if the deformation caused by wind shear is taken into account. However, the presence of many very large particles at early times during PDT II-2 would have undoubtedly led to disproportionately strong rf effects.

10. Summary

From photographic studies, the overall cloud morphologies of DICE THROW and PDT II-2 do not resemble each other enough to unequivocally state that geometric predictions for the DICE THROW behavior were valid. The anticipated early development of an intense cloud of ejecta (spires) to 5 s or 10 s did not characterize DICE THROW. Perhaps because of its larger yield and stronger flow field, the DICE THROW main event produced a less amorphous cloud than did PDT II-2. The general development of the DICE THROW cloud and the mass aloft seems to be consistent with the HULL predictions. It appears that no dust was injected by the detonation into the region where the normal-direction vortex formation is predicted. If the calculations are accurate, no dust entrainment in the vortex region ever took place, and the visible cloud remained in a region of mostly vertical flow and thus corresponded to a "stem." Because part of the

reason for performing measurements during these tests is to verify or improve the codes, the possibility of marking the region of (currently visible) vortex formation with smoke trails or the like should be considered.

REFERENCES

1. DNA, Proceedings of the DICE THROW Symposium 21-23 June 1977, Vols. 1-3, DNA 4377P-1, -2, -3, Contract DNA001-75-C-0023, General Electric Company-TEMPO, DASIAC, Santa Barbara, CA, 93102 (July 1977).
2. A. A. Burns, "DICE THROW UHF/SHF Transmission Experiment--Preliminary Results, Stanford Research Institute, Menlo Park, CA, 94025 (January 1977), unpublished.
3. A. A. Burns and R. E. Winkelman, "DICE THROW UHF/SHF Transmission Experiment--Dielectric Properties of Dust," Stanford Research Institute, Menlo Park, CA, 94025 (March 1977), unpublished.
4. A. A. Burns and G. Smith, "Design of an Experiment to Measure RF Propagation Through Dust and Debris," Stanford Research Institute, Menlo Park, CA, 94025 (August 1975), unpublished.
5. R. L. Bollen, W. G. Chesnut, V. E. Hatfield, and G. Smith, "Predictions of Effects Upon Experimental Microwave Links Following the DICE THROW Detonation," DNA 4183T, Final Report, SRI Project 4887, Contract DNA001-76-C-0207, Stanford Research Institute, Menlo Park, CA, 94025 (September 1976).
6. W. G. Chesnut, "Relative Intensity of Incoherent and Semicoherent Scattering from Turbulent Particulate Clouds," DNA 4666T, Technical Report 1, SRI Project 6900, Contract DNA001-78-C-0075, SRI International, Menlo Park, CA, 94025 (July 1978).
7. M. J. Campbell, J. Ulrichs, and B. W. Hapke, "The Electrical Properties of Rocks and Their Significance for Lunar Radar Observations," CRSR 333, Center for Radiophysics and Space Research, Cornell University, Ithaca, NY (February 1969).
8. M. Born and E. Wolf, Principles of Optics, 3rd Ed. (Pergamon Press, London, 1965).
9. J. D. Jackson, Classical Electrodynamics (John Wiley & Sons, Inc., New York, 1962).
10. E. J. Kownacki and R. P. Welty, "DIAL PACK Radar Analysis," DNA 2909F, Final Report, SAI-72-512-AR, Contract DNA001-72-0031, Science Applications, Inc., 1701 North Fort Myer Drive, Suite 908, Arlington, Virginia, 22209 (June 1972).

11. G. P. Ganong, S. E. Check, and C. E. Needham, "DICE THROW Dust Cloud Calculations," in Proceedings of the DICE THROW Symposium 21-23 June 1977, Volume II, DNA 4377P-2, Contract DNA001-75-C-0023, General Electric Co.-TEMPO, DASIAC, 816 State St., Santa Barbara, CA, 93102 (July 1977).

DISTRIBUTION LIST

DEPARTMENT OF DEFENSE

Assistant Secretary of Defense
Comm., Cmd., Cont. & Intell.
ATTN: C3IST&CCS, M. Epstein
ATTN: Dir. of Intelligence Systems,
J. Babcock

Assistant to the Secretary of Defense
Atomic Energy
ATTN: Executive Assistant

Command & Control Technical Center
ATTN: C-312, R. Mason
ATTN: C-650, G. Jones
3 cy ATTN: C-650, W. Heidig

Defense Advanced Rsch. Proj. Agency
ATTN: TIO

Defense Communications Agency
ATTN: Code 205
ATTN: Code R1033, M. Raffensperger
ATTN: Code 480, F. Dieter
ATTN: Code 101B
ATTN: Code 810, J. Barna
ATTN: Code 380

Defense Communications Engineer Center
ATTN: Code R720, J. Worthington
ATTN: Code R410, J. McLean
ATTN: Code R123
ATTN: Code R410, R. Craighill

Defense Intelligence Agency
ATTN: DC-7D, W. Wittig
ATTN: HQ-TR, J. Stewart
ATTN: DB-4C, E. O'Farrell
ATTN: DT-5
ATTN: DB, A. Wise
ATTN: DI-1B

Defense Nuclear Agency
ATTN: STVL
3 cy ATTN: RAAE
4 cy ATTN: TITL

Defense Technical Information Center
12 cy ATTN: DD

Field Command
Defense Nuclear Agency
ATTN: FCPR

Field Command
Defense Nuclear Agency
Livermore Division
ATTN: FCPRL

Interservice Nuclear Weapons School
ATTN: ITV

Joint Chiefs of Staff
ATTN: C35
ATTN: C35, Evaluation Office

DEPARTMENT OF DEFENSE (Continued)

Joint Strat. Tgt. Planning Staff
ATTN: JLTW-2

National Security Agency
ATTN: R-52, J. Skillman
ATTN: B-3, F. Leonard
ATTN: W-32, O. Bartlett

Undersecretary of Defense for Rsch. & Engrg.
ATTN: Strategic & Space Systems (OS)

WMCCS System Engineering Org.
ATTN: R. Crawford
ATTN: J. Hoff

DEPARTMENT OF THE ARMY

Assistant Chief of Staff for Automation & Comm.
Department of the Army
ATTN: DAAC-ZT, P. Kenny

Atmospheric Sciences Laboratory
U.S. Army Electronics R&D Command
ATTN: DELAS-EO, F. Niles

BMD Systems Command
Department of the Army
2 cy ATTN: BMDSC-HW

Deputy Chief of Staff for Ops. & Plans
Department of the Army
ATTN: DAMO-RQC

Electronics Tech. & Devices Lab.
U.S. Army Electronics R&D Command
ATTN: DELET-ER, H. Bomke

Harry Diamond Laboratories
Department of the Army
ATTN: DELHD-N-P
ATTN: DELHD-N-RB, R. Williams
ATTN: DELHD-N-P, F. Wizenitz
ATTN: DELHD-I-TL, M. Weiner

U. S. Army Comm.-Elec. Engrg. Instal. Agency
ATTN: CCC-EMEO, W. Nair
ATTN: CCC-EMEO-PED, G. Lane
ATTN: CCC-CED-CCO, W. Neuendorf

U.S. Army Communications Command
ATTN: CC-OPS-W
ATTN: CC-OPS-WR, H. Wilson

U.S. Army Communications R&D Command
ATTN: DRDCO-COM-RY, W. Kesselman

U.S. Army Foreign Science & Tech. Center
ATTN: DRXST-SD

U.S. Army Materiel Dev. & Readiness Command
ATTN: DRCLDC, J. Bender

DEPARTMENT OF THE ARMY (Continued)

U.S. Army Nuclear & Chemical Agency
ATTN: Library

U.S. Army Satellite Comm. Agency
ATTN: Document Control

U.S. Army TRADOC Systems Analysis Activity
ATTN: ATAA-PL
ATTN: ATAA-TCC, F. Payan, Jr.
ATTN: ATAA-TDC

DEPARTMENT OF THE NAVY

Joint Cruise Missile Project Office
Department of the Navy
ATTN: JCM-G-70

Naval Air Development Center
ATTN: Code 6091, M. Setz

Naval Air Systems Command
ATTN: PMA 271

Naval Electronic Systems Command
ATTN: Code 3101, T. Hughes
ATTN: PME 117-20
ATTN: Code 501A
ATTN: PME 117-2013, G. Burnhart
ATTN: PME 117-211, B. Kruger
ATTN: PME 106-4, S. Kearney
ATTN: PME 106-13, T. Griffin

Naval Intelligence Support Center
ATTN: NISC-50

Naval Ocean Systems Center
ATTN: Code 5322, M. Paulson
ATTN: Code 532, J. Bickel
3 cy ATTN: Code 5324, W. Moler

Naval Research Laboratory
ATTN: Code 6780, S. Ossakow
ATTN: Code 6700, T. Coffey
ATTN: Code 7550, J. Davis
ATTN: Code 7500, B. Wald

Naval Space Surveillance System
ATTN: J. Burton

Naval Surface Weapons Center
ATTN: Code F31

Naval Surface Weapons Center
ATTN: Code F-14, R. Butler

Naval Telecommunications Command
ATTN: Code 341

Office of Naval Research
ATTN: Code 420
ATTN: Code 421

Office of the Chief of Naval Operations
ATTN: OP 604C
ATTN: OP 941D
ATTN: OP 981N

DEPARTMENT OF THE NAVY (Continued)

Strategic Systems Project Office
Department of the Navy
ATTN: NSP-2722, F. Wimberly
ATTN: NSP-2141
ATTN: NSP-43

DEPARTMENT OF THE AIR FORCE

Aerospace Defense Command
Department of the Air Force
ATTN: DC, T. Long

Air Force Avionics Laboratory
ATTN: AAD, W. Hunt
ATTN: AAD, A. Johnson

Air Force Geophysics Laboratory
ATTN: LKB, K. Champion
ATTN: OPR-1, J. Ulwick
ATTN: PHP, J. Aarons
ATTN: PHI, J. Buchau
ATTN: PHP, J. Mullen
ATTN: OPR, A. Stair

Air Force Weapons Laboratory
Air Force Systems Command
ATTN: DYC
ATTN: SUL

Air Logistics Command
Department of the Air Force
ATTN: OO-ALC/MM, R. Blackburn

Assistant Chief of Staff
Intelligence
Department of the Air Force
ATTN: INED

Assistant Chief of Staff
Studies & Analyses
Department of the Air Force
ATTN: AF/SASC, W. Adams
ATTN: AF/SASC, G. Zank

Ballistic Missile Office
Air Force Systems Command
ATTN: MNNL, S. Kennedy
ATTN: MNNH, M. Baran
ATTN: MNNH

Deputy Chief of Staff
Operations, Plans & Readiness
Department of the Air Force
ATTN: AFXOXFD
ATTN: AFXOKCD
ATTN: AFXOKT
ATTN: AFXOKS

Deputy Chief of Staff
Research, Development, & Acq.
Department of the Air Force
ATTN: AFRDQ
ATTN: AFRDSP
ATTN: AFRDSS
ATTN: AFRDS

DEPARTMENT OF THE AIR FORCE (Continued)

Electronic Systems Division
Department of the Air Force
ATTN: DCKC, J. Clark

Electronic Systems Division
Department of the Air Force
ATTN: XRW, J. Deas

Electronic Systems Division
Department of the Air Force
ATTN: YSM, J. Kobelski
ATTN: YSEA

Foreign Technology Division
Air Force Systems Command
ATTN: TQTD, B. Ballard
ATTN: NIIS, Library
ATTN: SDEC, A. Oakes

Headquarters Space Division
Air Force Systems Command
ATTN: SKA, M. Clavin
ATTN: SKA, C. Rightmyer

Headquarters Space Division
Air Force Systems Command
ATTN: SZJ, W. Mercer
ATTN: SZJ, L. Doan

Rome Air Development Center
Air Force Systems Command
ATTN: OCS, V. Coyne
ATTN: TSLD

Rome Air Development Center
Air Force Systems Command
ATTN: EEP

Strategic Air Command
Department of the Air Force
ATTN: XPFS
ATTN: NRT
ATTN: DCX
ATTN: DCXF
ATTN: DCXT, T. Jorgensen
ATTN: DCXT
ATTN: OOKSN

DEPARTMENT OF ENERGY CONTRACTORS

EG&G, Inc.
Los Alamos Division
ATTN: J. Colvin
ATTN: D. Wright

Lawrence Livermore Laboratory
ATTN: Technical Information Dept. Library

Los Alamos Scientific Laboratory
ATTN: D. Westervelt
ATTN: P. Keaton
ATTN: R. Taschek

Sandia Laboratories
Livermore Laboratory
ATTN: T. Cook
ATTN: B. Murphey

DEPARTMENT OF ENERGY CONTRACTORS (Continued)

Sandia Laboratories
ATTN: D. Thornbrough
ATTN: D. Dahlgren
ATTN: Org. 1250, W. Brown
ATTN: Space Project Division
ATTN: 3141

OTHER GOVERNMENT AGENCIES

Central Intelligence Agency
ATTN: OSI/PSTD

Department of Commerce
National Bureau of Standards
ATTN: R. Moore

Department of Commerce
National Oceanic & Atmospheric Admin.
ATTN: R. Grubb

Institute for Telecommunications Sciences
National Telecommunications & Info. Admin.
ATTN: L. Berry
ATTN: A. Jean
ATTN: W. Utlaut
ATTN: D. Crombie

U.S. Coast Guard
Department of Transportation
ATTN: G-DOE-3/TP54, B. Romine

DEPARTMENT OF DEFENSE CONTRACTORS

Aerospace Corp.
ATTN: F. Morse
ATTN: N. Stockwell
ATTN: I. Garfunkel
ATTN: D. Olsen
ATTN: S. Bower
ATTN: T. Salmi
ATTN: R. Slaughter
ATTN: V. Josephson

University of Alaska
ATTN: Technical Library
ATTN: T. Davis
ATTN: N. Brown

Analytical Systems Engineering Corp.
ATTN: Radio Sciences

Analytical Systems Engineering Corp.
ATTN: Security

Barry Research Communications
ATTN: J. McLaughlin

BDM Corp.
ATTN: L. Jacobs
ATTN: T. Neighbors

Berkeley Research Associates, Inc.
ATTN: J. Workman

Boeing Co.
ATTN: M/S 42-33, J. Kennedy
ATTN: S. Tashird
ATTN: G. Hall

DEPARTMENT OF DEFENSE CONTRACTORS (Continued)

University of California at San Diego
ATTN: H. Booker

Charles Stark Draper Lab., Inc.
ATTN: D. Cox
ATTN: J. Gilmore

Computer Sciences Corp.
ATTN: H. Blank

Comsat Labs.
ATTN: G. Hyde
ATTN: R. Taur

Cornell University
ATTN: D. Farley, Jr.

Electrospace Systems, Inc.
ATTN: H. Logston

ESL, Inc.
ATTN: C. Prettie
ATTN: J. Roberts
ATTN: J. Marshall

Ford Aerospace & Communications Corp.
ATTN: J. Mattingley

General Electric Co.
ATTN: M. Bortner

General Electric Co.
ATTN: A. Steinmayer
ATTN: C. Zierdt

General Electric Co.
ATTN: F. Peibert

General Electric Company-TEMPO
ATTN: W. Knapp
ATTN: M. Stanton
ATTN: T. Stevens
ATTN: D. Chandler
ATTN: DA FAC

General Electric Tech. Services Co., Inc.
ATTN: G. Millman

General Research Corp.
ATTN: J. Ise, Jr.
ATTN: J. Garbarino

GTE Sylvania, Inc.
ATTN: M. Cross

HSS, Inc.
ATTN: D. Hansen

IBM Corp.
ATTN: F. Ricci

University of Illinois
ATTN: K. Yeh

DEPARTMENT OF DEFENSE CONTRACTORS (Continued)

Institute for Defense Analyses
ATTN: E. Bauer
ATTN: J. Aein
ATTN: J. Bengston
ATTN: H. Wolfhard

International Tel. & Telegraph Corp.
ATTN: Technical Library
ATTN: G. Wetmore

JAYCOR
ATTN: S. Goldman

JAYCOR
ATTN: D. Carlos

Johns Hopkins University
ATTN: T. Potemra
ATTN: Document Librarian
ATTN: P. Komiske
ATTN: T. Evans
ATTN: J. Newland
ATTN: B. Wise

Kaman Sciences Corp.
ATTN: T. Meagher

Linkabit Corp.
ATTN: I. Jacobs

Litton Systems, Inc.
ATTN: R. Grasty

Lockheed Missiles & Space Co., Inc.
ATTN: Dept. 60-12
ATTN: D. Churchill

Lockheed Missiles and Space Co., Inc.
ATTN: R. Johnson
ATTN: M. Walt
ATTN: W. Imhof

M.I.T. Lincoln Lab.
ATTN: D. Towle
ATTN: L. Loughlin

McDonnell Douglas Corp.
ATTN: N. Harris
ATTN: G. Mroz
ATTN: J. Moule
ATTN: W. Olson

Meteor Communications Consultants
ATTN: R. Leader

Mission Research Corp.
ATTN: R. Hendrick
ATTN: S. Gutsche
ATTN: F. Fajen
ATTN: D. Sowle
ATTN: R. Bogusch

DEPARTMENT OF DEFENSE CONTRACTORS (Continued)

Mitre Corp.
ATTN: C. Callahan
ATTN: G. Harding
ATTN: A. Kymmel
ATTN: B. Adams

Mitre Corp.
ATTN: W. Foster
ATTN: M. Horrocks
ATTN: W. Hall

Pacific-Sierra Research Corp.
ATTN: E. Field, Jr.

Pennsylvania State University
ATTN: Ionospheric Research Lab.

Photometrics, Inc.
ATTN: I. Kofsky

Physical Dynamics, Inc.
ATTN: E. Fremouw

R & D Associates
ATTN: R. Lelevier
ATTN: B. Gabbard
ATTN: R. Turco
ATTN: F. Gilmore
ATTN: H. Ory
ATTN: W. Karzas
ATTN: W. Wright, Jr.
ATTN: C. MacDonald
ATTN: C. Greifinger
ATTN: M. Gantsweg

R & D Associates
ATTN: L. Delaney
ATTN: B. Yoon

Rand Corp.
ATTN: F. Bedrozian
ATTN: C. Crain

Riverside Research Institute
ATTN: V. Trapani

Science Applications, Inc.
ATTN: SZ

DEPARTMENT OF DEFENSE CONTRACTORS (Continued)

Rockwell International Corp.
ATTN: J. Kristof

Santa Fe Corp.
ATTN: E. Ortlieb

Science Applications, Inc.
ATTN: L. Linson
ATTN: D. Hamlin
ATTN: D. Sachs
ATTN: E. Straker
ATTN: J. McDougall
ATTN: C. Smith

Science Applications, Inc.
ATTN: D. Davis

SRI International
ATTN: C. Rino
ATTN: G. Smith
ATTN: G. Price
ATTN: R. Leadabrand
ATTN: W. Jaye
ATTN: W. Chesnut
ATTN: M. Baron
ATTN: A. Burns
ATTN: D. Neilson
ATTN: R. Livingston

Teledyne Brown Engineering
ATTN: R. Deliberis

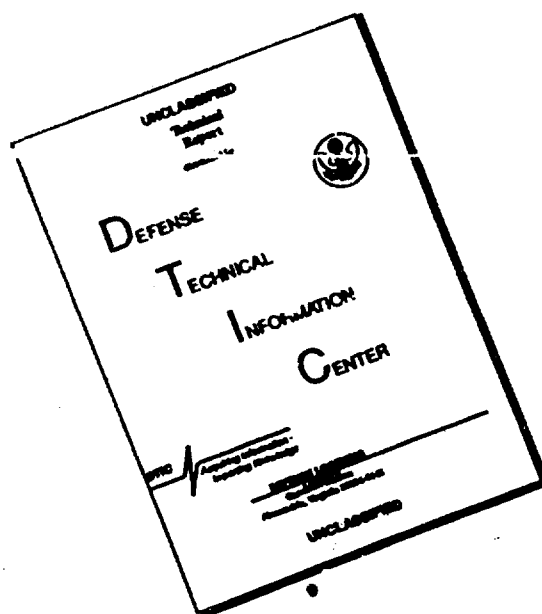
Tri-Com, Inc.
ATTN: D. Murray

TRW Defense & Space Sys. Group
ATTN: S. Altschuler
ATTN: R. Plebuch
ATTN: D. Dee

Utah State University
ATTN: L. Jensen
ATTN: K. Baker

Visidyne, Inc.
ATTN: J. Carpenter

DISCLAIMER NOTICE



THIS DOCUMENT IS BEST
QUALITY AVAILABLE. THE COPY
FURNISHED TO DTIC CONTAINED
A SIGNIFICANT NUMBER OF
PAGES WHICH DO NOT
REPRODUCE LEGIBLY.